NASA/CR—2007-214815

# Unsteady Velocity Measurements in the NASA Research Low Speed Axial Compressor

## Smooth Wall Configuration

*Jan Lepicovsky*
*ASRC Aerospace Corporation, Cleveland, Ohio*

May 2007

# NASA STI Program . . . in Profile

Since its founding, NASA has been dedicated to the advancement of aeronautics and space science. The NASA Scientific and Technical Information (STI) program plays a key part in helping NASA maintain this important role.

The NASA STI Program operates under the auspices of the Agency Chief Information Officer. It collects, organizes, provides for archiving, and disseminates NASA's STI. The NASA STI program provides access to the NASA Aeronautics and Space Database and its public interface, the NASA Technical Reports Server, thus providing one of the largest collections of aeronautical and space science STI in the world. Results are published in both non-NASA channels and by NASA in the NASA STI Report Series, which includes the following report types:

- TECHNICAL PUBLICATION. Reports of completed research or a major significant phase of research that present the results of NASA programs and include extensive data or theoretical analysis. Includes compilations of significant scientific and technical data and information deemed to be of continuing reference value. NASA counterpart of peer-reviewed formal professional papers but has less stringent limitations on manuscript length and extent of graphic presentations.

- TECHNICAL MEMORANDUM. Scientific and technical findings that are preliminary or of specialized interest, e.g., quick release reports, working papers, and bibliographies that contain minimal annotation. Does not contain extensive analysis.

- CONTRACTOR REPORT. Scientific and technical findings by NASA-sponsored contractors and grantees.

- CONFERENCE PUBLICATION. Collected papers from scientific and technical conferences, symposia, seminars, or other meetings sponsored or cosponsored by NASA.

- SPECIAL PUBLICATION. Scientific, technical, or historical information from NASA programs, projects, and missions, often concerned with subjects having substantial public interest.

- TECHNICAL TRANSLATION. English-language translations of foreign scientific and technical material pertinent to NASA's mission.

Specialized services also include creating custom thesauri, building customized databases, organizing and publishing research results.

For more information about the NASA STI program, see the following:

- Access the NASA STI program home page at *http://www.sti.nasa.gov*

- E-mail your question via the Internet to *help@sti.nasa.gov*

- Fax your question to the NASA STI Help Desk at 301–621–0134

- Telephone the NASA STI Help Desk at 301–621–0390

- Write to:
  NASA Center for AeroSpace Information (CASI)
  7115 Standard Drive
  Hanover, MD 21076–1320

NASA/CR—2007-214815

# Unsteady Velocity Measurements in the NASA Research Low Speed Axial Compressor

## Smooth Wall Configuration

*Jan Lepicovsky*
*ASRC Aerospace Corporation, Cleveland, Ohio*

Prepared under Contract NNC06BA07B

National Aeronautics and
Space Administration

Glenn Research Center
Cleveland, Ohio 44135

May 2007

## Acknowledgments

The work was sponsored by the NASA Glenn Research Center under the Intelligent Propulsion Systems Foundation Technologies by Dr. C.R. Mercer. The author would like to thank Mr. J.P. Veres, chief of the GRC Compressor Branch, for his support and permission to publish the results of this study, to Dr. G.E. Welch of Army Research Laboratory for his role in initiation of this work, and mainly to Mr. E.P. Braunscheidel of NASA GRC for his significant effort in managing the test facility operation. Help from Ms. E.L. Parrott and Mr. R. Torres, both of NASA GRC, is also gratefully acknowledged.



This work was sponsored by the Fundamental Aeronautics Program at the NASA Glenn Research Center.

*Level of Review*: This material has been technically reviewed by NASA expert reviewer(s).

Available from

NASA Center for Aerospace Information
7115 Standard Drive
Hanover, MD 21076–1320

National Technical Information Service
5285 Port Royal Road
Springfield, VA 22161

Available electronically at http://gltrs.grc.nasa.gov

# Unsteady Velocity Measurements in the NASA Research Low Speed Axial Compressor
## Smooth Wall Configuration

Jan Lepicovsky
ASRC Aerospace Corporation
Cleveland, Ohio 44135

## Introduction

The report is a collection of experimental unsteady data acquired in the first stage of the NASA Low Speed Axial Compressor in configuration with smooth (solid) wall treatment over the first rotor. It is the basic configuration of this compressor. The aim of the report is to present a reliable experimental data base that can be used for analysis of the compressor flow behavior, and hopefully help with further improvements of compressor CFD codes. There is no attempt in the report to explain or analyze the data acquired from the standpoint of compressor performance. All data analysis is strictly restricted to verification of reliability of the experimental data reported.

The report is divided into six main sections. The low speed axial compressor and the basic instrumentation are briefly described in the first section. It is followed by a section with description of an in-house developed methodology of unsteady velocity measurements using a thermo-anemometric split-fiber probe; a probe frequency response is also discussed in the second section. The third section contains first a set of experimental data presented as averaged radial distributions for three compressor operation conditions. Spanwise distributions of the tangential velocity component, measured upstream and downstream of the first rotor, used to determine the total temperature rise over the first rotor, are also discussed in this section. Ensemble averages of unsteady flow data based on a rotor blade passage period are summarized in the fourth section; the ensemble averages are presented as diagrams for selected blade span locations, as well as contour maps for all tested operation conditions. Ensemble averages based on the rotor revolution period are discussed in the fifth section. Finally, in the sixth section, spectral analysis of unsteady flow parameters is presented. The report is completed with two appendices where performance and dynamic response of thermo-anemometric probes is discussed.

# Contents

# List of Symbols

| | | |
|---|---|---|
| $A_P$ | $[m.s^{-1}]$ | peak amplitude |
| $A_L$ | $[dB]$ | local maximum amplitude |
| $h$ | $[mm]$ | blade span |
| $f$ | $[Hz]$ | frequency |
| $n$ | $[min^{-1}]$ | rotative speed |
| $s$ | $[V]$ | signal voltage level |
| $U_R$ | $[m.s^{-1}]$ | rotational speed at a given radius |
| $U$ | $[V]$ | sensor signal level |
| $V$ | $[m.s^{-1}]$ | mean absolute velocity, velocity amplitude |
| $v'$ | $[m.s^{-1}]$ | fluctuation velocity |
| $z$ | $[mm]$ | spanwise distance (from blade root) |
| $\alpha$ | $[dg]$ | absolute flow angle |
| $\lambda_{ROT}$ | $[dg]$ | rotor circumference |
| $\Delta E$ | $[V]$ | voltage difference |
| $\delta E$ | $[V]$ | deviation from zero incidence voltage |
| $\Delta T_R$ | $[K]$ | total temperature rise at a given radius (Eqs. 3-1 and 3-2) |
| $\Phi$ | $[1]$ | compressor flow coefficient |
| $\Phi_R$ | $[1]$ | flow coefficient at a given radius (Eq. 3-3) |
| $\Phi(\rho V)$ | $[kg.\ m^{-2}.s^{-1}]$ | merit function |
| $\Psi_R$ | $[1]$ | stage loading factor at a given radius (Eq. 3-4) |
| $\rho$ | $[kg.m^{-3}]$ | air density |
| $\sigma$ | $[m.s^{-1}]$ | velocity unsteadiness |
| $\tau$ | $[ms]$ | time |
| $\tau_{BLP}$ | $[1]$ | normalized period of blade passage |
| $\tau_{ROT}$ | $[1]$ | normalized period of rotor revolution |
| $\eta$ | $[dg]$ | probe incidence angle |
| $\jmath_{A\text{-}RAN}$ | $[1]$ | normalized velocity unsteadiness |

### Subscripts

| | |
|---|---|
| *A-IN* | axial, inlet |
| *A*, *AX* | axial |
| *AV* | average |
| *IN* | inlet |
| *M* | mean |
| *R* | radius, |
| *T, TG* | tangential |

### Abbreviations

| | |
|---|---|
| *AXI* | axial |
| *IGV* | inlet guide vane |
| *LE* | leading edge, |
| *LSAC* | low speed axial compressor |
| *MAG* | magnitude |
| *OPB* | once per blade |
| *OPR* | once per revolution |
| *RB* | rotor blade |
| *RBR* | rotor blade row |
| *SV* | stator vane |
| *SVR* | stator vane row |
| *TAN* | tangential |

# 1.0 Facility Description and Basic Instrumentation

The NASA Glenn Research Center Low-Speed Axial Compressor (LSAC), built to increase the understanding of the complex flow phenomena occurring in multistage compressors, has been heavily used in the past for various research programs, including experiments presented in this report.

## 1.1 Test Facility

Overall views of the NASA research compressor facility are shown in photographs in Fig. 1-1. The air is drawn from the test cell into the plenum provided with flow straighteners (Ref. 1-1). Then air passes through a bellmouth with a *12.7:1* area contraction. The flow then enters the compressor and exits through a throttle valve at the entrance to the collector. The compressor partial cross section and the blade/vane row layout are shown in Fig. 1-2. The research compressor consists of a row of inlet guide vanes (IGV) followed by four identical stages, each having a rotor blade row (RBR) and a stator vane row (SVR). Each rotor has 39 blades, each stator consists of 52 vanes, and there are also 52 vanes in the IGV row. The compressor tip radius is *610 mm*, and blade or vane height is *122 mm*. The aspect ratio (span/chord) is *1.20* for rotor rows and *1.30* for stator rows (Ref. 1-1). The compressor design tip speed is *61.0* $m.s^{-1}$, design mean axial flow velocity is *24.4* $m.s^{-1}$, and the overall pressure ratio is *1.042*. The design flow coefficient is *0.395*. All data presented in this paper were acquired at a constant speed line of *983* $min^{-1}$. At this rotational speed, the rotor shaft frequency was *16.38 Hz*, and the rotor blade passing frequency was *638.95 Hz*. All stator rows can be indexed circumferentially to move across almost two full blade pitches. For this investigation, however, the stator rows were held at fixed positions (including the IGV cascade), and clocked as shown in Fig. 1-2. Average wall clearance for the first rotor was *1.04 mm*, with maximum and minimum values of *1.19* and *0.76 mm*, respectively. The compressor shroud is provided with a number of small access ports for aerodynamic probes.

## 1.2 Basic Instrumentation and Measurement Stations

Both steady-state and unsteady data were acquired during the course of this experimental investigation. The steady state data were acquired using the standard instrumentation as specified in Ref. 1-1. Only basic steady-state parameters, needed to characterize compressor operation conditions, were recorded. Namely, these parameters were: inlet total pressure and total temperature, inlet mean Mach number, overall mass flow rate, flow coefficient, ten static pressures along the compressor shroud, three static pressures on the compressor hub, and actual rotational speed. Standard instrumentation used is described in Ref. 1-1, and calibration of steady-state probes is presented in detail in Ref. 1-2.

Unsteady data were acquired using a thermo-anemometer system. Three types of thermo-anemometer probes were used: a split-fiber probe for measurement of velocity magnitude and direction, and single-fiber and single-wire probes to measure velocity magnitude only. Split-fiber and single-fiber probes are basically film probes with a restricted range of frequency response. Properties of thermo-anemometric probes will be discussed later. Most of the data presented in this report were acquired using the split-fiber probe. Some data acquired by a single-wire probe were used for spectral analysis of velocity fluctuations. The single-fiber probe data acquired were not used at all due to a limited frequency response as discussed later.

All test results, reported here, were acquired in the first stage of the low speed compressor. New access ports were provided over the first compressor rotor to accommodate actuators with thermo-anemometric probes. Layout of measurement stations (ports) is shown in Fig. 1-3. There were four new ports provided for probe traversing; two ports were upstream of the first stage rotor (*S10A* and *S10B*), and two ports were located downstream of the first rotor (*S15A* and *S15B*). Section R-R in Fig. 1-3 shows shape of trailing edges of inlet guide vanes as the flow leaves the IGV cascade, and section S-S depicts shape of leading edges of the first stator as the flow approaches stator vane row (*S1*). The angular positions of the probe ports are measured in the clockwise direction from the top of the compressor

shroud (12 o'clock). Two port locations were selected to provide one measurement station in the midpitch and one in the wake region of the inlet guide vanes. The remaining two ports were for one station in the midpitch and one station in the stagnation region of the first stator vanes.

The thermo-anemometric probes were mounted in specially modified actuators. The tip of the actuator was provided with a protective dome, into which the probe was retracted for the compressor runs when the thermo-anemometric probes were not used or before the actuator was dismounted from the compressor. A drawing of the modified actuator tip is shown in Fig. 1-4. This arrangement proved to be very practical. Not a single thermo-anemometric probe was lost due to handling during the entire program. Further, this arrangement allowed easy frequent transports of the probe between the compressor and the calibration jet facility. Because there was no need to take the split-fiber probe out of the actuator for calibration, the reliability of flow directional measurement improved significantly. A split-fiber probe positioned in the compressor blade passage is shown in Fig. 1-5.

### 1.3 Expected Flow Trajectories

As mentioned above, new probe ports were drilled in the compressor shroud. The selection of these new port locations was based on a requirement that radial traverses in front of the first rotor would be made at midpitch and wake region of the IGV row, and traverses behind the first rotor would be made at midpitch and stagnation region of the SBR cascade. However, the actual locations of these ports were misplaced slightly due to mechanical restrictions on the compressor shroud. In order to select the port locations, expected trajectories of air particles through the compressor first stage were generated, and are shown in Figs. 1-6 through 1-8 for mid span, and tip and root regions of the blades. The diagrams were created based on measured axial velocity, inlet and exit flow angles, and rotational speed. As seen in Fig. 1-6 for the mid span location, the trajectories for measurement stations *S10B* and *S15A* lay very close to each other, and thus it can be expected that the measurements at station *S15A* will be affected to a degree by probe wake generated at station *S10B* if both stations were probed at the same time. Data acquired at station *S10A* are affected by the wake generated by an inlet guide vane; these effects are discussed in the section on averaged radial distributions. Data taken at the measurement station *S15A* are representative for flow at the midpitch region of the first stator, whereas data taken at station *S15B* clearly represent data from the stator vane stagnation region.

Expected air trajectories in the blade root region (Fig. 1-7) differ from the pattern at the mid span height in the previous figure. Measurements in the hub region at station *S15A* might be affected by probe at station *S10A*. The measurements at station *S10B* will be affected by the wake flow shed from an inlet guide vane. The same effect, to a smaller extent, may be expected on data taken at the measurement station *S15A*. Finally, the expected air trajectories at the blade tip are presented in Fig. 1-8. Here, the IGV wakes will affect measurements at stations *S10A* and *S10B*. It seems that at this region there is no effect of probe upstream of the rotor on data collected downstream of the first stage rotor.

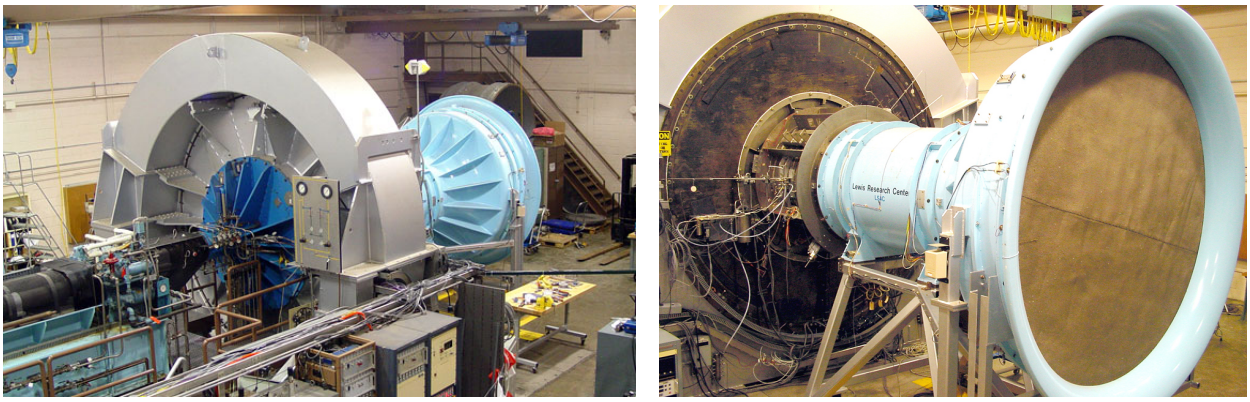

Fig. 1-1. NASA Glenn Research Center low speed axial compressor facility.

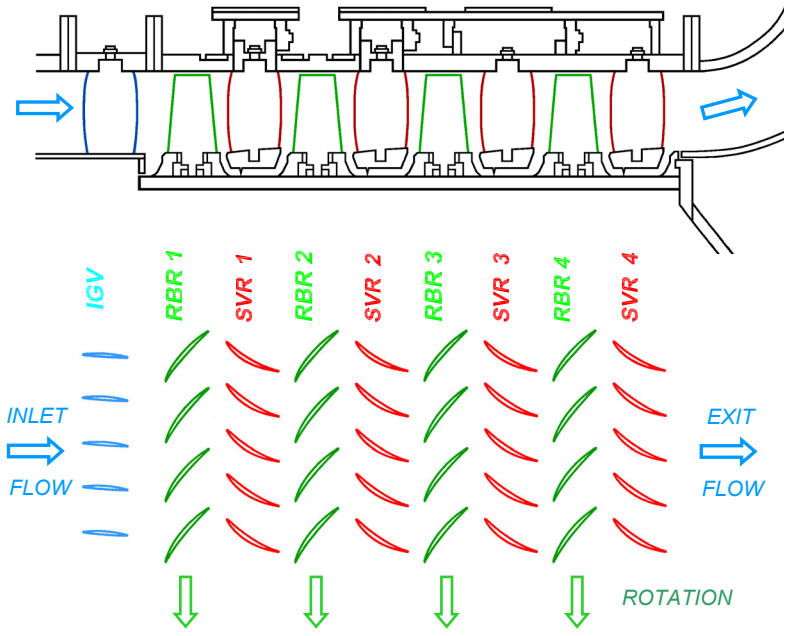


Fig. 1-2. Flow path and blading plan of the NASA low speed axial compressor.

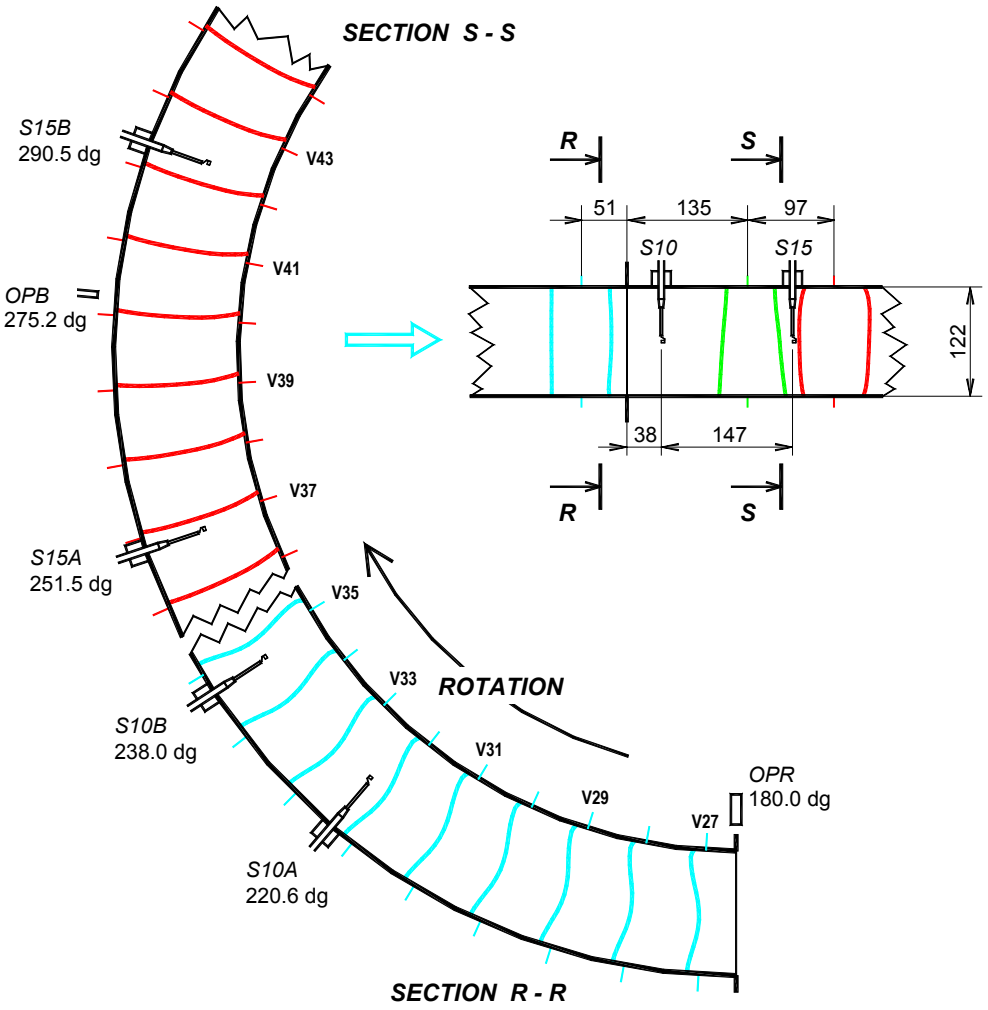


**Fig. 1-3. Layout of measurement stations ( dimensions in *mm* ).**

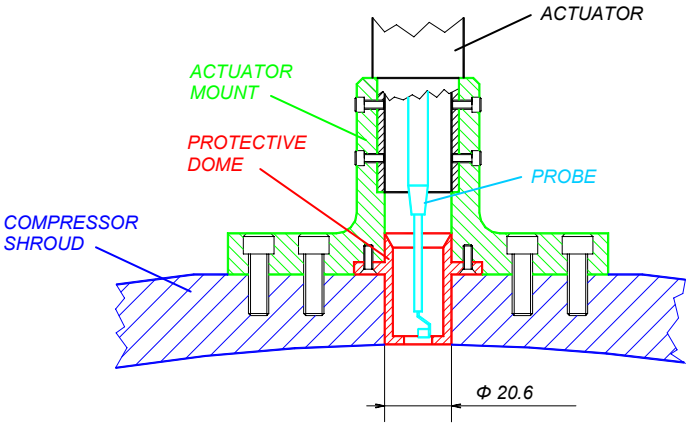


**Fig. 1-4. Modified actuator tip with probe protective dome (dimension in *mm*).**

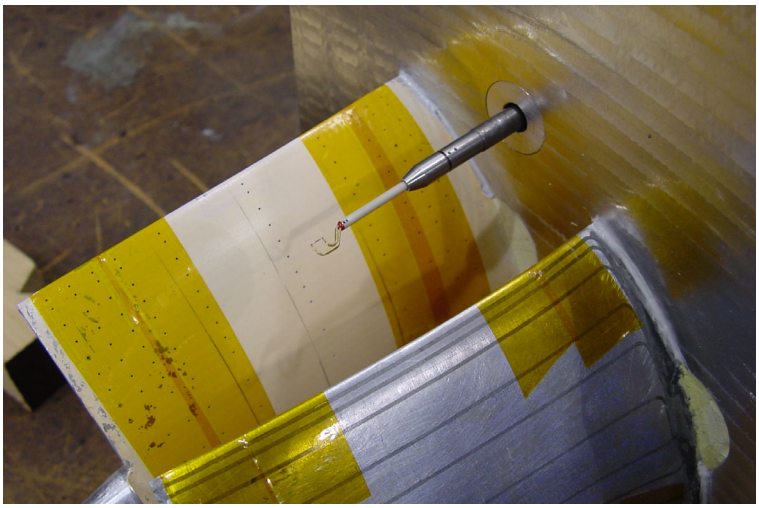

**Fig. 1-5. Split-fiber probe in the blade passage.**

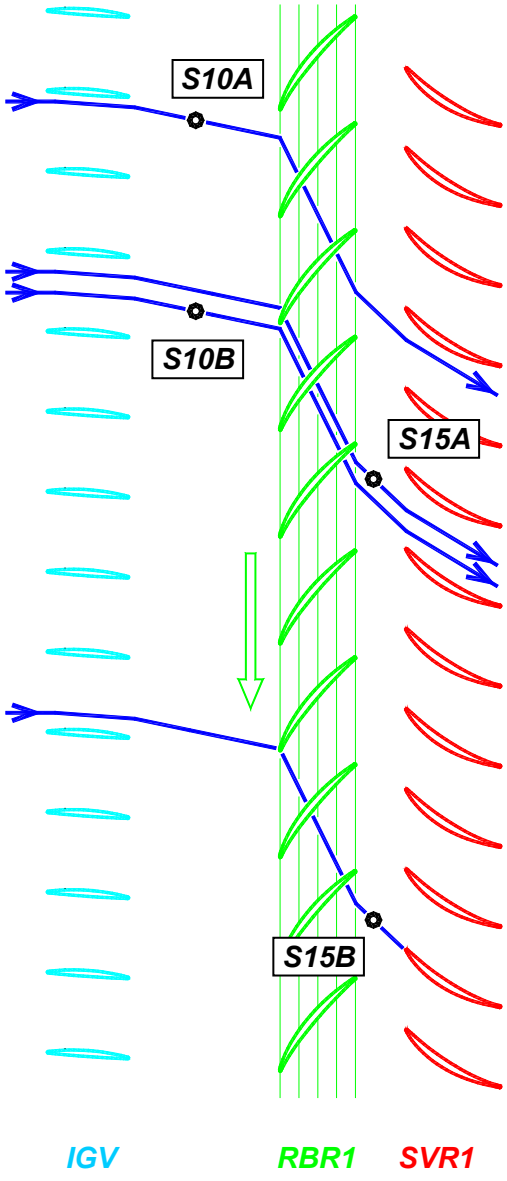


**Fig. 1-6.** **Expected air trajectories through the first stage of the LSAC at the mid span height (*z/h = 0.50*) for a flow coefficient of *0.375*.**

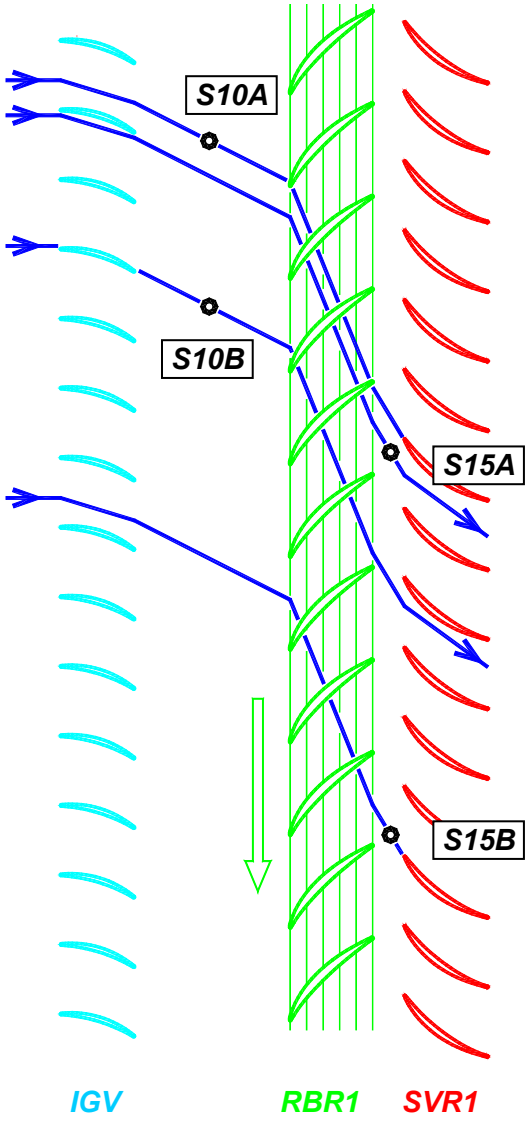


**Fig. 1-7.** **Expected air trajectories through the first stage of the LSAC in the blade root region (*z/h = 0.10*) for a flow coefficient of *0.375*.**

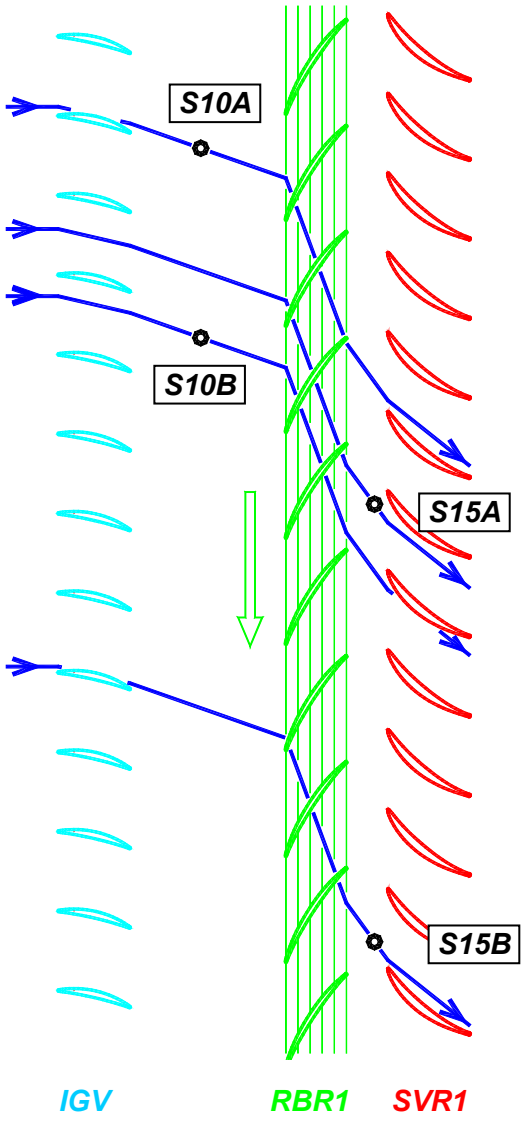


**Fig. 1-8.** **Expected air trajectories through the first stage of the LSAC in the blade tip region (*z/h = 0.90*) for a flow coefficient of *0.375*.**

# 2.0 Unsteady Velocity Measurements

All unsteady data recorded were digitized using *32 kHz* sampling frequency for each data channel. Each record is *5 s* long, which in rounded numbers represents *82* rotor revolutions or *3198* rotor blade passages. In order to avoid aliasing problems, all signals were filtered before digitization. The only filter available was a low pass *10 kHz* filter with a rolloff *60 db* per decade, which was a little bit slow for perfect anti-aliasing.

## 2.1 Thermo-Anemometric Probes

Unsteady velocities were measured using Dantec StreamLine constant temperature anemometer system. Three different types of thermo-anemometric probes were used during these tests: a split-fiber probe (Dantec 55R57), a single-fiber probe (Dantec 55R03), and a single-wire probe (Dantec 55P13). The split-fiber probe consists of two independent nickel films deposited on a quartz cylinder, and thus it can be used to measure simultaneously two velocity components (velocity magnitude and velocity angle) in a plane perpendicular to the probe cylinder. Both velocity components are measured simultaneously, which allows determination of the Reynolds shear stress component in the unsteady flow. The diameter of the quartz cylinder (fiber) is *200 μm*. The active length of the sensors is *1.25 mm*. The probe is shown in Fig. 2-1; the probe features are discussed in Ref. 2-1. The single-fiber probe has one nickel film deposited on a quartz cylinder *70 μm* in diameter. Finally, the single-wire probe consists of a platinum-plated tungsten wire 5 *μm* in diameter. Both single element probes have the same active length of *1.25 mm*.

The split-fiber probe diameter, however, is 40 times larger than the diameter of the single-wire probe, and hence the dynamic response of the split-fiber probe is reduced in comparison with a single-wire probe. The frequency response of the single-wire probe was determined using a square-wave test (Ref. 2-2). The test indicated that the wire probe has a flat characteristic (within *3 dB*), up to a cut-off frequency of *75 kHz*. It has been established that the cut-off frequency of single wire probes drops with increasing wire diameter. The theory of the square wave test has not yet been developed for fiber probes, and the square-wave test is deemed not to be reliable for these probes (Ref. 2-3). It is generally accepted that the hot-film probes have lower frequency response than hot-wire probes. The reasons for the lower frequency response are at least two: (1) a large size of fiber probes, and (2) the thermal inertia of the substrate fiber. However, in the case of fiber probes, the cut-off frequency does not necessarily decrease with an increasing fiber diameter. Surprisingly, the experience shows that within a certain diameter range, the cut-off frequency of fiber probes increases with increasing fiber diameter (Ref. 2-3). This trend was confirmed by comparing turbulence intensity measurements in a free jet using single-wire and fiber probes (Ref. 2-4). It is a fact that with fiber probes only a very thin film on the fiber surface (about *0.5 μm* thick) is heated, while the core (the fiber) is not (Ref. 2-5). Rapid changes in heat transfer due to velocity unsteadiness affect mainly the thin film and the fiber core, due to its very low heat conductivity, is affected very little. Most likely, the optimum sensitivity and time response to rapid velocity changes is also a function of probe diameter. The measurements in a free jet (Ref. 2-4) and subsequent frequency analysis indicate that the frequency response of a split-fiber probe (Dantec 55R57) is flat up to at least *10 kHz*, while a single-fiber probe (Dantec 55R03) has a flat frequency characteristic only to *5 kHz*.

## 2.2 Probe Spatial Resolution

All three thermo-anemometric probes were oriented with their sensing elements in the radial direction, in order to detect velocity variation in the axial-tangential plane. This orientation assured maximum spatial resolution in the plane with largest directional changes of the velocity vector. As seen in Fig. 2-2, spatial resolution of thermo-anemometric probes in the axial-tangential plane is superior to the spatial resolution of standard probes used for steady state measurements (Ref. 1-1). Probe characteristic contours in the axial-tangential plane are shown in scale together with the rotor blade trailing edge shape

for direct comparison. The diameter of the largest thermo-anemometric probe (split-fiber probe) is only *0.2 mm*, whereas the inlet diameter of the kiel total pressure probe is *1.63 mm*.

In the radial direction, however, the situation is different. As already mentioned the length of the sensing element for all three thermo-anemometric probes is *1.25 mm*, which is comparable with the standard probe resolution. The rotor blade height is *122.0 mm*, and thus the length of the sensing element is about *1%* of the blade height. Such spatial resolution is more than sufficient for most of the blade with exception of the blade tip. The average blade tip clearance is only *1.04 mm*, which is less then the sensor length.

The situation at the blade tip is depicted in Fig. 2-3. A thermo-anemometric probe in this figure is positioned at a location $z/h = 1.0$. As can be seen here, half of the sensing elements protrudes in the flow and spans for nearly the entire blade tip clearance. The clearance flow certainly exhibits rapid velocity gradients, but the probe yields a signal which represents a velocity value that is probably close to an average value over a wetted portion of the sensor surface. Thus the velocity data acquired within the blade tip gap most likely exhibit velocity gradients that are smaller than are the actual ones.

### 2.3 Signal Decomposition Procedure for Split-Fiber Probes

Calibration and data reduction procedures for single-wire and single-fiber probes are well established and described (Ref. 2-2). In the work presented in this report, an inverse form of a polynomial fit of calibration data was adopted (Ref. 2-4). For a split-fiber probe, however, there is no established procedure for signal decomposition into velocity magnitude and velocity direction components, and an in-house developed procedure, described below, was adopted.

An iterative data reduction (signal decomposition) procedure was developed in house (Ref. 2-2). Later, this procedure was modified to avoid convergence problems (Ref. 2-4). The modified procedure is not an iterative process but it is based on the minimum value of a merit function that is built over the entire range of $\rho V$ values for which the probe was calibrated. A flow chart of the modified signal decomposition procedure is in Fig. 2-4. First, the voltage difference $\Delta E(\eta)$ from the test data between sensors 1 and 2, $E1(t)$ and $E2(t)$, is determined for a specified time instant ($t$). Then, the procedure scans through a predetermined range of $\rho V$ values (independent variable), and for each $\rho V$ value finds dependable parameters in differential (*STEP 1*), and directional (*STEP 2*) characteristics. In the first step a value of flow angle $\eta(t)$ is found in a differential characteristic, which corresponds to a $\rho V$ value used.

In the second step a directional characteristic is employed that again is proper for the current $\rho V$ value. In this characteristic, voltages $E1(\eta,\rho V)$ and $E2(\eta,\rho V)$ are found, and the difference $\Delta E(\rho V) = E1(\eta,\rho V)-E2(\eta,\rho V)$ is calculated. While this process repeats for each throughflow density value until the entire range of preselected $\rho V$ values is utilized, a merit function is being built. Values of the merit function, $\Phi(\rho V)$, are calculated as squares of the difference $\Delta E(\eta) - \Delta E(\rho V)$. In the third step a $(\rho V)_M$ value, for which the merit function reaches its minimum, is found. Ideally, this value should be the actual throughflow density in the flow for the given instant $t$. As seen here, the entire process is performed in the domain of directional characteristics. Now, knowing the incidence, and using the zero flow angle voltages ($E1_0$, $E2_0$), determined during probe calibration, voltage corrections to remove directional effects ($\delta E1(\eta)$, $\delta E2(\eta)$) can be applied to test data voltages. The corrected voltages (free of directional bias) are used in the fourth step as inputs into velocity characteristics of both sensors to determine throughflow densities $(\rho V)_1$ and $(\rho V)_2$, as measured by each sensor. Ideally the three values $(\rho V)_1$, $(\rho V)_2$ and $(\rho V)_M$ are identical; in reality they differ usually within *3%* of their average value. These three values are monitored during the data reduction process. Test data for which the difference among these values is larger than *3%* are discarded. The procedure is very fast; to reduce a data set of *160000* entries takes about *90 s* on a current personal computer.

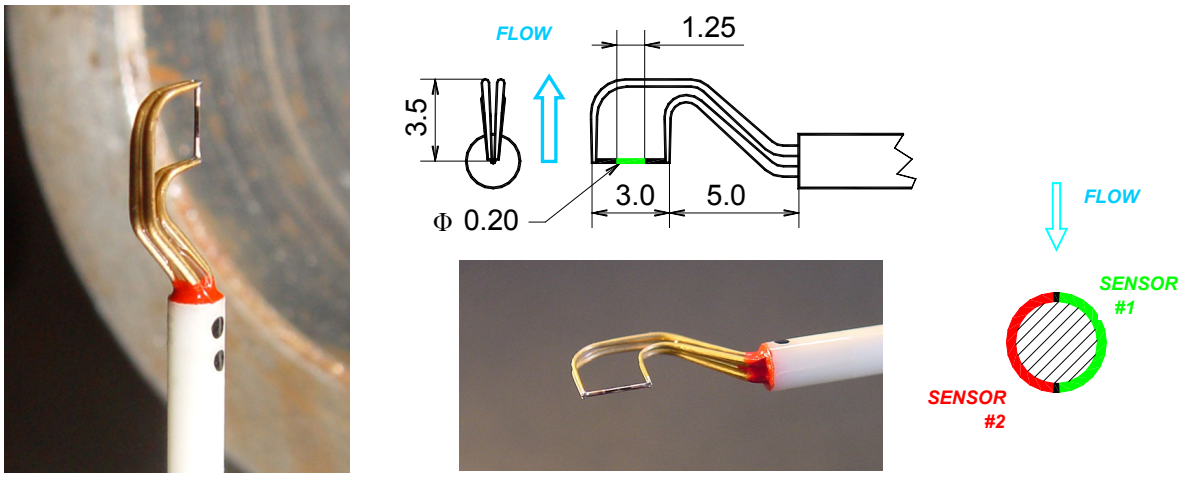


**Fig. 2-1. Split-fiber probe Dantec 55R57 (dimensions in mm).**

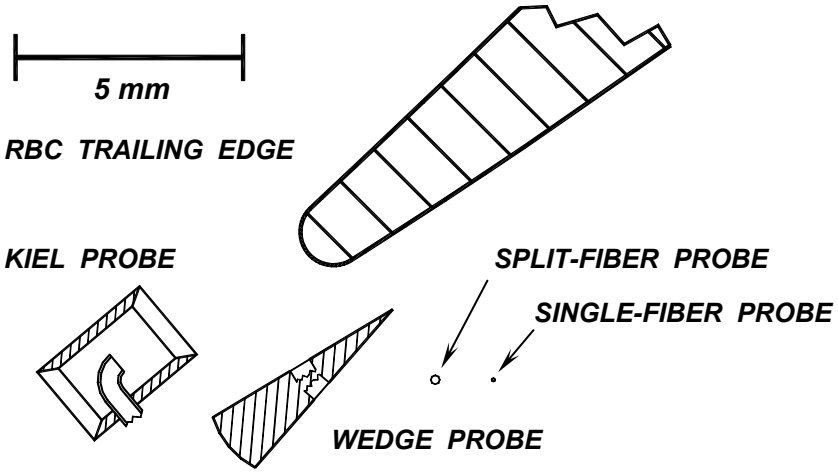


**Fig. 2-2. Comparison of probe sizes in the axial-tangential plane.**

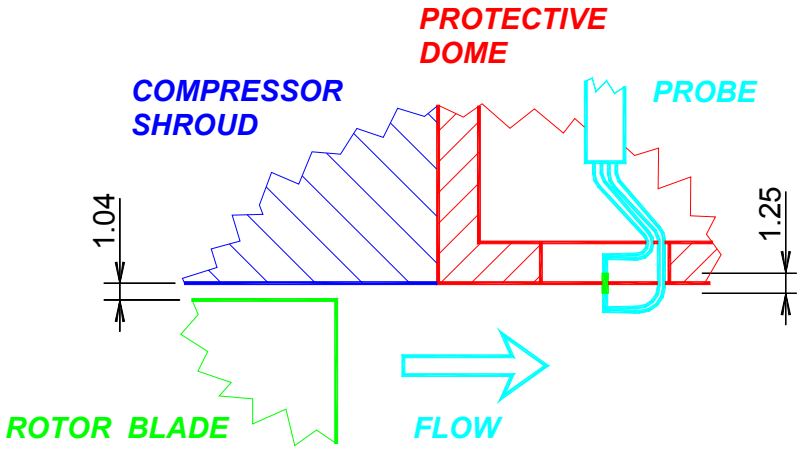


**Fig. 2-3. View of split-fiber probe and blade tip clearance (dimensions in *mm*).**

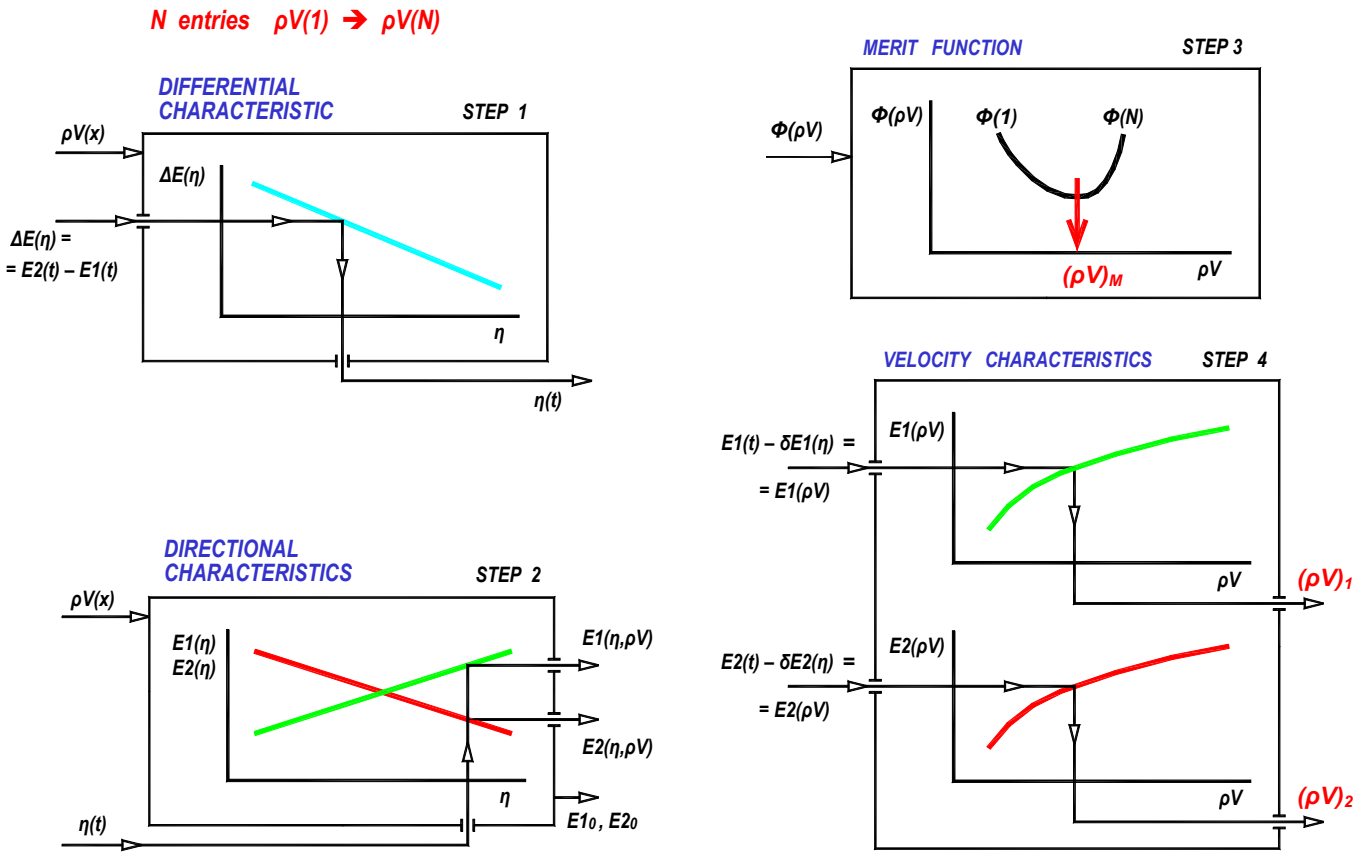


**Fig. 2-4. Flow chart of the modified signal decomposition procedure for a split-fiber probe.**

# 3.0 Averaged Radial Distributions

Experimental data that were acquired for three operation conditions, characterized by flow coefficients of nominal values of *0.340*, *0.375*, and *0.395*, are presented in this section. The flow coefficients are for the compressor design point operation ($\Phi = 0.395$), peak efficiency operation condition ($\Phi = 0.375$), and the near stall operation point ($\Phi = 0.340$). All data presented in this section were acquired by split-fiber probes. Time histories of unsteady velocities along the blade passage height, each of them in duration of *5 s,* which is equaled to *81* rotor revolutions, were averaged and plotted for all four measurement stations at the first rotor. A good test for verifying the reliability of the split-fiber probe data is comparison with mean velocity and flow angle data acquired by pneumatic probes. Conventional pneumatic probes used for these measurements are described in Refs. 1-1 and 1-2. Detail comparison of pneumatic probe data with split-fiber probe data is presented in Refs. 2-1, 2-4, and 2-6, and will not be repeated here. In summary the agreement between the pneumatic cobra probe data and data for split-fiber probe is very good; the differences in velocity magnitude are less than *2 %*, and the maximum difference in flow angle measurement is less than *2.5 dg*.

## 3.1 Near Stall Velocity Data Upstream of the First Rotor

The results for a flow coefficient of approximately *0.340*, which was the last stable operation point before the rotating stall instability occurred, for both measurement stations upstream of the first rotor are presented in Figs. 3-1 and 3-2. In these figures, radial (blade span) distribution of velocity magnitude is depicted in the left upper diagram. The next diagram in the same row presents distributions of velocity unsteadiness that was determined as a ratio of standard deviation of the entire unsteady velocity data segment ($v'$) and the average inlet axial velocity ($V_{A\text{-}IN}$). There are two distributions of velocity unsteadiness in this diagram that are barely distinguishable for the measurement station upstream of the first rotor. The first one is a distribution of unsteadiness of the velocity magnitude (labeled *MAGNITUDE*), which indicates the unsteadiness that would be measured by a single-fiber or single-wire probe that is insensitive to velocity direction in the plane perpendicular to the sensing element (Refs. 2-1 and 2-4). The second distribution in the same diagram is velocity unsteadiness (labeled *AXI+TAN*) that is determined as a vector addition of axial velocity unsteadiness and tangential velocity unsteadiness measured by a split-fiber probe. The unsteadiness is normalized by the average inlet axial velocity. The identity of the velocity magnitude and velocity unsteadiness distributions for stations *S10A* and *S10B* indicates that there are no angular fluctuations of the velocity vector at the exit from the IGV row (a detailed explanation is in the section 3.2). Finally, the last diagram in the first row shows the distribution of the absolute flow angle. Axial velocity and unsteadiness distributions are shown in the second row of diagrams, whereas tangential velocity and unsteadiness distributions are shown in the first two diagrams in the third row. The last diagram in the right lower corner shows distribution of a Reynolds term along the passage height. The Reynolds term is defined here as a time average of instantaneous products of axial and tangential velocity fluctuations generated over the entire interval of *5 s*. A small cartoon in the second row depicts the location of the probe in relation to the compressor IGV or first stator vanes for a mid span location.

The data acquired at station *S10A* (Fig. 3-1) shows two crossings of the wake generated by the inlet guide vane. This is due to the fact that the probe traversed the blade passage in a radial direction whereas the IGV trailing edge was highly curved. The situation is explained in Fig. 3-3 where IGV profiles and 'metal' angles (broken blue lines) are shown at several radial stations together with the probe locations, and they are associated with the measured velocity data. As seen here, as the probe was moved downwards along the vane it is washed by flow from the vane suction side (green arrows and symbols), then at about *78%* of the vane height ($z/h = 0.78$ in the left hand side diagrams in Fig. 3-3) the wakes move across, and the probe is washed by the flow from the pressure side of the vane (red arrows and symbols). The second wake crossing occurs at about *40%* of the vane height. Crossing the wake significantly affects velocity, velocity unsteadiness, and flow angle radial distributions. At station *S10B* (Fig. 3-2) there is no wake crossing because the probe is traversed in the mid pitch region of the vane channel far from the wakes. Consequently, radial distributions of flow parameters are smooth, without any abrupt changes at this probe port.

### 3.2 Near Stall Velocity Data Downstream of the First Rotor

Results of velocity measurements downstream of the first rotor are presented on Figs. 3-4 and 3-5. The data were taken at measurement stations *S15A* and *S15B* for a near stall operation point of $\Phi = 0.340$. The plots are arranged in the same way as already described for the measurement stations upstream of the first rotor.

A noticeable difference between these data and data measured upstream of the rotor is in the distributions of velocity unsteadiness. As seen here, distributions, labeled *MAGNITUDE* and *AXI+TAN*, are not identical any more. This indicates that there was a strong time dependence of the velocity direction at the exit plane from the rotor row (stations *S15A* and *S15B*) as the rotor wakes are passing the probe. This is demonstrated by noticeably higher velocity unsteadiness in comparison with the velocity magnitude unsteadiness. As mentioned above, the magnitude unsteadiness represents data taken by a single-wire (or fiber) probe, and the velocity unsteadiness represents data taken by a split-fiber probe. In this particular case, both unsteadiness distributions were generated from split-fiber probe data; the magnitude unsteadiness was used for verification of the signal decomposition procedure applied to split-fiber probe data by comparison with true single-wire probe results (Ref. 2-4).

A single-wire probe perpendicular to the axial-tangential plane measures fluctuations of the velocity magnitude only. Because the probes were attached to the absolute frame of the compressor stator, the velocity fluctuations, generated in the relative system of the compressor rotor, were measured in their transformed form in the absolute frame. This transformation imposes a severe limitation on the ability of a single-wire probe to measure the velocity fluctuations as explained next. Let us assume a specific case when the conversion from the relative to the absolute system results in velocity $V_M$ that has a constant magnitude and oscillates about a mean direction $\alpha$ by $\pm\Delta\alpha$ (Fig. 3-6). The velocity components oscillate about $V_X$ by $\pm v_X$ and about $V_Y$ by $\pm v_Y$. Obviously, if the fluctuations $v_X$ and $v_Y$ are measured, the resulting overall fluctuations of the velocity vector $V$ can be calculated and velocity unsteadiness is then a ratio of the overall velocity fluctuations and the velocity magnitude. However, measurement of the velocity vector $V_M$ with a single-wire probe, which is insensitive to flow direction, results in a constant value (the $V_M$ magnitude is constant), and consequently the apparent velocity unsteadiness is zero. This is due to the fact that a single-wire thermo-anemometric probe converts a vector value (magnitude and angle) into a scalar value (electric voltage proportional velocity magnitude).

Radial distributions measured at stations upstream of the first stator (*S15A* and *S15B*) also exhibit differences between the mid pitch (Fig. 3-4) and vane stagnation (Fig. 3-5) regions. Generally, the axial velocity is smaller over the entire vane span in the stagnation region, while the velocity magnitude and the tangential velocity component are smaller mainly in the upper half of the blade passage. The absolute flow angle in the lower half of the passage is larger in the stagnation region than the one in the mid pitch region. It must be remembered, however, that the stator vane leading edge is lightly curved (see Fig. 1-3), which certainly contributes to the observed changes in flow parameters. The velocity unsteadiness level is about the same for both mid pitch and stagnation regions.

### 3.3 Rotor Velocity Data for all Operation Conditions

Radial distributions of averaged flow parameters for all tested operation conditions are presented in Figs. 3-7 through 3-10. These figures have similar structure to that described above, except that the diagrams of Reynolds terms are omitted. For clarity, distributions are shown as smooth lines with no symbols for individual test points. Each figure summarizes three operation conditions, characterized by nominal flow coefficients of *0.340*, *0.375*, and *0.395* distinguished by color, red, blue, and green, respectively.

As seen for measurement stations *S10A* (Fig. 3-7) and *S10B* (Fig. 3-8) past the IGV row (ahead of the first rotor), decreasing flow coefficient decreases velocity magnitude but does not affect absolute velocity angle. Consequently, both axial and tangential velocity components also decrease, although the decrease of the tangential component is barely traceable due to a small flow angle. Normalized velocity unsteadiness is not affected by a decreasing flow coefficient.

The situation is quite different for measurements past the first rotor (stations *S15A* and *S15B*, Figs. 3-9 and 3-10, respectively). Here, the mean absolute velocity magnitude is substantially independent of the changes in flow coefficient. Flow angle, however, strongly increases with decreasing flow coefficient, as does the axial velocity component. The tangential velocity increases. Velocity unsteadiness levels visibly increase, in particular for the operation conditions close to the rotating stall regime.

### 3.4 Temperature Rise Over the First Rotor

As stated above and argued in Appendix A and B, it is believed that the flow velocity and its components, measured by split-fiber probes, represent a reliable experimental data set that can be used for determining other flow parameters that are extremely difficult to measure. One such parameter is a rise in total temperature across the rotor. In this particular case of a low speed axial compressor, the total temperature rise is very small in absolute terms, and of the order of the error band for the existing experimental techniques for flow temperature measurements.

Assuming that the specific heat stays constant as the flow passes through the rotor then for a streamline the total temperature rise across the rotor can be determined by equation Eq. 3-1 (Ref. 3-1):

$$\Delta T_{SL} = \frac{U_{T\_15} * V_{T\_15} - U_{T\_10} * V_{T\_10}}{c_P} \tag{3-1}$$

where $\Delta T_{SL}$ $[K]$ is total temperature rise in a streamline,
$U_{T\_15}$ $[m.s^{-1}]$ is rotational speed behind the rotor (station *S15*),
$U_{T\_10}$ $[m.s^{-1}]$ is rotational speed in front of the rotor (station *S10*),
$V_{T\_15}$ $[m.s^{-1}]$ is tangential velocity behind the rotor (station *S15*),
$V_{T\_10}$ $[m.s^{-1}]$ is tangential velocity in front of the rotor (station *S10*),
$c_P$ $[J.kg^{-1}.K^{-1}]$ is air specific heat at constant pressure.

For strictly two dimensional flow in the axial-tangential plane, implying no radial shift of streamlines in the rotor, this equation can be simplified to a form shown in Eq. 3-2. Tangential velocities are now associated with the rotor radius (blade height) rather than with a streamline.

$$\Delta T_R = \frac{U_R * \left(V_{T\_15} - V_{T\_10}\right)}{c_P} \tag{3-2}$$

Symbols in the above equation are
$\Delta T_R$ $[K]$ is total temperature rise at a given radius (blade height),
$U_R$ $[m.s^{-1}]$ is rotational speed at a given radius (blade height).

The total temperature rise along the blade span can be determined only for the measurement stations where the tangential velocities were measured. There are four possible combinations among the measurement stations: *S15A - S10A*, *S15A - S10B*, *S15B – S10A*, and *S15B – S10B*. A summary of the results obtained is shown in Fig. 3-11. Three diagrams in the left hand column depict the total temperature rise between station *S15A* past the rotor and stations *S10A* (red curve) and station *S10B* (blue curve) in front of the rotor. The right hand column is for temperature rise between stations *S15B* and *S10A* (green curve), and stations *S15B* and *S10B* (black curve). The average values across the entire blade span for each operating conditions are on the right off the diagrams. As seen here, the total temperature rise increases as the compressor operation point is forced to lower flow rates. There is practically negligible difference in average temperature rise values between data for either measurement station in front of the rotor (*S10A* versus *S10B*). However, there is a noticeable difference in results for measurement stations past the rotor (*S15A* versus *S15B*; left column diagrams versus right column diagrams). The total temperature rise is always lower for measurement station *S15B*. At this station the probe traversed the flow in the stagnation region of a stator vane (as can be seen in Figs. 1-6 through 1-8), whereas at station *S15A*, the probe traversed the flow of the suction side of the closest stator vane. At station *S10A* the probe was traversed through the wake region of an inlet guide vane (see Fig. 3-7). The wake crossing has visible

but only local effects on temperature rise distribution, and the effects on average temperature rise are nearly negligible.

### 3.5 Flow Coefficient and Stage Loading

Components of the unsteady velocity vector can also be used to quantify two important nondimensional parameters, flow coefficient $\Phi$, and stage loading factor $\Psi$, which characterize the compressor operation condition. Definitions of these parameters is given in Ref. 3-2. Customarily, the flow coefficients are based on the inlet average axial velocity ahead of the IGV row. The flow coefficient used throughout this report to describe the operation condition of the entire four stage axial compressor is based on this definition, and was determined using the basic steady state instrumentation (Ref. 1-1) measuring the overall mass flow through the compressor. However, to characterize the first stage only, the flow coefficient ($\Phi_R$) was based on axial velocity measured in front of the rotor (i.e., behind the IGV row), simply because the velocity flowfield upstream of the IGV row was not probed.

The definitions of flow coefficient and stage loading factor for the compressor first stage are given as follows.

$$\Phi_R = \frac{V_{A\_10}}{U_R} \tag{3-3}$$

where $\Phi_R$ [*1*] is the first stage flow coefficient,
$U_R$ [$m.s^{-1}$] is rotational speed,
$V_{A\_10}$ [$m.s^{-1}$] is axial velocity in front of the rotor (station *S10*),

$$\Psi_R = \frac{V_{T\_15} - V_{T\_10}}{U_R} \tag{3-4}$$

where $\Psi_R$ [*1*] is the first stage loading factor,
$U_R$ [$m.s^{-1}$] is rotational speed,
$V_{T\_15}$ [$m.s^{-1}$] is tangential velocity behind the rotor (station *S15*),
$V_{T\_10}$ [$m.s^{-1}$] is tangential velocity in front of the rotor (station *S10*).

Flow coefficient and stage loading factor distributions along the rotor blade span are plotted in Fig. 3-12. The distributions are shown for compressor flow coefficients of *0.395*, *0.375*, and *0.341*. The compressor flow coefficient is based on average inlet velocity, determined from measured mass flow rate, and rotor blade tip speed. The values of rotor flow coefficients averaged over the blade height were corrected for the blade tip speed, and are also given in the diagrams. The average values of rotor flow coefficients are about the same for both measurement stations *S10A* and *S10B*. It looks like the velocity defects due to wake crossing at station *S10A* are compensated by a faster velocity decrease at the rotor hub for station *S10B*. The reason for this rapid velocity drop at the rotor hub can be traced in Fig. 1-7. As seen here, the probe at station *S10B* is becoming affected in the hub region by an IGV wake flow. The averaged flow coefficients have about *3 %* higher values than coefficients based on compressor inlet flow. Considering that the rotor flow coefficients were determined from only two radial traverses instead of from the entire flow area, the agreement with inlet flow coefficients is very good.

The character of the stage loading factor distributions follows the trends discussed for the total temperature rise distributions. The stage loading exhibits a local peak at the blade tip region and then steadily increases toward the second local peak at the rotor hub. This increase in loading seems to be more rapid for station *S15B* where the probe is traversed through the stagnation region of a stator vane as can be traced in Figs. 1-6 through 1-8. The average loading factor values, shown in Fig. 3-12, were corrected for the blade tip speed. The average loading factors based on upstream station *S10A* (IGV wake crossings) show consistently slightly lower values than the ones based on station *S10B*, where the probe was traversed most of the blade height away from the IGV wakes.

***Probe split-fiber R57G, Port S10A, n = 984 min$^{-1}$, Φ = 0.342***

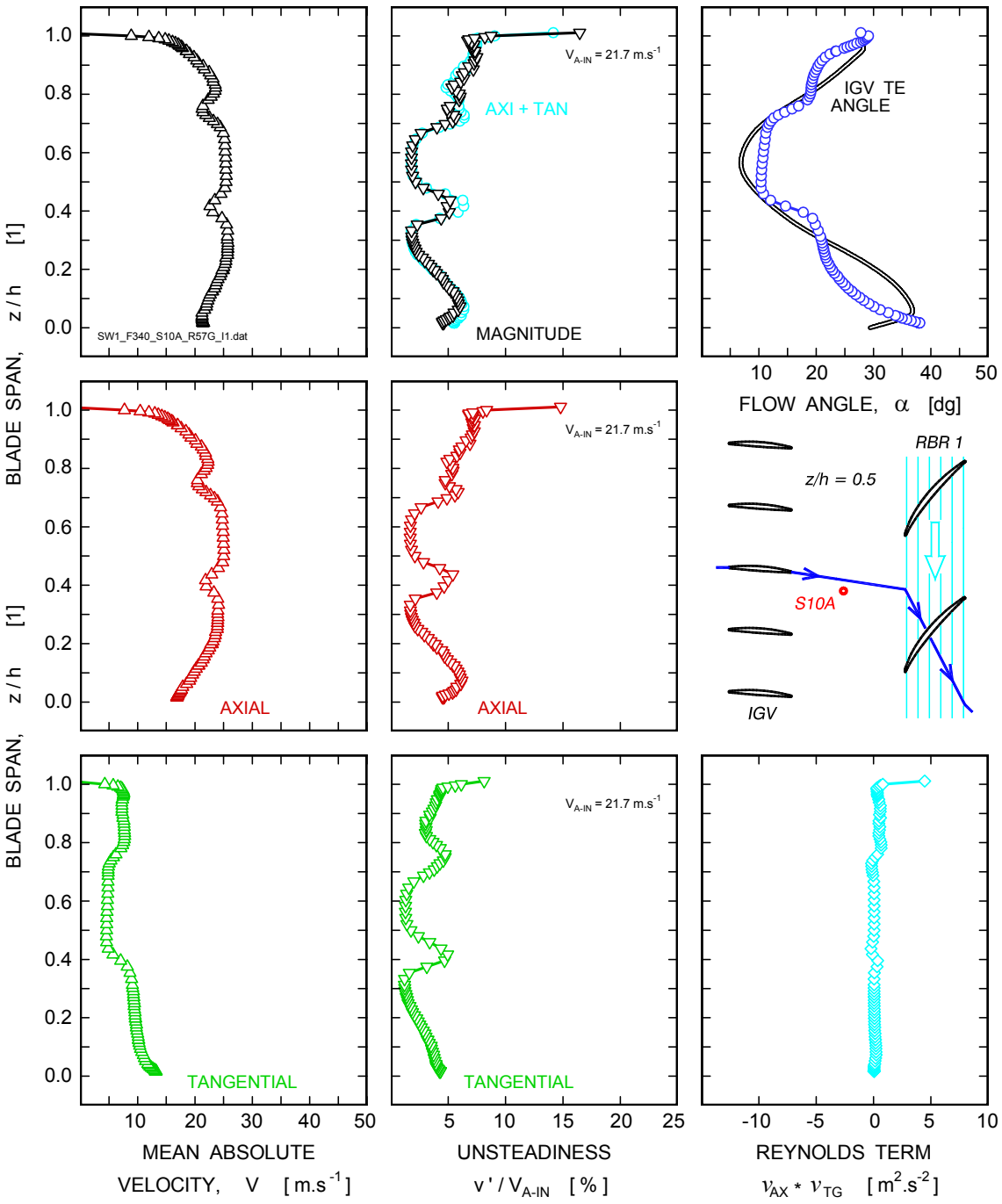


**Fig. 3-1. Radial distributions of flow parameters along the blade passage span behind the IGV row at station *S10A* for flow coefficient of *0.342*.**

***Probe split-fiber R57G, Port S10B, n = 984 min$^{-1}$, Φ = 0.339***

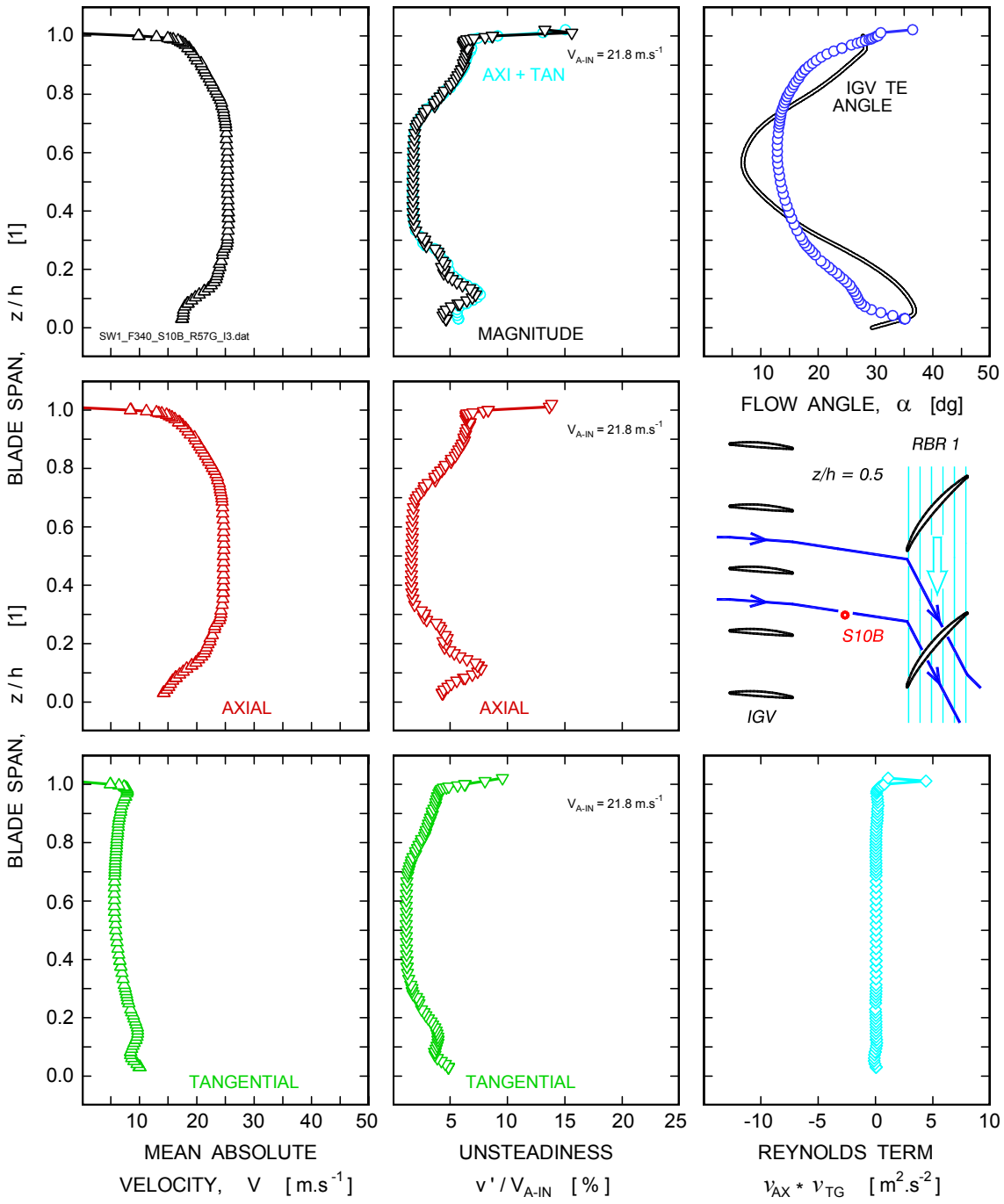


**Fig. 3-2. Radial distributions of flow parameters along the blade passage span behind the IGV row at station *S10B* for flow coefficient of *0.339*.**

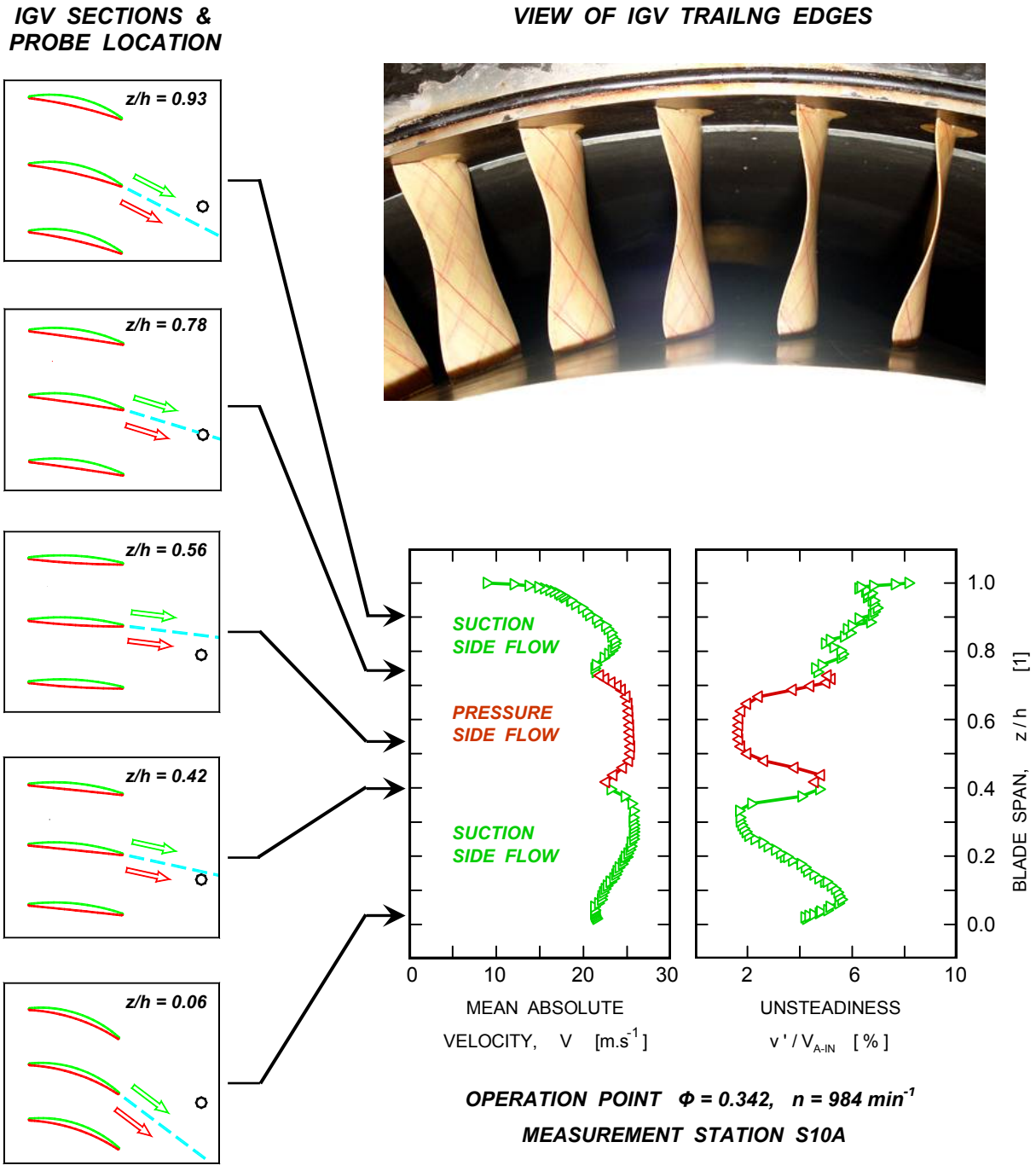


**Fig. 3-3.** **Probe traversing in the IGV wake region (station *S10A*).**

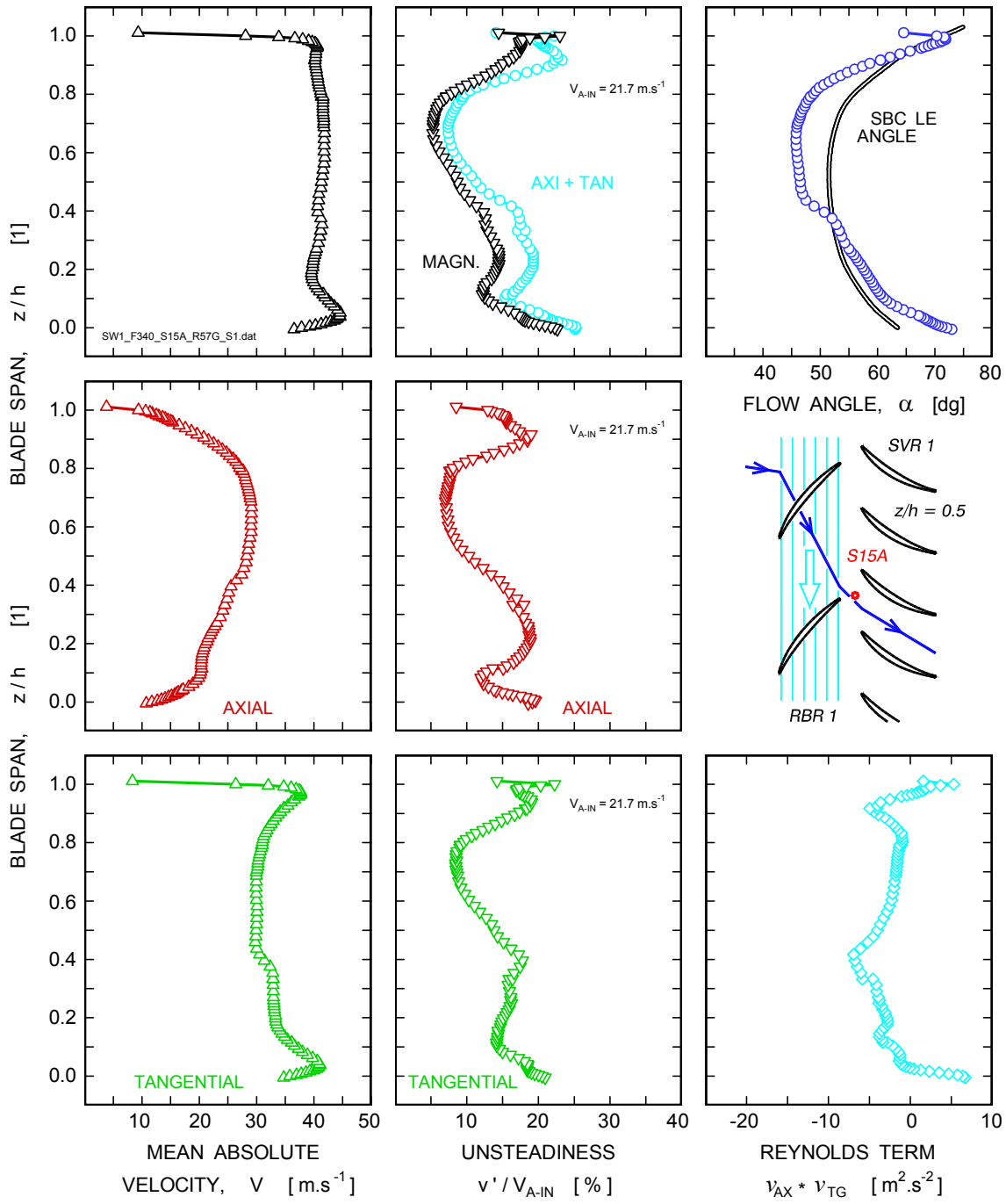


**Fig. 3-4.** **Radial distributions of flow parameters along the blade passage span in front of the first stator row at station *S15A* for flow coefficient of *0.341*.**

***Probe split-fiber R57G, Port S15B, n = 984 min$^{-1}$, Φ = 0.340***

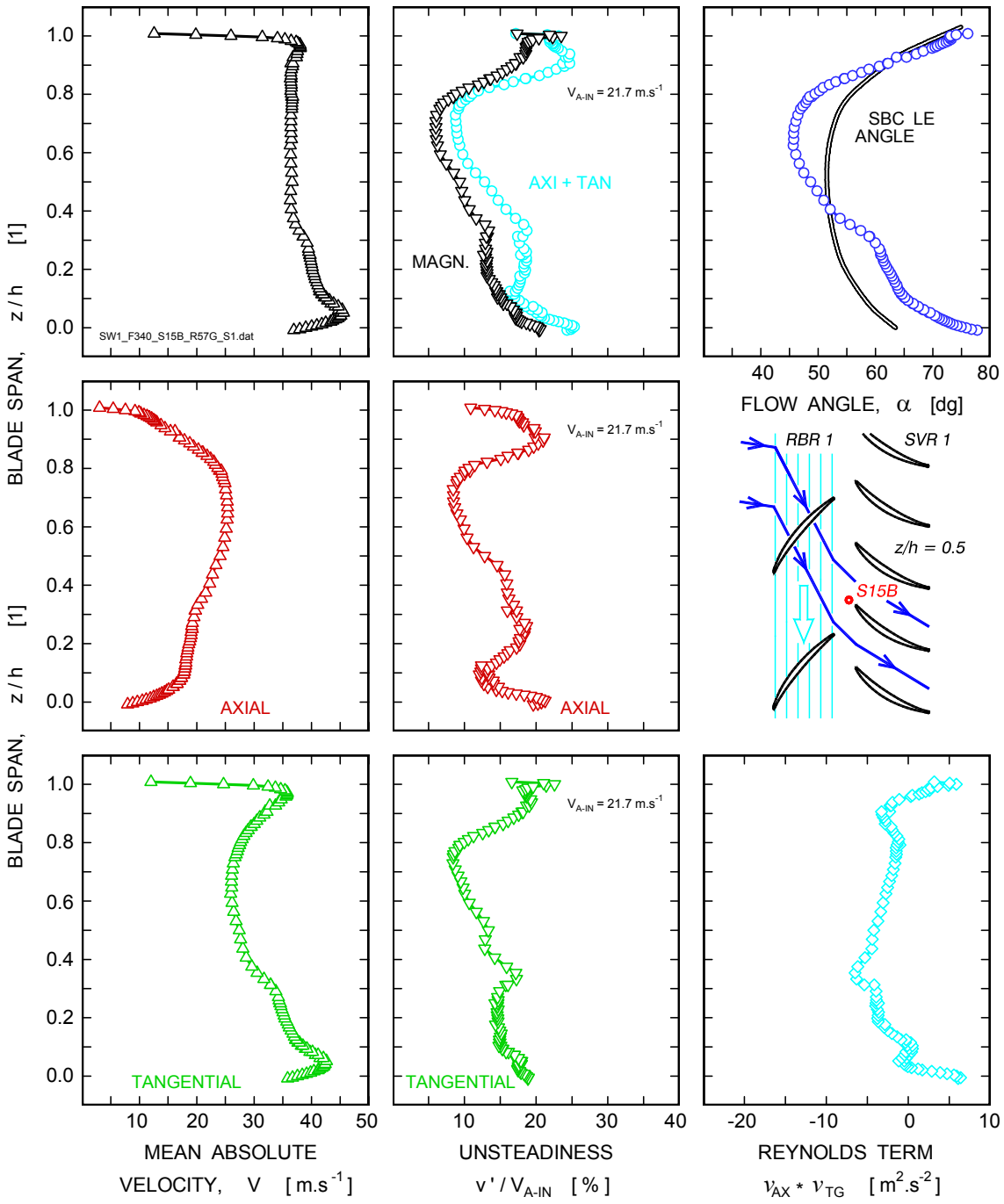


**Fig. 3-5. Radial distributions of flow parameters along the blade passage span in front of the first stator row at station *S15B* for flow coefficient of *0.340*.**

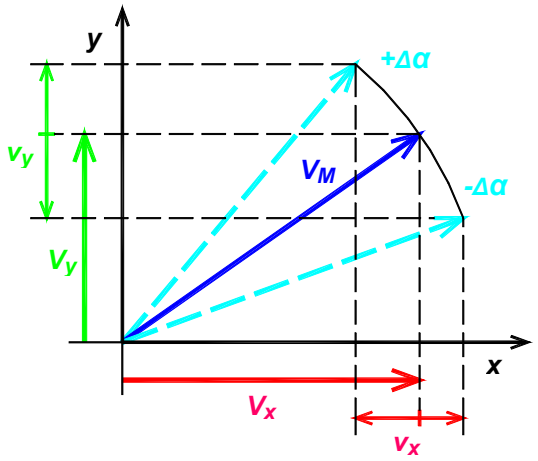


**Fig. 3-6. Oscillation of a velocity vector with constant magnitude.**

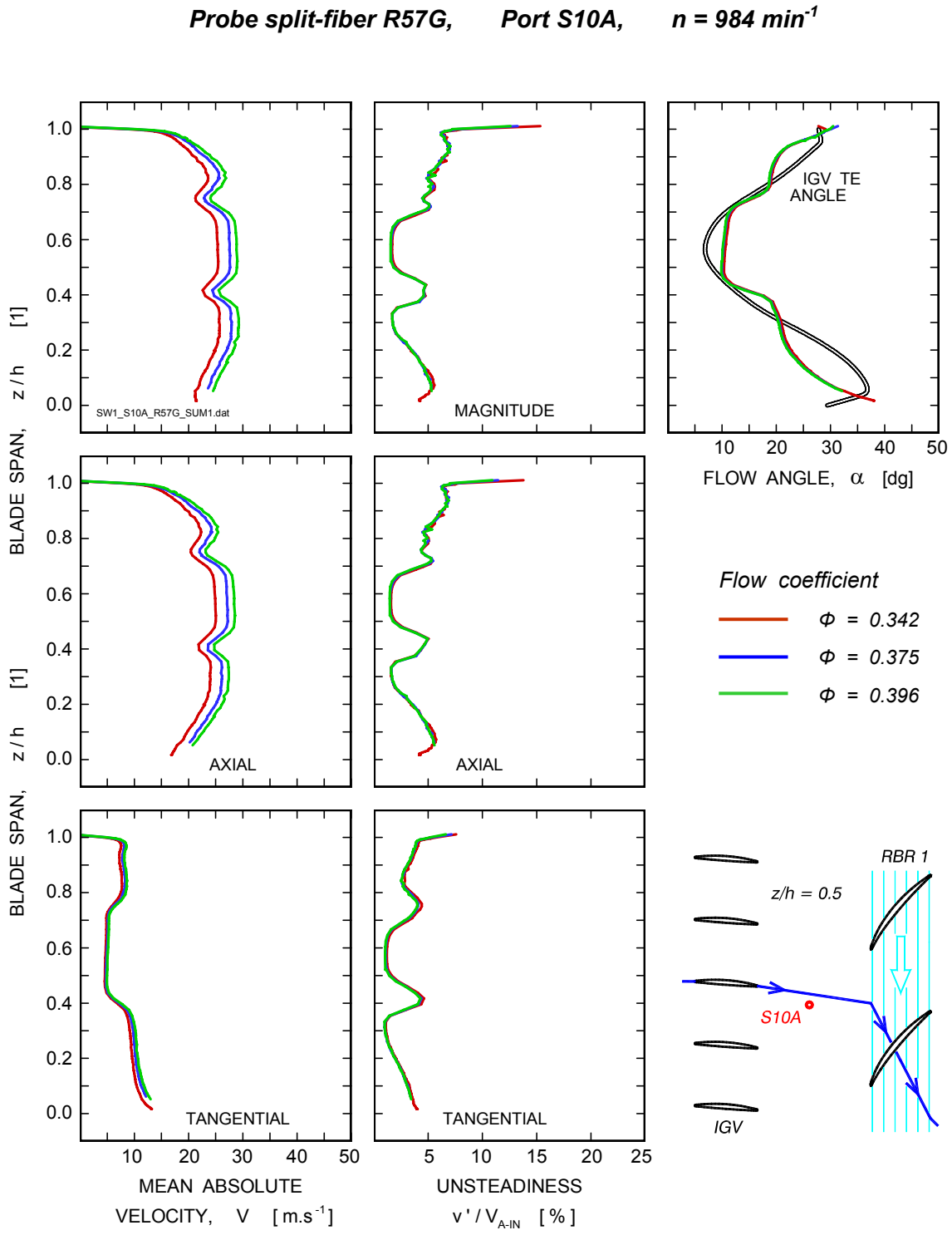


**Fig. 3-7. Comparison of radial distributions of flow parameters along the blade passage span behind the IGV row at station *S10A* for three operation conditions.**

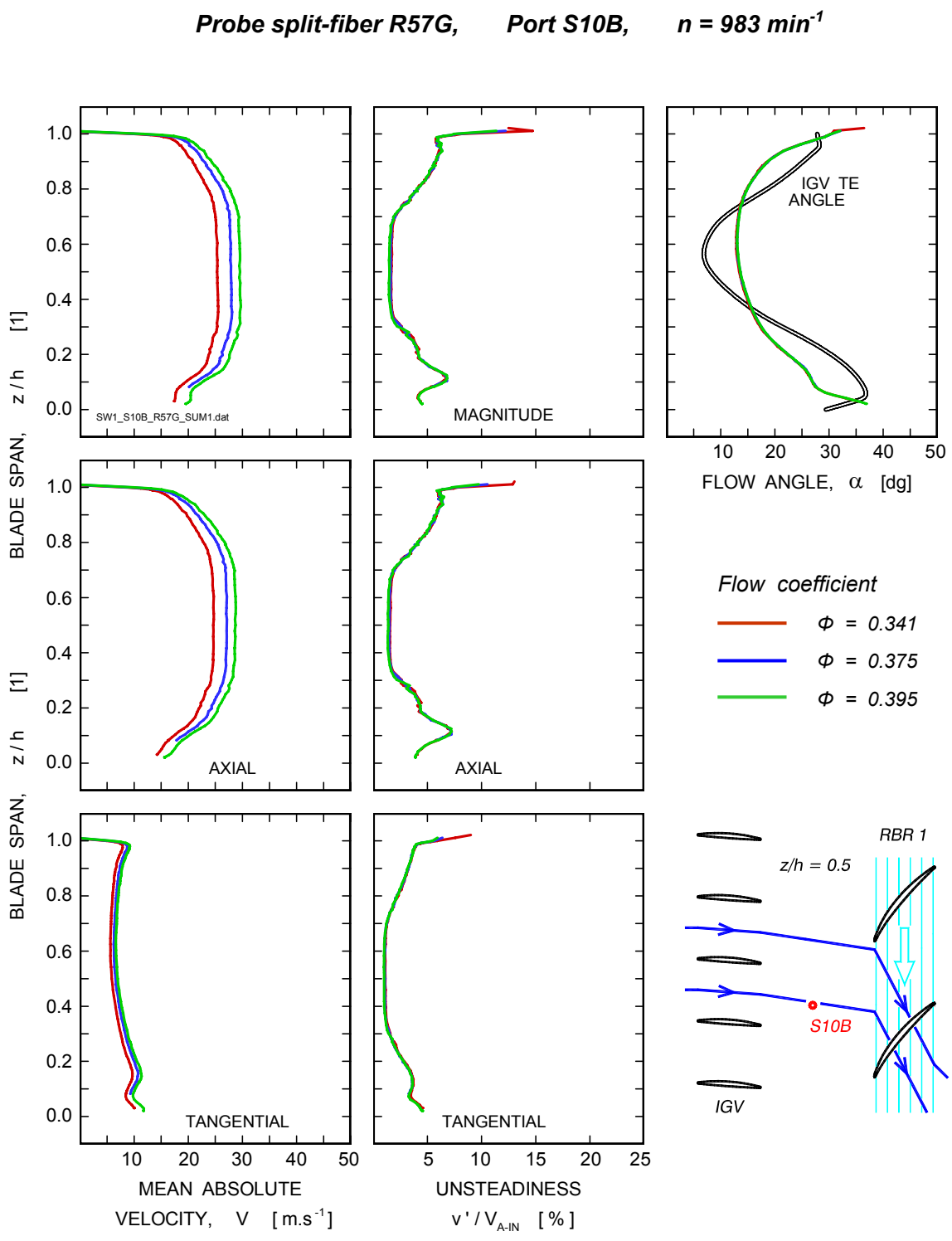


**Fig. 3-8. Comparison of radial distributions of flow parameters along the blade passage span behind the IGV row at station *S10B* for three operation conditions.**

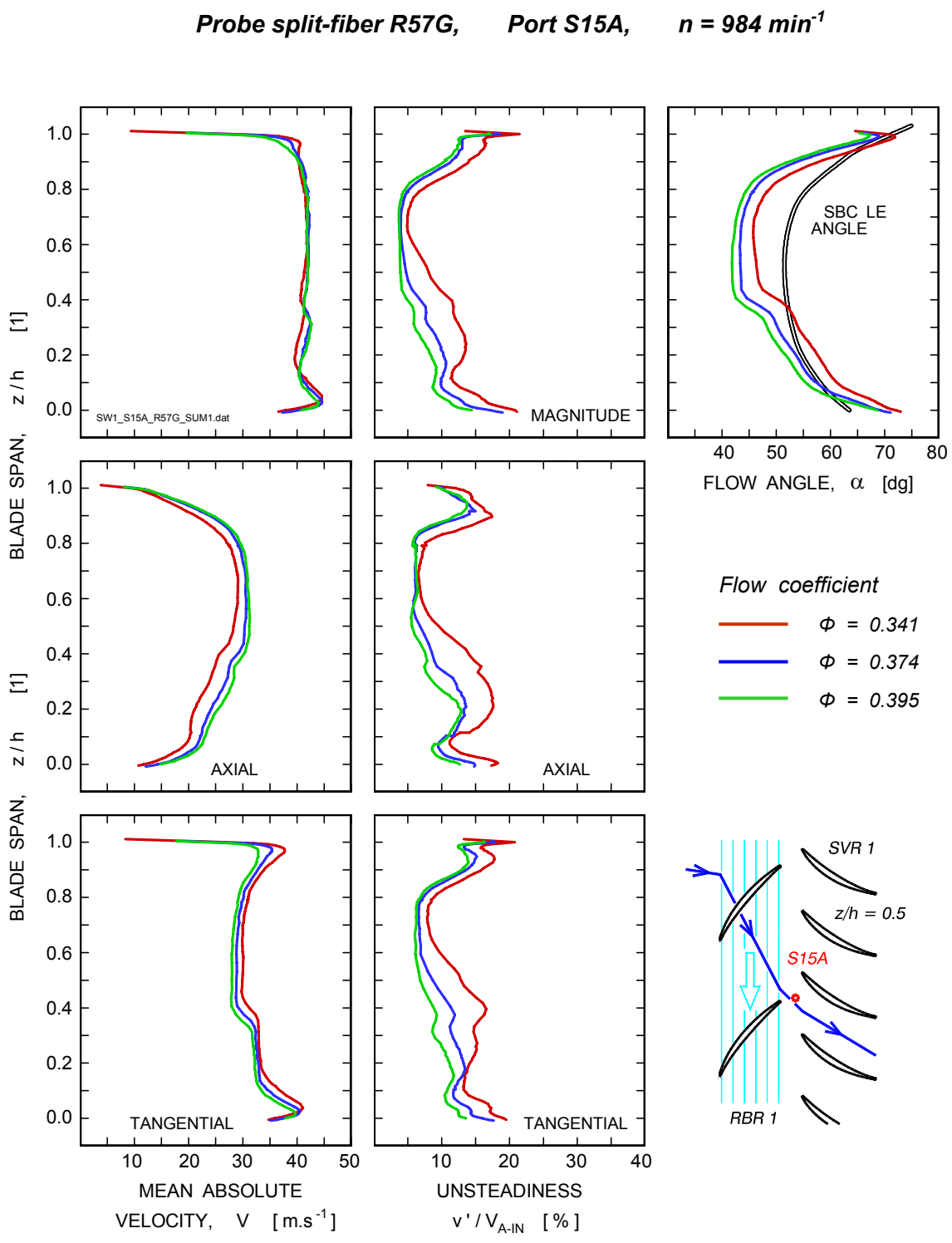


**Fig. 3-9. Comparison of radial distributions of flow parameters along the blade passage span in front of the first stator row at station *S15A* fort three operation conditions.**

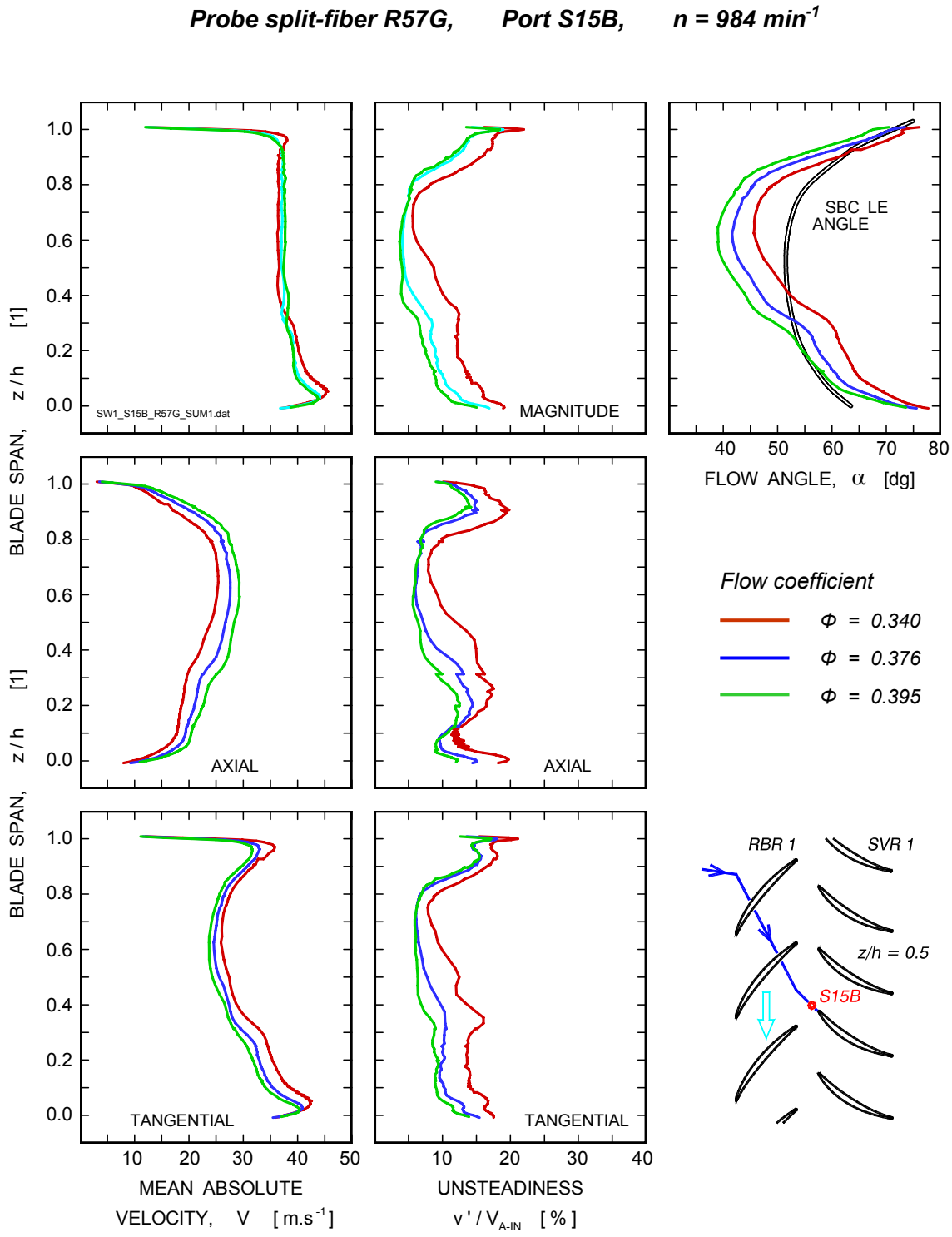


**Fig. 3-10. Comparison of radial distributions of flow parameters along the blade passage span in front of the first stator row at station *S15B* fort three operation conditions.**

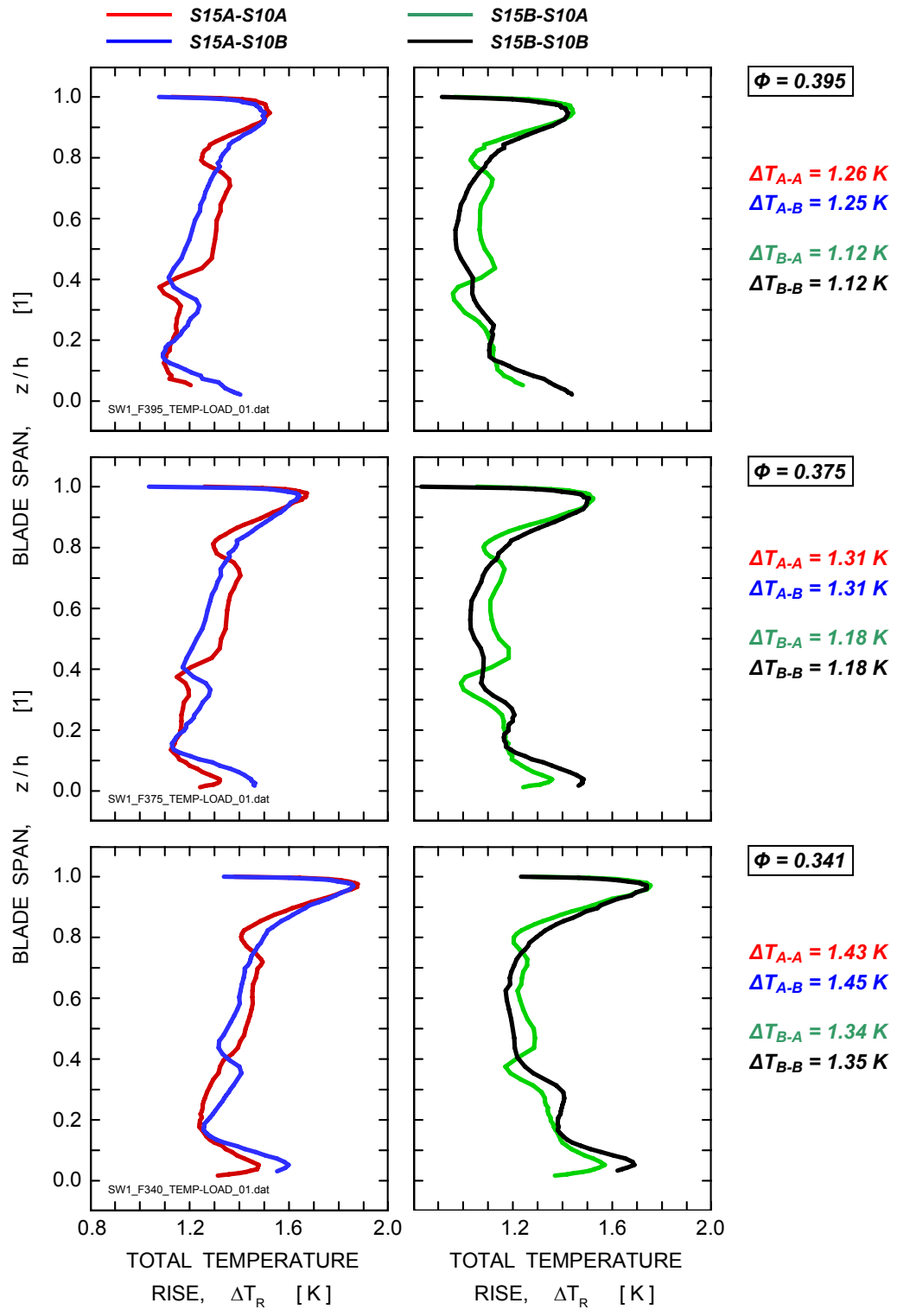


**Fig. 3-11. Spanwise distributions of the total temperature rise across the first stage rotor.**

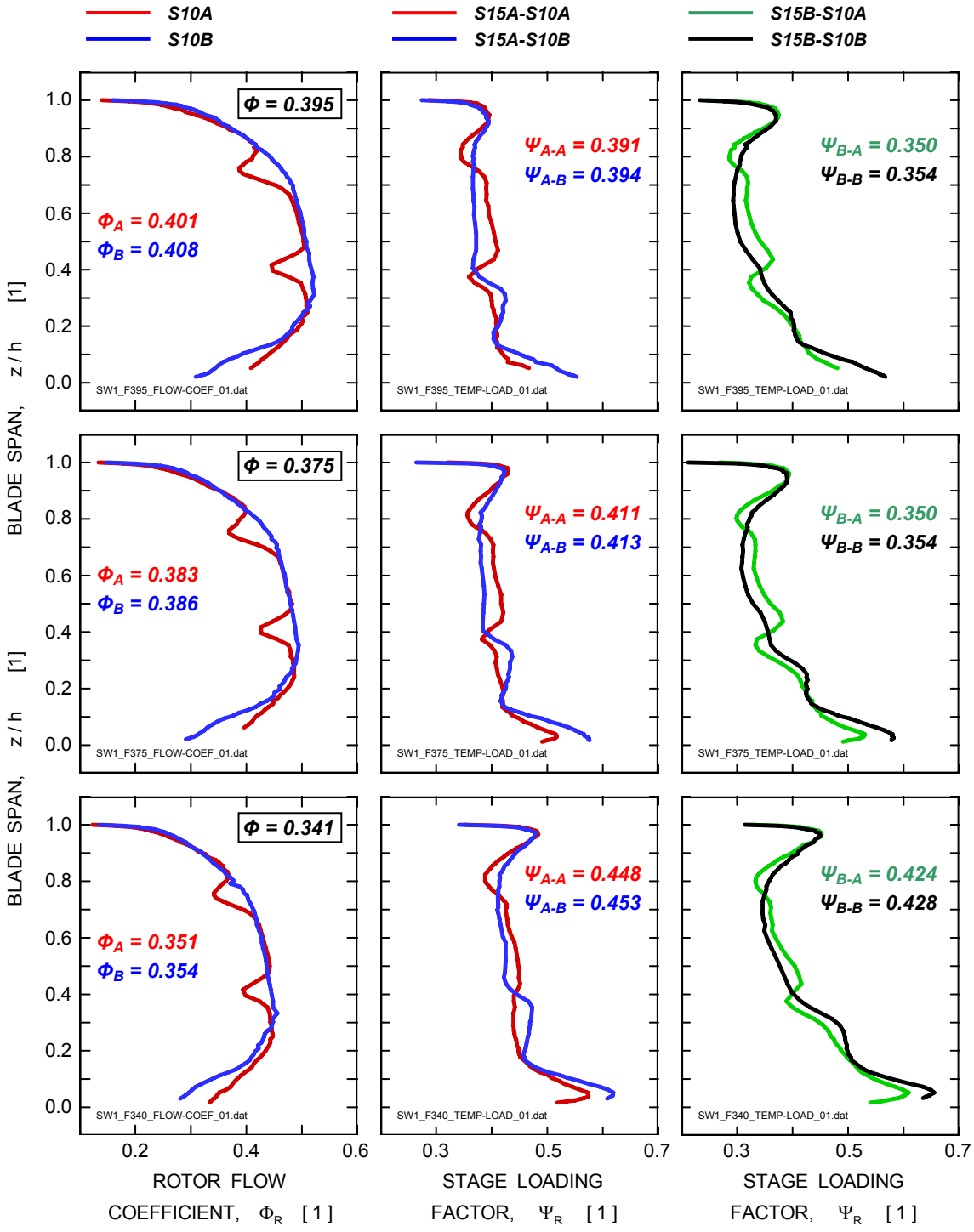


**Fig. 3-12. Rotor inlet flow coefficient ($\Phi_R$) and stage loading factor ($\Psi_R$) distributions along the rotor blade span.**

# 4.0 Blade Passage Ensemble Averages

Variations of flow parameters across a rotor blade passage can be retrieved from time histories using an ensemble averaging technique. In order to perform ensemble averaging, timing information about rotor and blade angular positions with respect to the probe position must be available.

## 4.1 Timing Signals

Two signals to determine rotor timing were acquired: once-per-revolution (OPR) and once-per-blade (OPB) signals. The OPR signal was derived from a standard optical pickup that is used to count rotor revolutions. The sensor is placed in the compressor frame perpendicular to the rotor disc, close to the disc circumference, facing a black mark on the disc. A relation of the rotor mark to the position of rotor blades can be seen in photograph in Fig. 4-1. The other signal, the OPB signal, was generated by an optical proximity probe mounted on the compressor shroud at the mid chord plane of the first rotor blades. Signals of both OPR and OPB probes are shown in Fig. 4-2.

The OPR signal exhibits constant amplitude spikes generated while rotor mark passes by the pickup. The OPB signal, on the other hand, exhibits strong variations in the amplitude of spikes generated as the blades are passing by the optical proximity probe. First, on the scale of one rotor revolution, it appears that the amplitude of spikes varies in a sine wave fashion. This may indicate a small eccentricity in the rotor motion or a pattern in arrangement of rotor blades according to their heights. On the smaller scale, blade-to-blade variations show big differences in the spike amplitude. Differences in blade heights will contribute to these variations, however, most likely, these variations are due to differences in the reflectivity of the blade tips (the OPB signal basically measures intensity of the light reflected from blade tips). As seen in Fig. 4-1, most of the blades are made from fiberglass. However, there are two aluminum blades on the rotor, and as might be expected, these two blades generate two strongest OPB signals.

The OPR and OPB signals, and for that matter all unsteady signals acquired, are mutually synchronized via an A/D board clock. The A/D board used does not have a provision for sample-and-hold data acquisition, and therefore they are time shifted by $0.8\ \mu s$ with respect to each other. We did not correct for this time shift because it is negligible with respect to the blade passage time of $1.57\ ms$ and is even more negligible relative the rotor revolution time of $61.04\ ms$. The A/D board timing is discussed in Ref. 4-1.

Since the onset of data acquisition was not triggered by the rotor motion, the starting point of time histories was arbitrary with respect to the rotor angular position. Therefore the beginning of all data was set during post processing to the center of the first full time interval of the OPR mark in the OPR data. In this way, velocity signals acquired for all test conditions are uniquely associated with individual rotor blades (Fig. 4-3).

## 4.2 Ensemble Averaging

Ensemble averaging enhances components of an unsteady signal associated with frequencies that are integer multiples of the frequency that is selected as a base for averaging (blade passing frequency in this particular case). Random signals and periodic signals at other frequencies are suppressed (averaged out). Therefore, the distribution of ensemble averages along the rotor blade passage, for unsteady velocity data, yields a blade-to-blade velocity distribution. A standard deviation of each ensemble averaged data point along the blade pitch can also be calculated (Ref. 4-2), which then yields a blade-to-blade velocity unsteadiness distribution (Ref. 2-1). Provided that there are no other periodic components in the original signal except those that are associated with blade passing frequency and its harmonics then averaging the unsteadiness distribution over a blade pitch results in a value which represents random (turbulent) flow fluctuations. In other words this is the velocity turbulence average value that remains after contributions of all deterministic fluctuations associated with blade passing frequency were removed. The unsteadiness distributions presented in 'Averaged radial distributions' (Section 3.0) were for overall unsteadiness levels, which contained deterministic fluctuations associated with blade passing frequency as well as the flow turbulence.

### 4.3 Blade Ensemble Averages of Flow Parameters

Results of blade passage ensemble averaging for axial and tangential velocity components and for absolute flow angle and velocity magnitude are shown in Figs. 4-4 through 4-7, respectively. These distributions are based on split-fiber probe measurements at a station *S15A* at the mid pitch position upstream of the first stator. The compressor was operated at a rotational speed of *983* $min^{-1}$ and a flow coefficient of *0.340*, which is at the last stable point before the onset of rotating stall. To improve the readability of data in the wake region each diagram depicts a same blade-to-blade distribution plotted twice next to each other. The ensemble averages were generated from data segments that were *5 s* in duration, therefore every blade-to-blade distribution represents an average of at least *3100* rotor blade passages.

Blade-to-blade distributions of velocity or flow angle are presented in the left hand columns of diagrams in Figs. 4-4 through 4-7 for selected blade height positions. The average velocity or angle values, for each distribution presented, are stated at each diagram. These average values are identical to the overall average values presented in Figs. 3-4 and 3-9. The blade-to-blade distributions of velocity or directional unsteadiness are presented in the right-hand column in Figs. 4-4 through 4-7. The distributions clearly illustrate significantly different unsteady flow behavior in the blade tip and hub regions.

### 4.4 Blade Channel Average Contour Maps

Individual diagrams with blade-to-blade distributions helped to determine probe performance. It is difficult and impractical, however, to gain an insight into the overall flow behavior using the individual distribution diagrams. Therefore, the blade-to-blade distributions were used to create contour maps for individual flow parameters at two measurement stations behind the first stage rotor (*S15A* and *S15B*) and for various flow coefficients. The contour plots for flow parameters and unsteadiness for operation conditions characterized by flow coefficients of *0.395*, *0.375*, and *0.340* are presented for both measurement stations in Figs. 4-8 through 4-25. Similarly as with the blade-to-blade single signal distributions, also shown here are two identical blade-channel contour maps plotted next to each other to improve the readability of the rotor blade wake region. Broken lines in these plots the indicate location of the rotor blade trailing edge. Contour scales for velocity components and velocity unsteadiness are normalized by the inlet velocity $V_{IN}$. The difference between positions for stations *S15A* and *S15B* reflects the difference in relative positions of measurement stations and stator vanes.

It can be seen in the first series of figures, which is for the axial velocity component (Figs. 4-8 through 4-13), that as the flow coefficient decreases the width of the rotor blade wake increases, and in particular there is a significant increase of the extent of the region of low axial velocity (i.e., aerodynamic blockage) as well as high velocity unsteadiness at the blade root on the blade suction side. The same is true for the blade tip region where there is a dramatic increase of the size of the region with increased axial velocity unsteadiness in the rotor blade pressure side flow. On comparing experimental results for the mid pitch measurement station (*S15A*) and the stagnation region measurement station (*S15B*), the flow pattern is basically similar, however the mid pitch region exhibits higher velocity levels then the levels measured by a probe traversing in the stator vane stagnation region.

The second series of figures (Figs. 4-14 through 4-19) presents the results for the tangential velocity component. This component increases with decreasing values of the flow coefficient, in particular in the blade hub region and in the rotor wake. The tangential velocity unsteadiness also increases with a falling flow coefficient; however, the increase is noticeable mainly in the blade tip region, and nearly insignificant close to the hub.

Contour maps for absolute flow angle and flow angle (directional) unsteadiness are presented in the third series of figures (Figs. 4-20 through 4-25). In general, the absolute flow angle increases with decreasing compressor flow coefficient. The directional unsteadiness increases as well. However, it appears that the increase in directional unsteadiness is more pronounced for measurements in the stator vane stagnation region (station *S15B*). This is true in particular for the low flow coefficient of *0.340* where the directional unsteadiness is quite high in the entire blade tip region and on the suction side at the blade root. For the high flow coefficient of *0.395* a difference in flow unsteadiness between stations *S15A* and *S15B* is barely traceable.

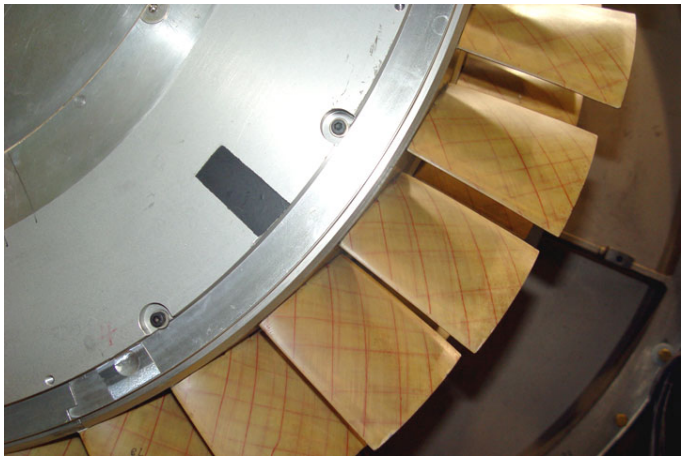

**Fig. 4-1. OPR marker on the first rotor disc.**

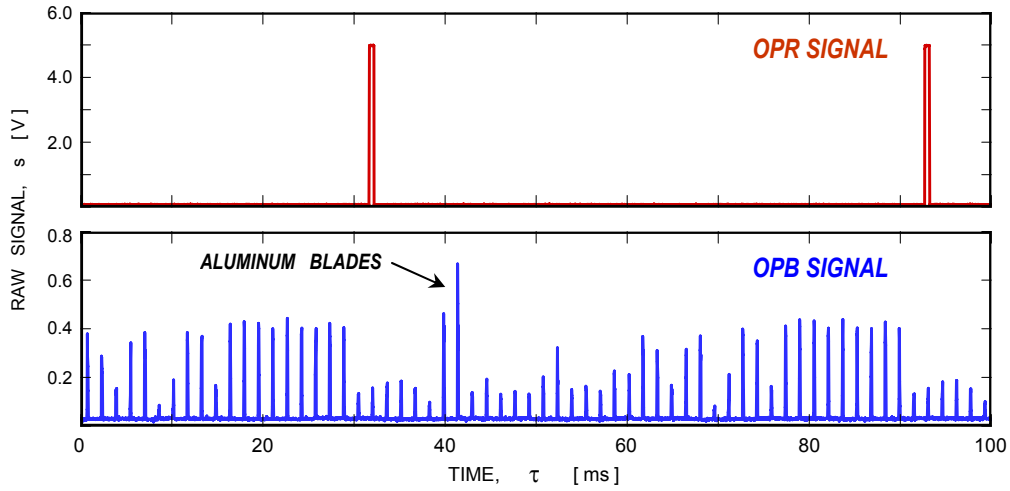


**Fig. 4-2. Random onset of OPR and OPB signals**

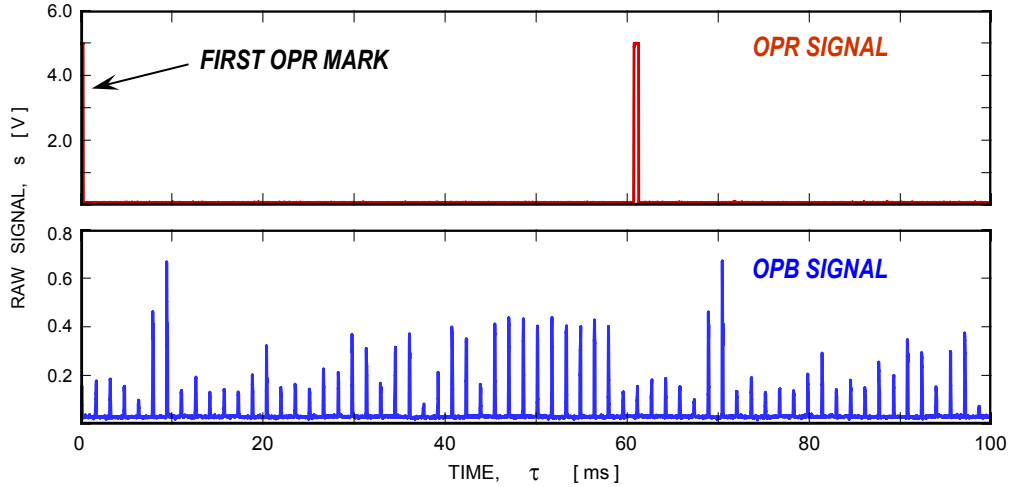


**Fig. 4-3. Onset of OPR and OPB signals for a fixed rotor angular position.**

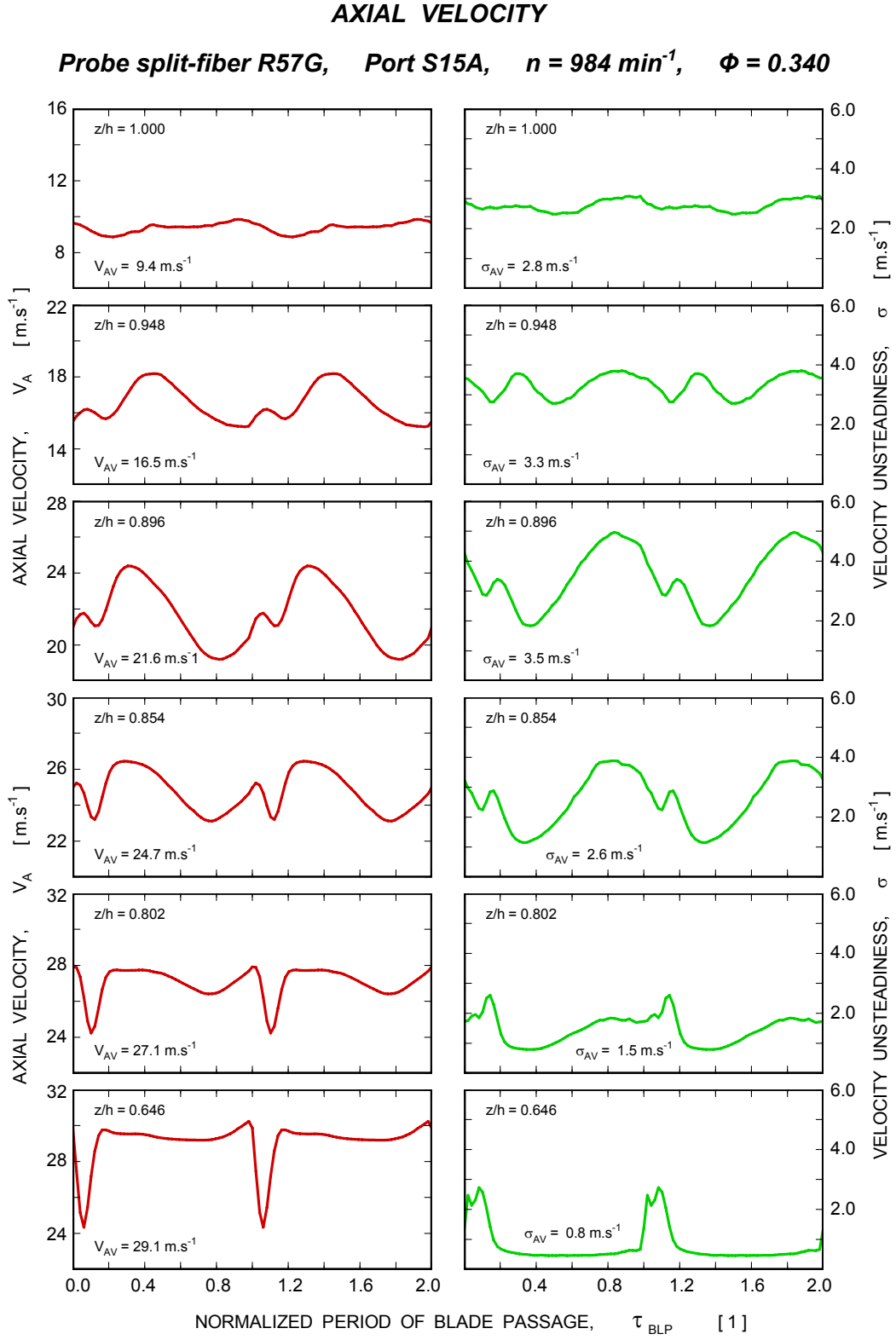


**Fig. 4-4a. Blade passage ensemble averages of axial velocity component at station *S15A* for flow coefficient of *0.340*.**

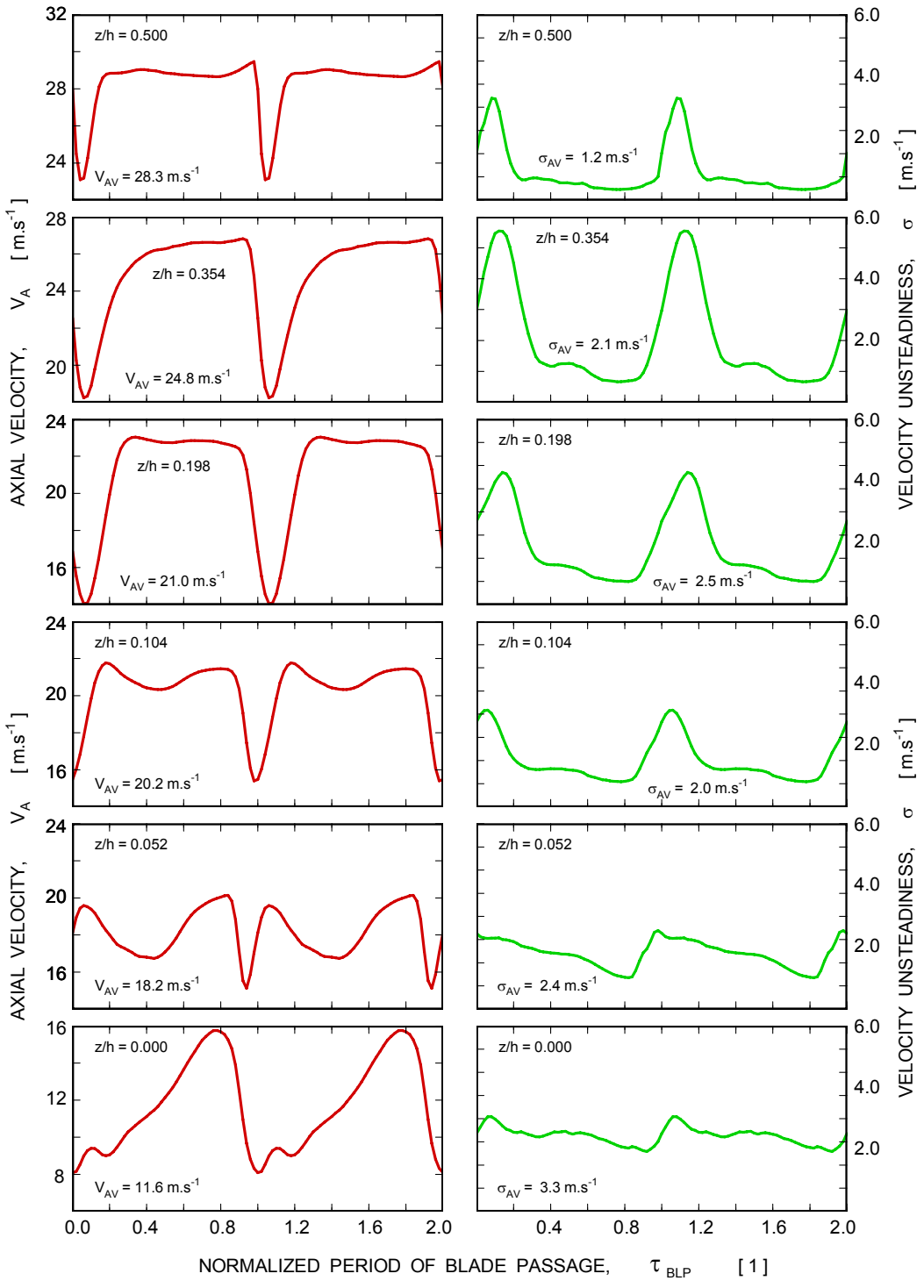


**Fig. 4-4b. Blade passage ensemble averages of axial velocity component at station *S15A* for flow coefficient of *0.340*.**

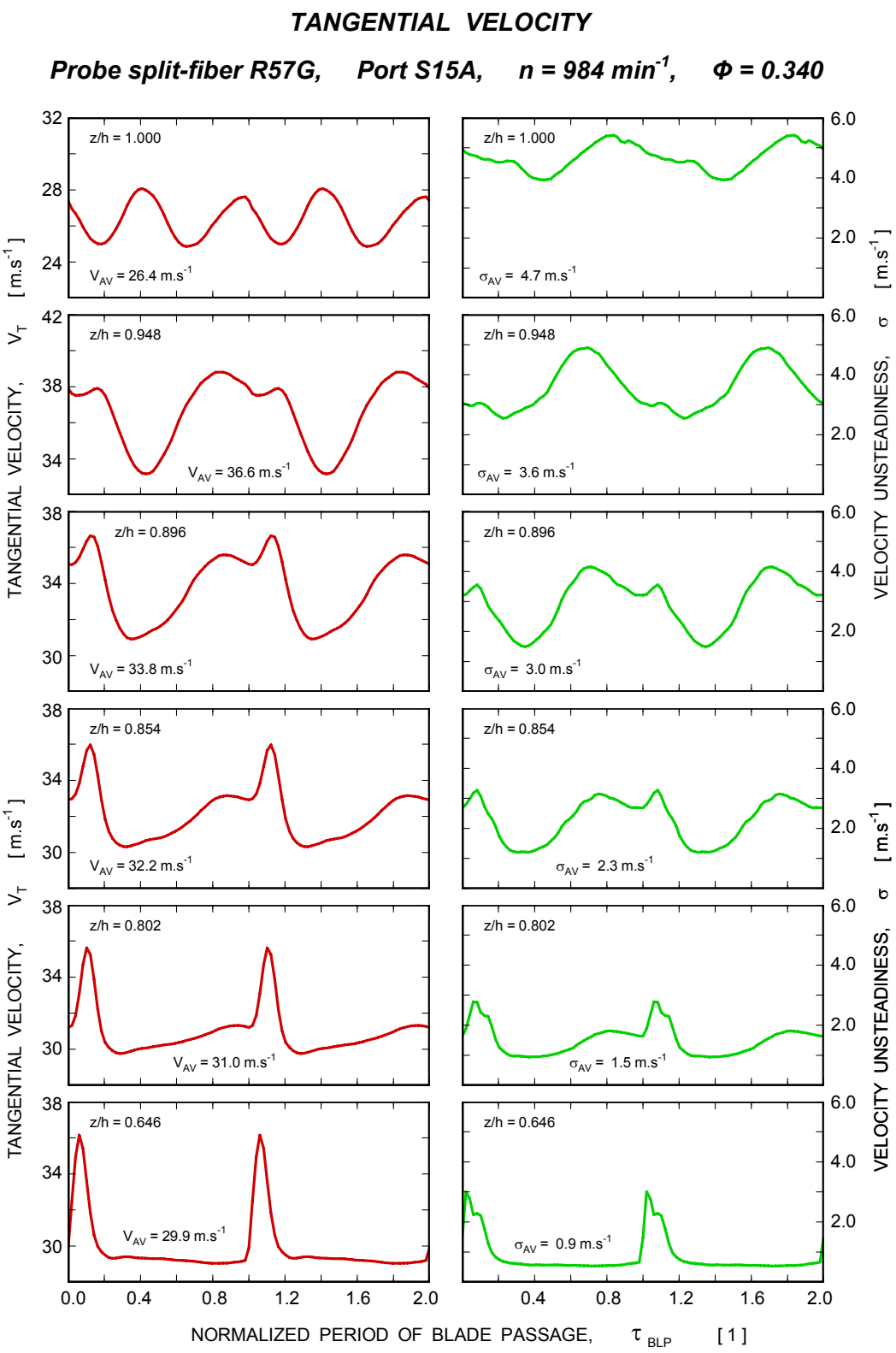


**Fig. 4-5a. Blade passage ensemble averages of tangential velocity component at station *S15A* for flow coefficient of *0.340*.**

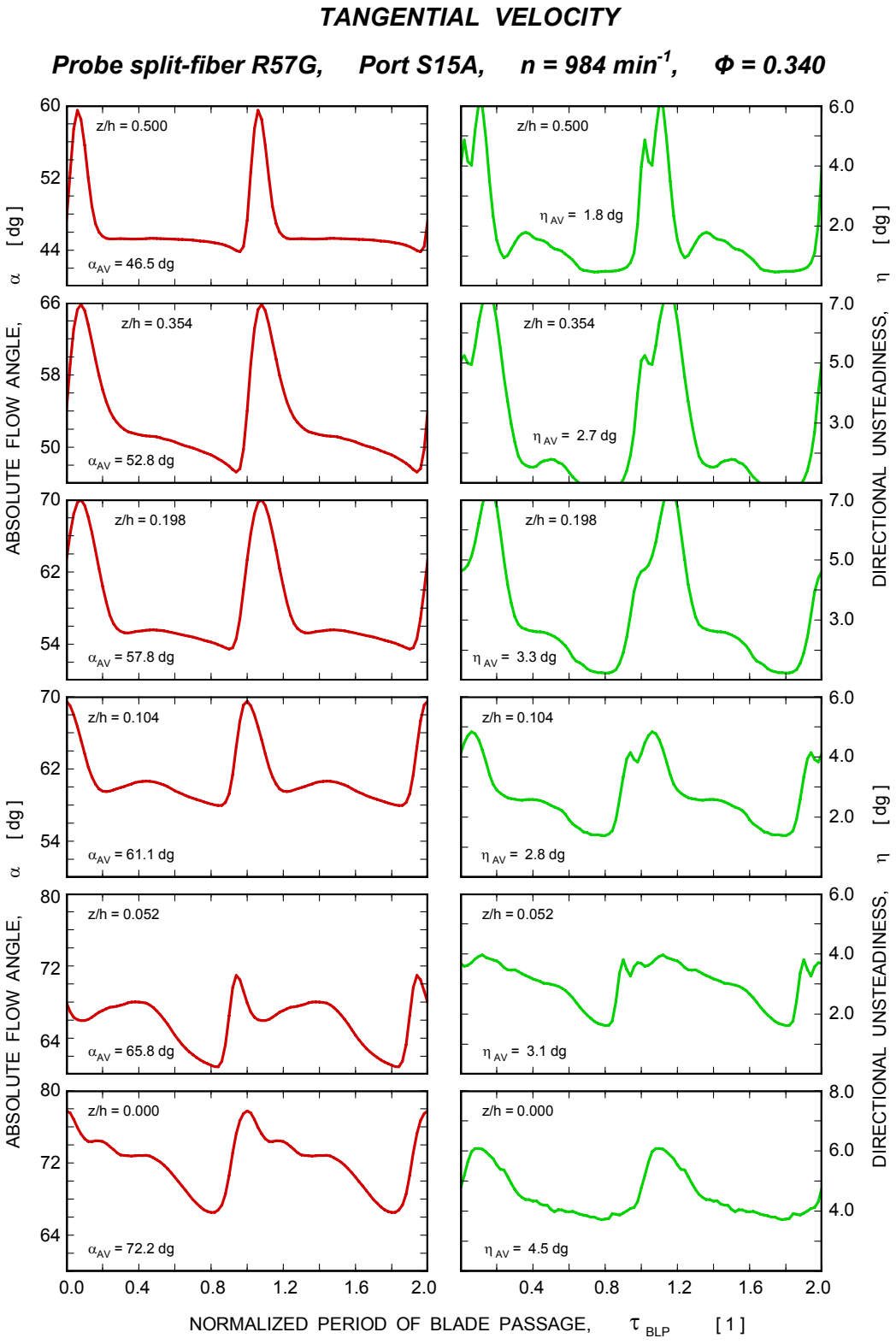


**Fig. 4-5b. Blade passage ensemble averages of tangential velocity component at station *S15A* for flow coefficient of *0.340*.**

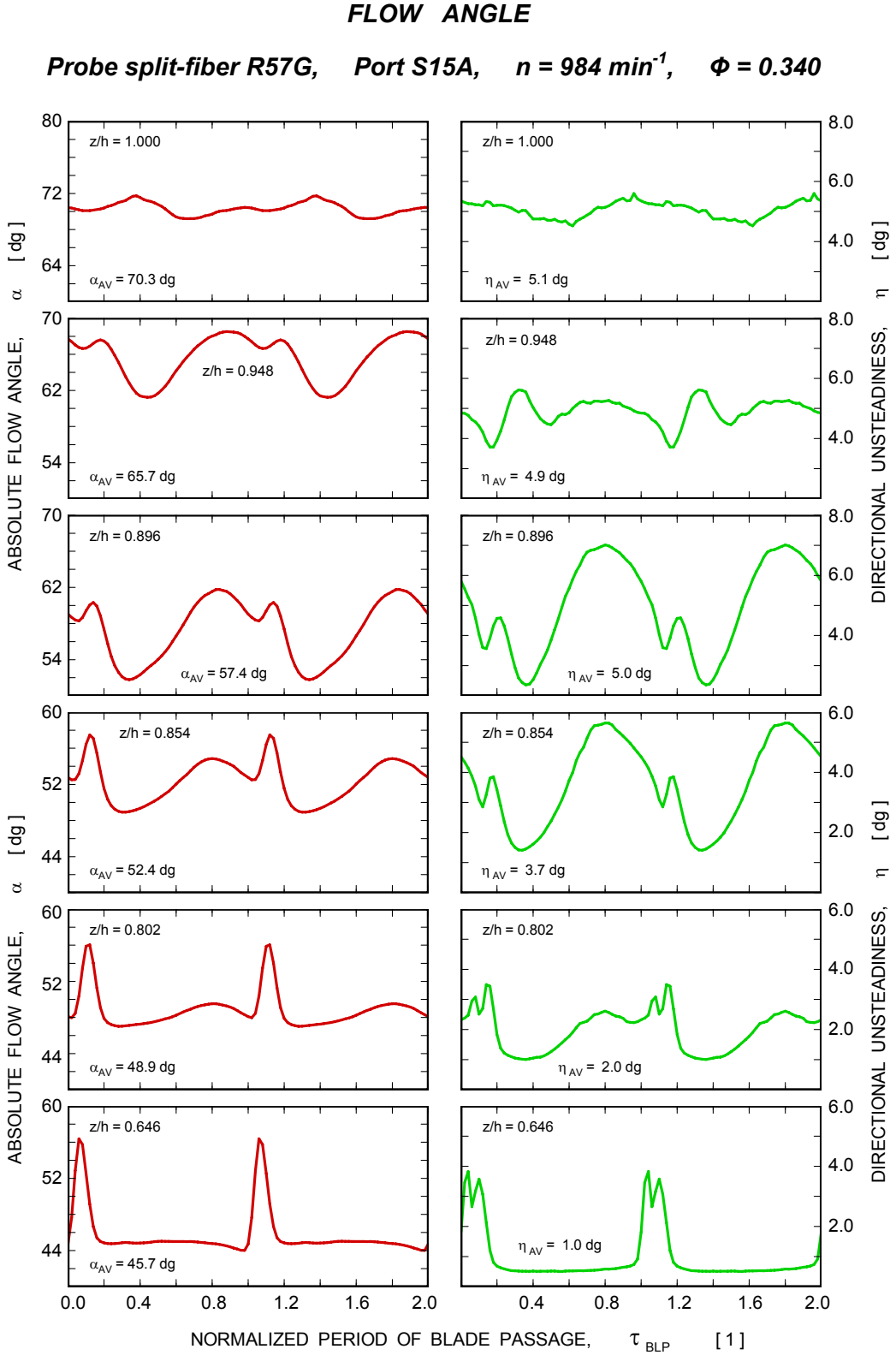


**Fig. 4-6a. Blade passage ensemble averages of absolute flow angle at station *S15A* for flow coefficient of *0.340*.**

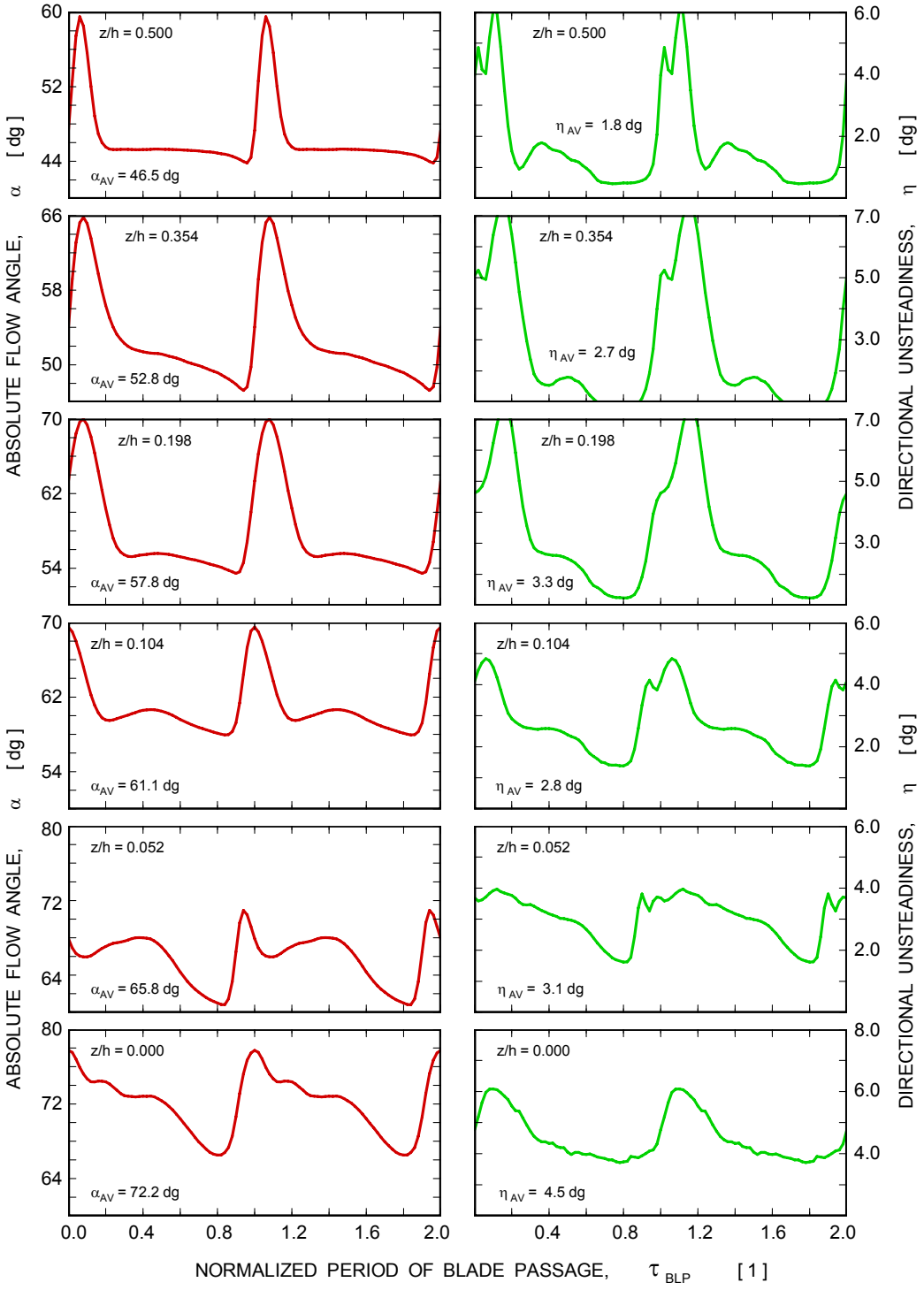


**Fig. 4-6b. Blade passage ensemble averages of absolute flow angle at station *S15A* for flow coefficient of *0.340*.**

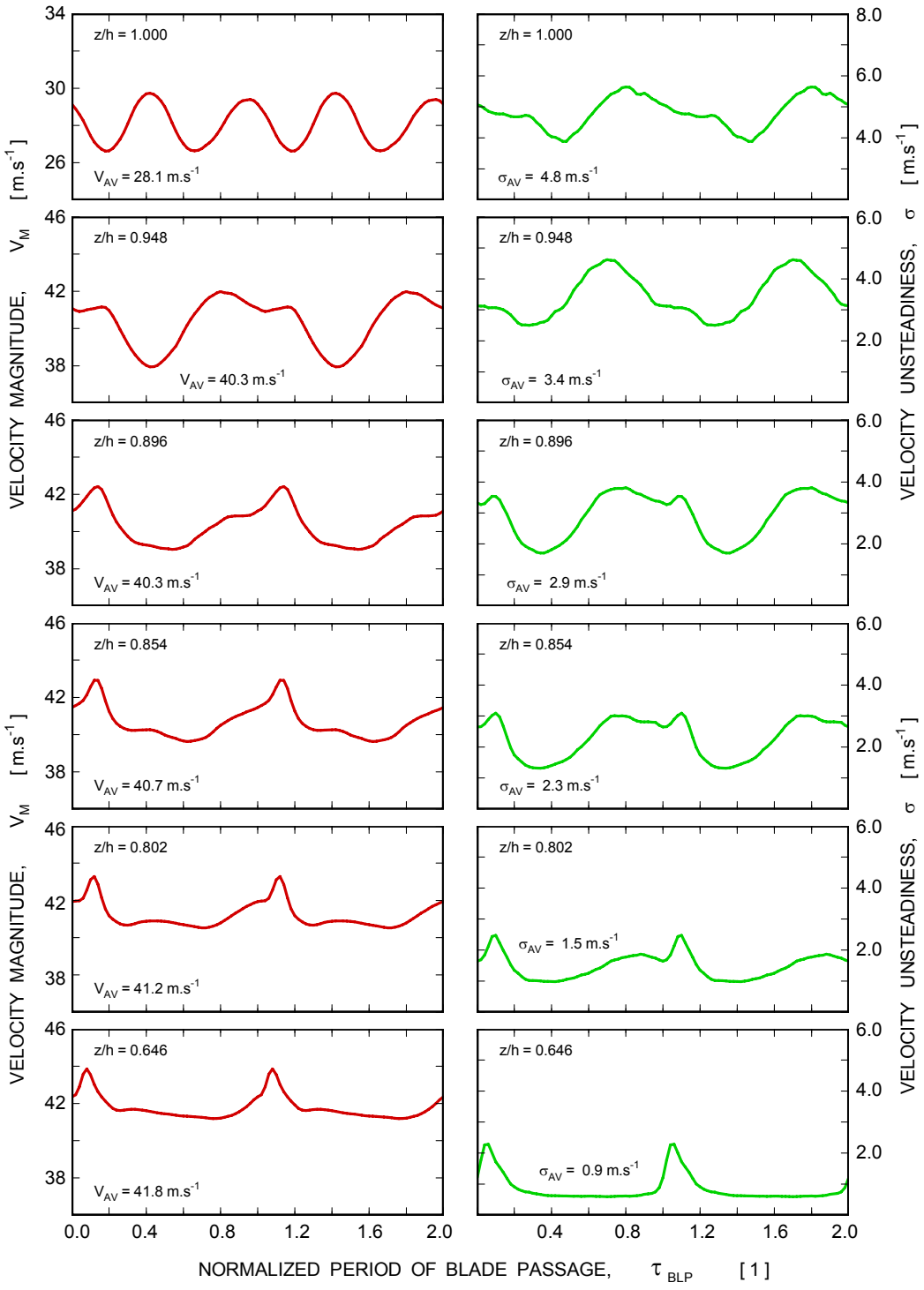


**Fig. 4-7a. Blade passage ensemble averages of velocity magnitude at station *S15A* for flow coefficient of *0.340*.**

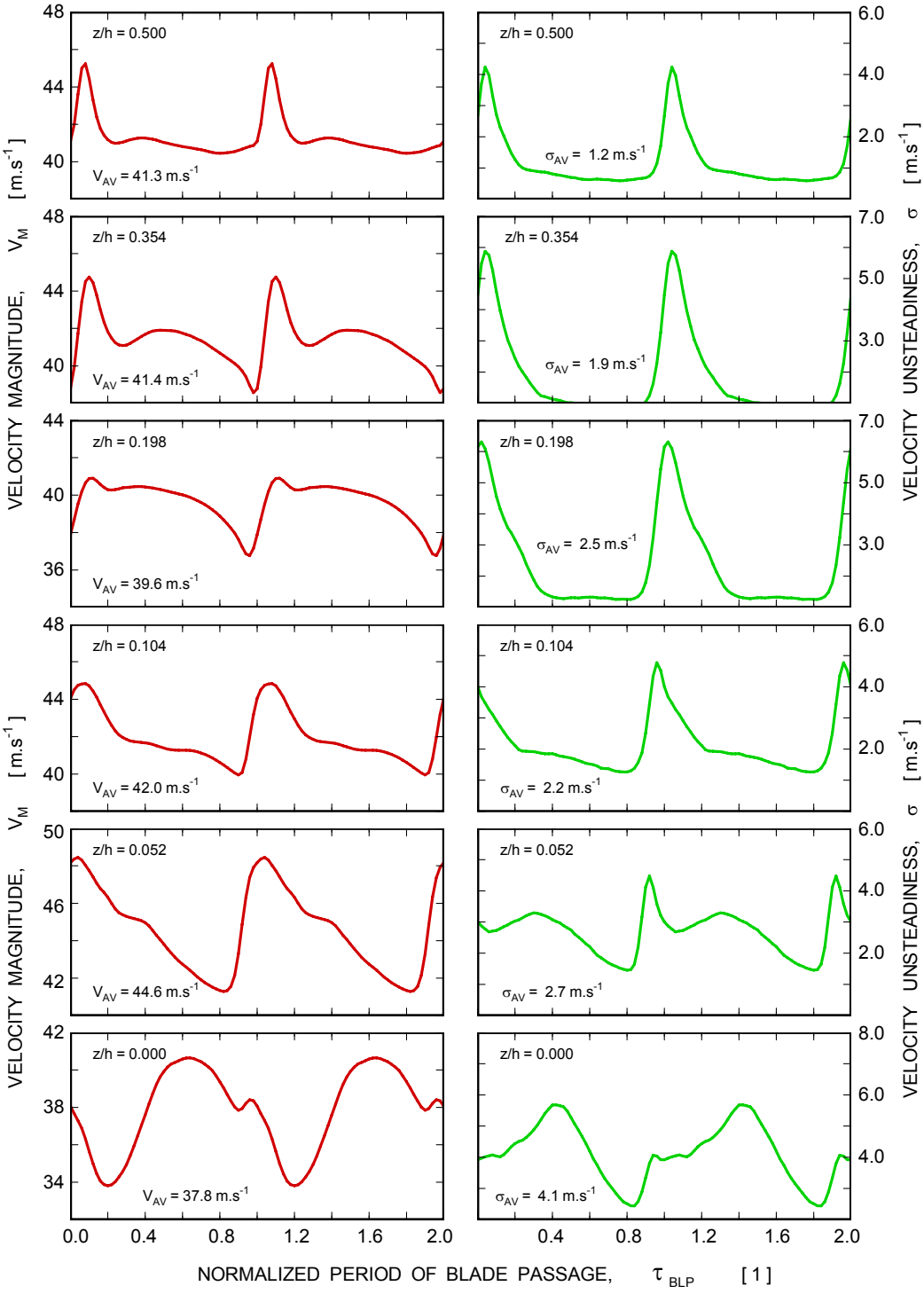


**Fig. 4-7b. Blade passage ensemble averages of velocity magnitude at station *S15A* for flow coefficient of *0.340*.**

***Probe split-fiber R57G, Port S15A, n = 984 min$^{-1}$, Φ = 0.395***

***NORMALIZED AXIAL VELOCITY LEVELS***

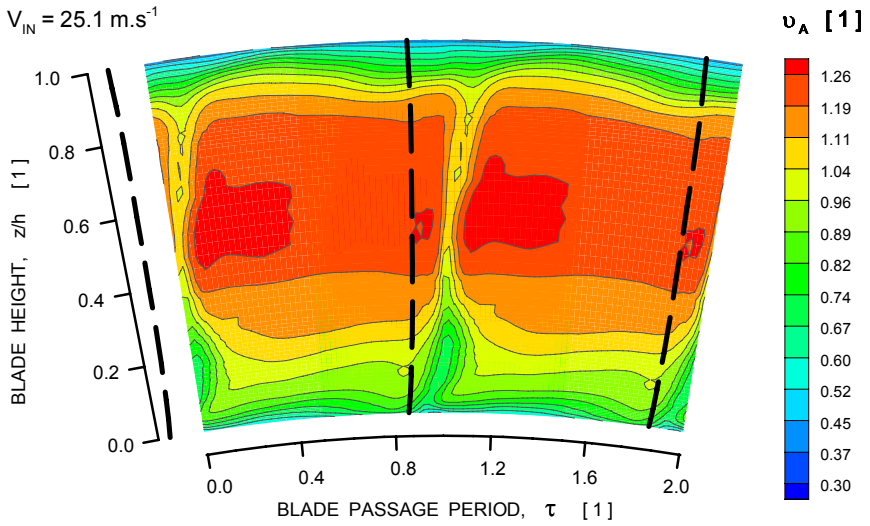


***RANDOM AXIAL VELOCITY UNSTEADINESS***

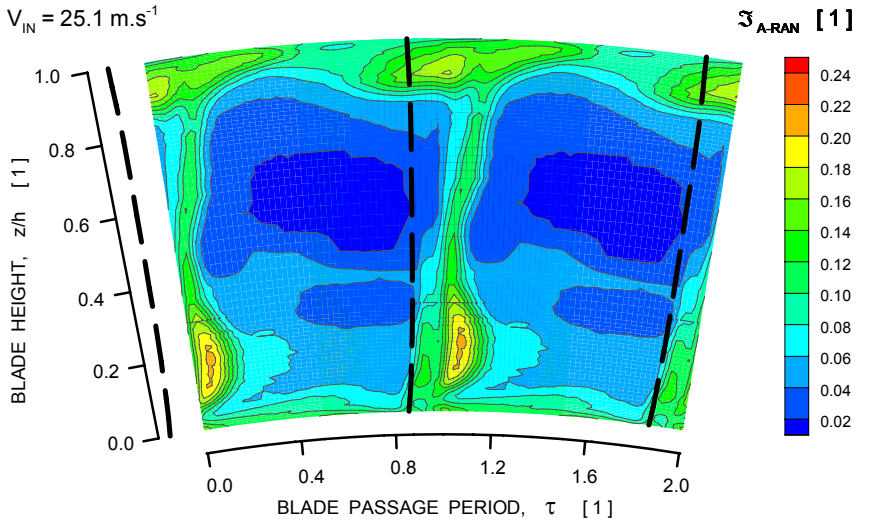


**Fig. 4-8. Contour maps of axial velocity for a rotor blade passage measured at station *S15A* for flow coefficient of *0.395*.**

***Probe split-fiber R57G, Port S15B, n = 983 min$^{-1}$, Φ = 0.395***

***NORMALIZED AXIAL VELOCITY LEVELS***

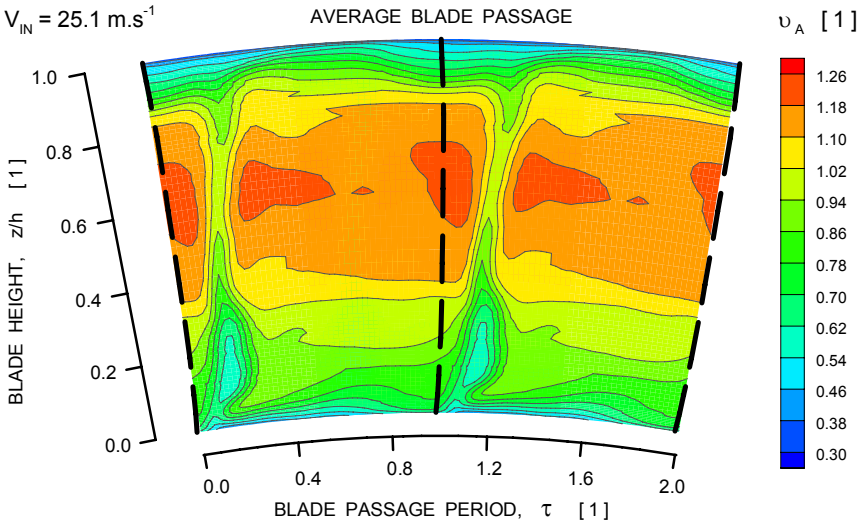


***RANDOM AXIAL VELOCITY UNSTEADINESS***

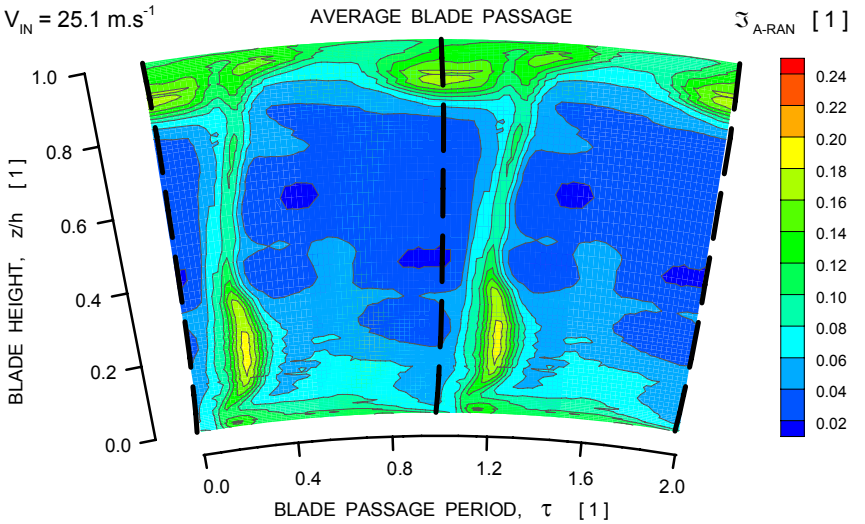


**Fig. 4-9. Contour maps of axial velocity for a rotor blade passage measured at station *S15B* for flow coefficient of *0.395*.**

***Probe split-fiber R57G, Port S15A, n = 984 min$^{-1}$, Φ = 0.374***

***NORMALIZED AXIAL VELOCITY LEVELS***

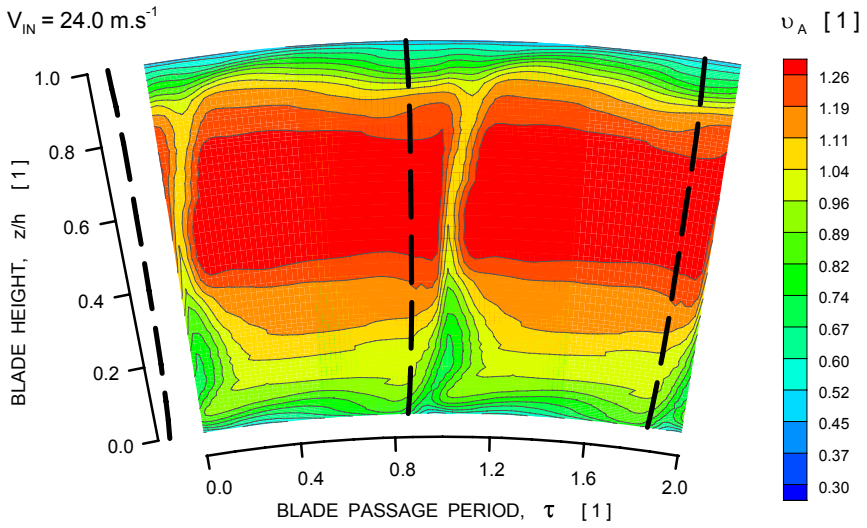


***RANDOM AXIAL VELOCITY UNSTEADINESS***

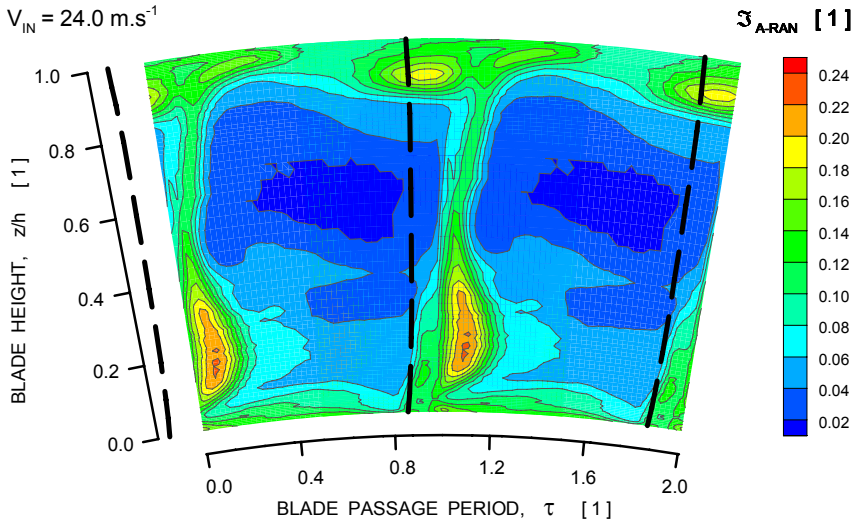


**Fig. 4-10. Contour maps of axial velocity for a rotor blade passage measured at station *S15A* for flow coefficient of *0.374*.**

***Probe split-fiber R57G, Port S15B, n = 983 min$^{-1}$, Φ = 0.376***

***NORMALIZED AXIAL VELOCITY LEVELS***

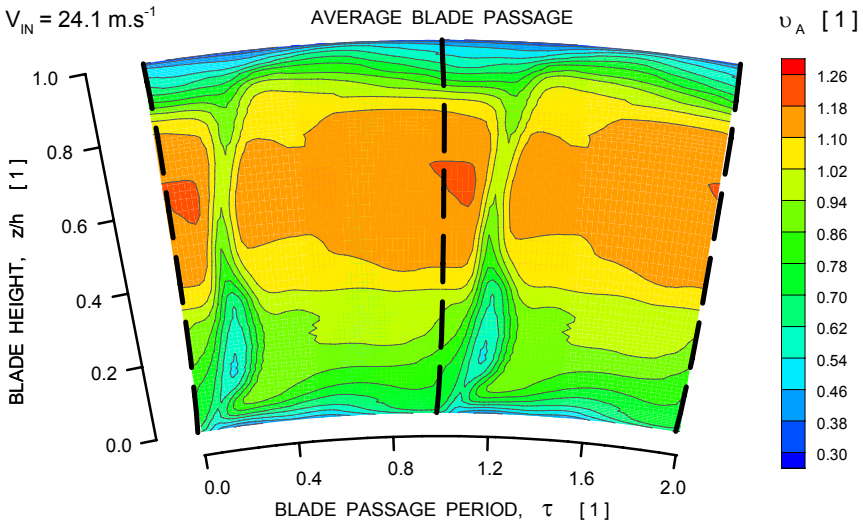


***RANDOM AXIAL VELOCITY UNSTEADINESS***

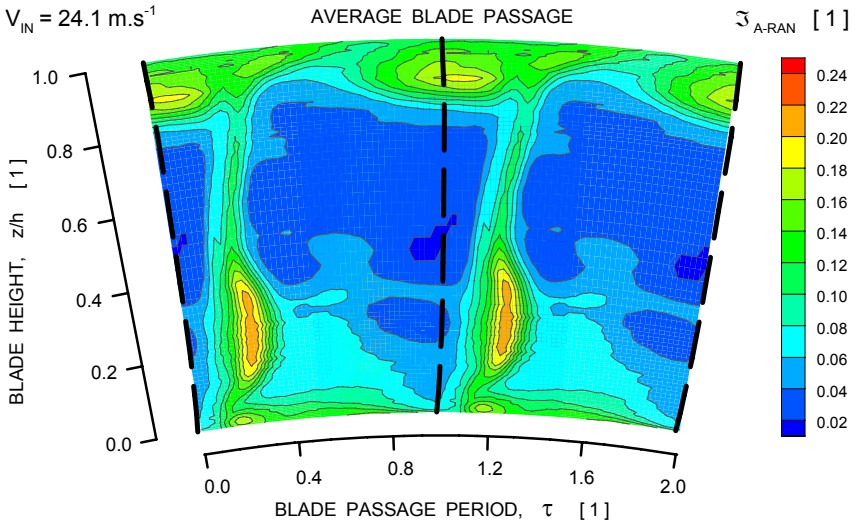


**Fig. 4-11. Contour maps of axial velocity for a rotor blade passage measured at station *S15B* for flow coefficient of *0.376*.**

***Probe split-fiber R57G, Port S15A, n = 983 min$^{-1}$, Φ = 0.341***

***NORMALIZED AXIAL VELOCITY LEVELS***

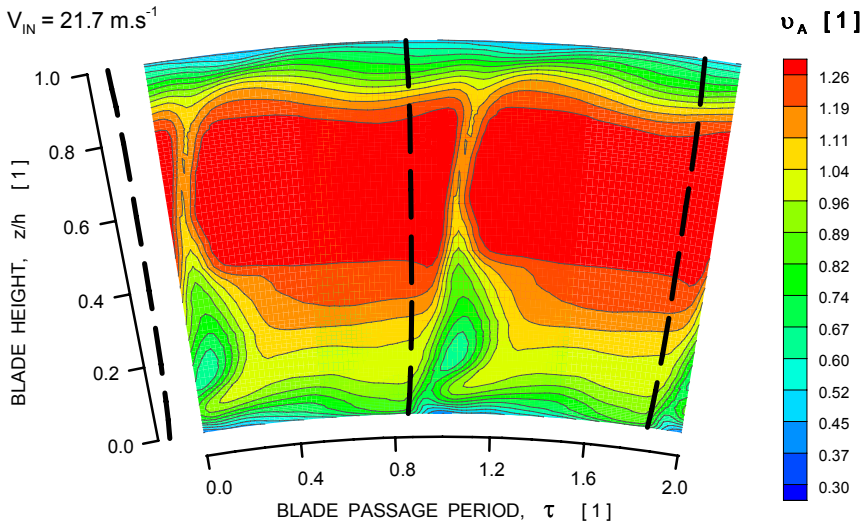


***RANDOM AXIAL VELOCITY UNSTEADINESS***

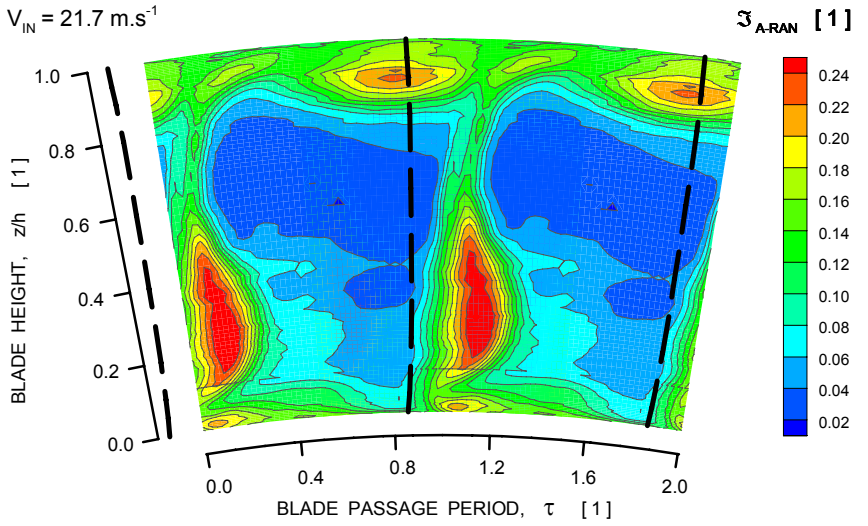


**Fig. 4-12. Contour maps of axial velocity for a rotor blade passage measured at station *S15A* for flow coefficient of *0.341*.**

***Probe split-fiber R57G, Port S15B, n = 983 min$^{-1}$, Φ = 0.340***

***NORMALIZED AXIAL VELOCITY LEVELS***

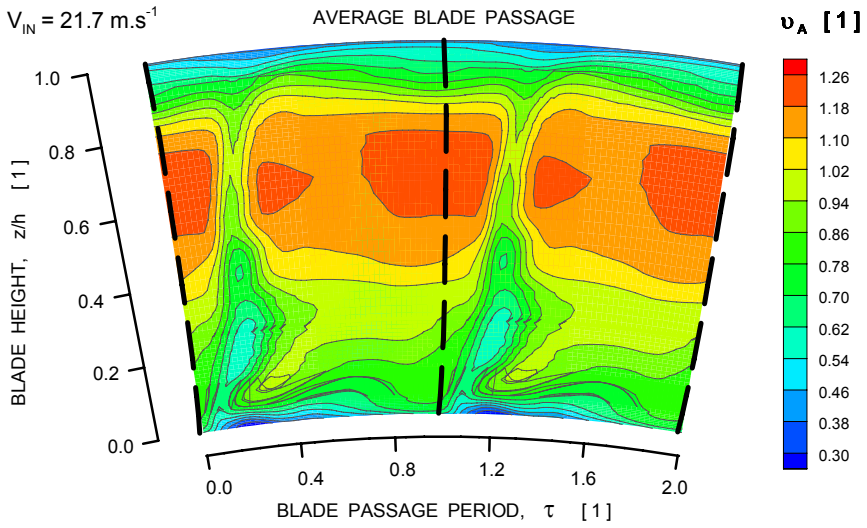


***RANDOM AXIAL VELOCITY UNSTEADINESS***

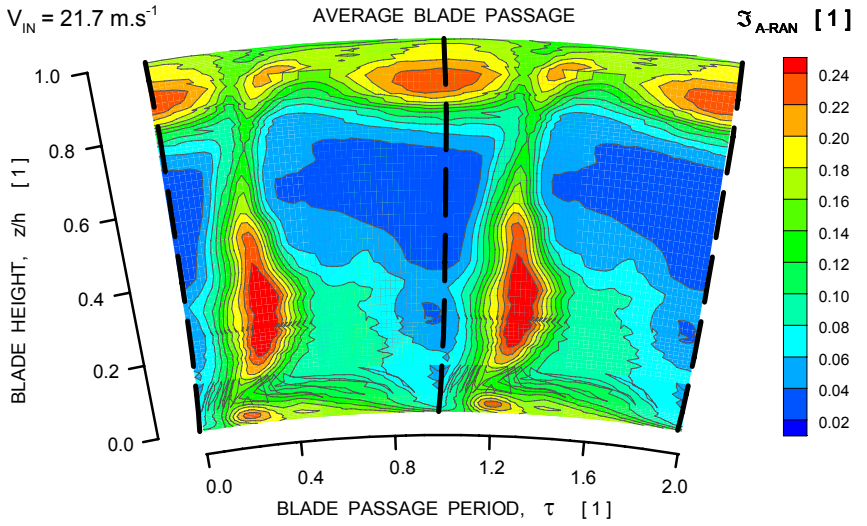


**Fig. 4-13. Contour maps of axial velocity for a rotor blade passage measured at station *S15B* for flow coefficient of *0.340*.**

***Probe split-fiber R57G, Port S15A, n = 983 min$^{-1}$, Φ = 0.395***

***NORMALIZED TANGENTIAL VELOCITY LEVELS***

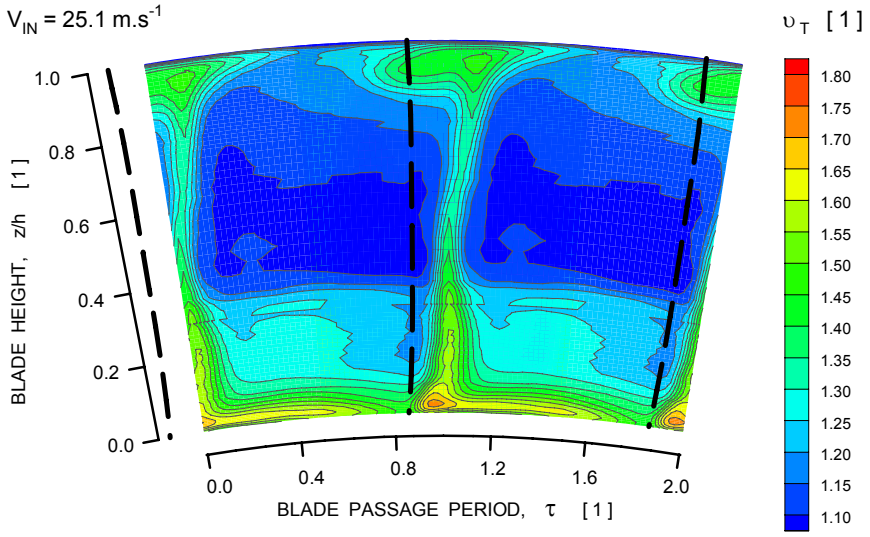


***RANDOM TANGENTIAL VELOCITY UNSTEADINESS***

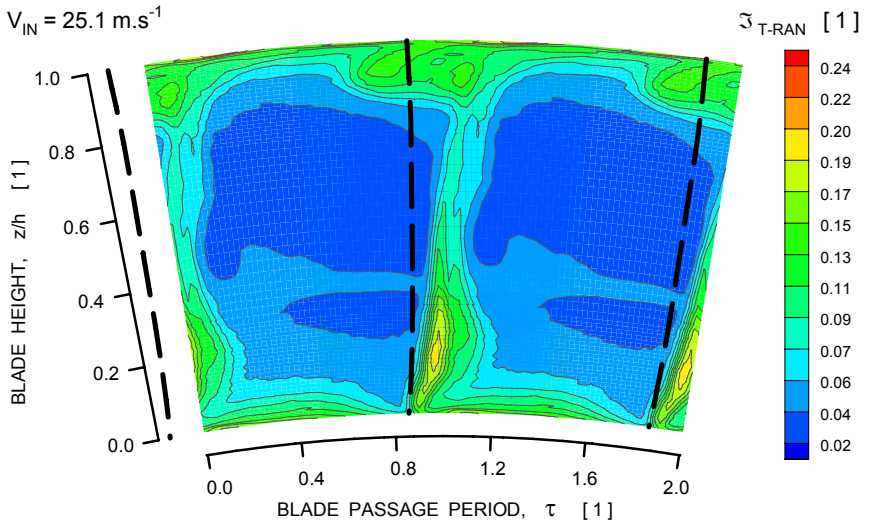


**Fig. 4-14. Contour maps of tangential velocity for a rotor blade passage measured at station *S15A* for flow coefficient of *0.395*.**

***Probe split-fiber R57G, Port S15B, n = 983 min$^{-1}$, Φ = 0.395***

***NORMALIZED TANGENTIAL VELOCITY LEVELS***

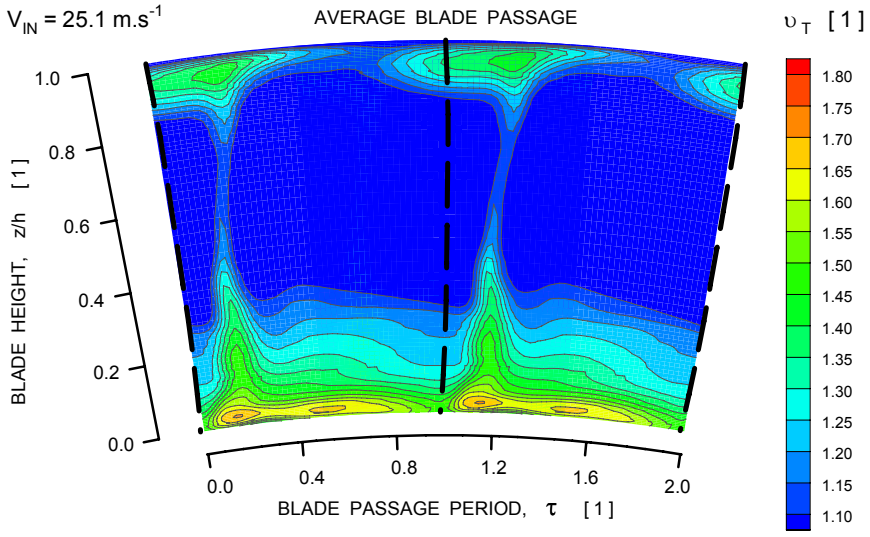


***RANDOM TANGENTIAL VELOCITY UNSTEADINESS***

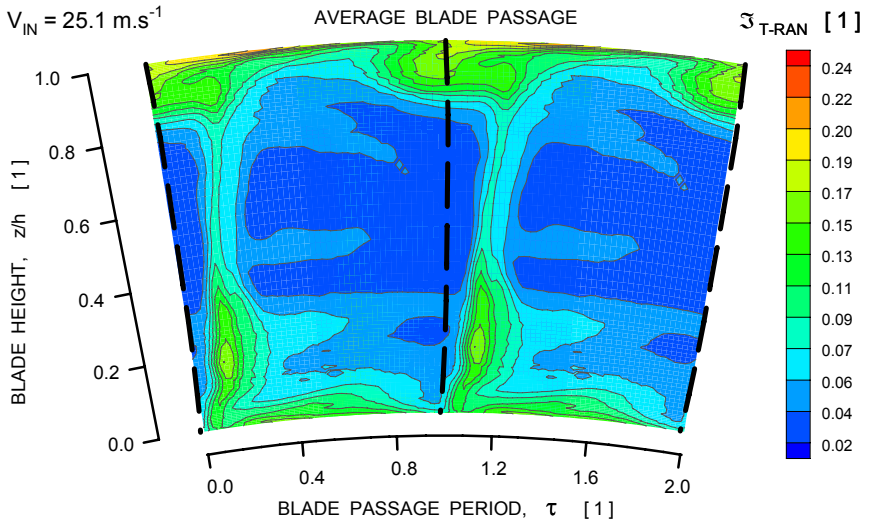


**Fig. 4-15. Contour maps of tangential velocity for a rotor blade passage measured at station *S15B* for flow coefficient of *0.395*.**

***Probe split-fiber R57G, Port S15A, n = 983 min$^{-1}$, Φ = 0.375***

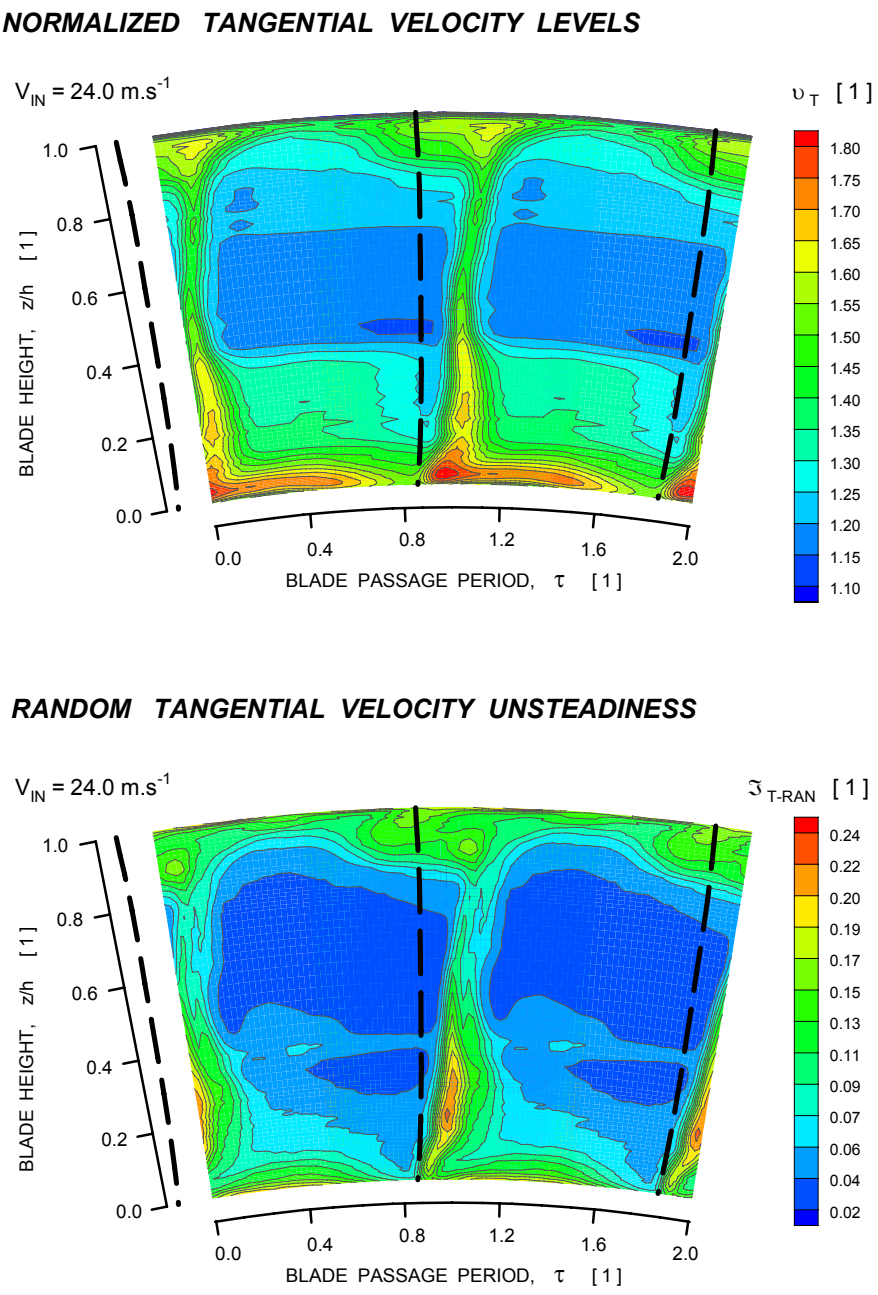


**Fig. 4-16. Contour maps of tangential velocity for a rotor blade passage measured at station *S15A* for flow coefficient of *0.375*.**

***Probe split-fiber R57G, Port S15B, n = 983 min$^{-1}$, Φ = 0.375***

***NORMALIZED TANGENTIAL VELOCITY LEVELS***

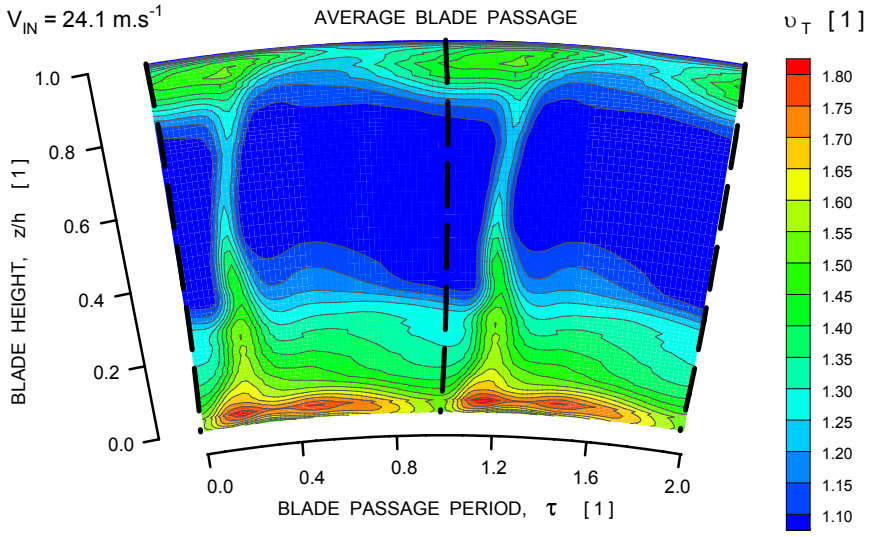


***RANDOM TANGENTIAL VELOCITY UNSTEADINESS***

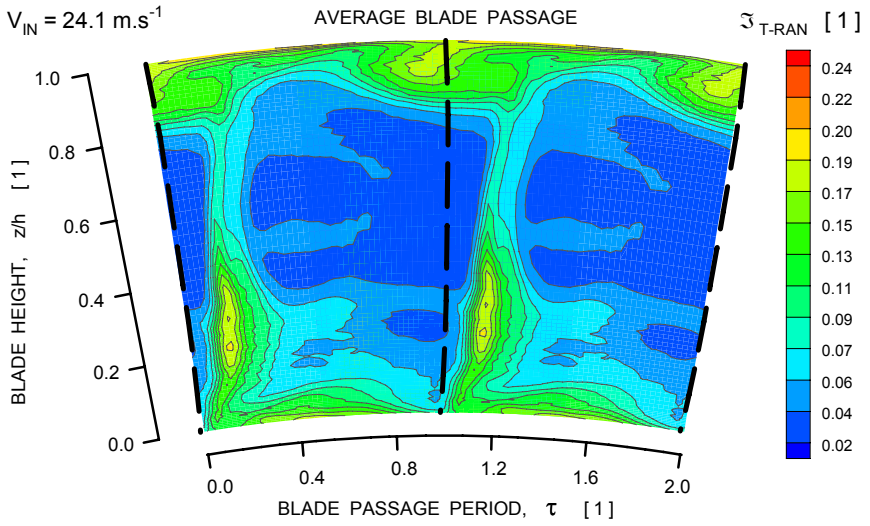


**Fig. 4-17. Contour maps of tangential velocity for a rotor blade passage measured at station *S15B* for flow coefficient of *0.375*.**

***Probe split-fiber R57G, Port S15A, n = 983 min$^{-1}$, Φ = 0.341***

***NORMALIZED TANGENTIAL VELOCITY LEVELS***

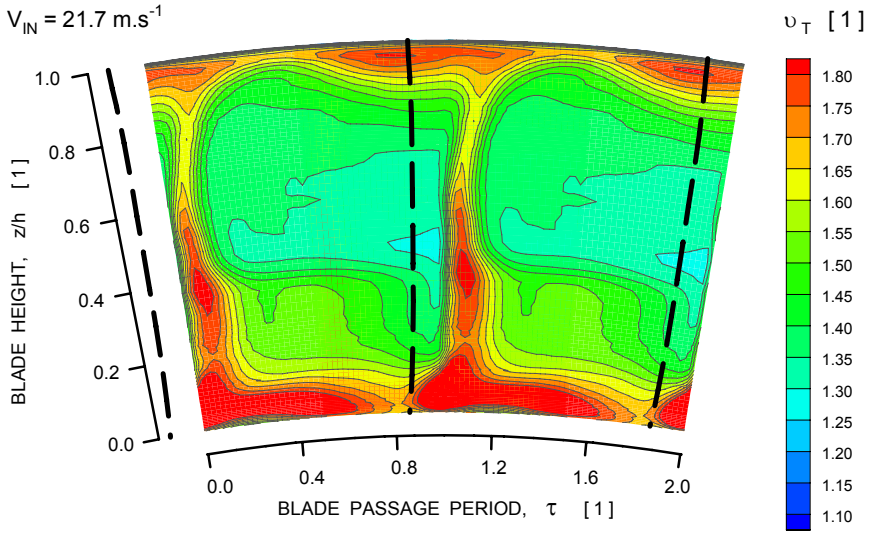


***RANDOM TANGENTIAL VELOCITY UNSTEADINESS***

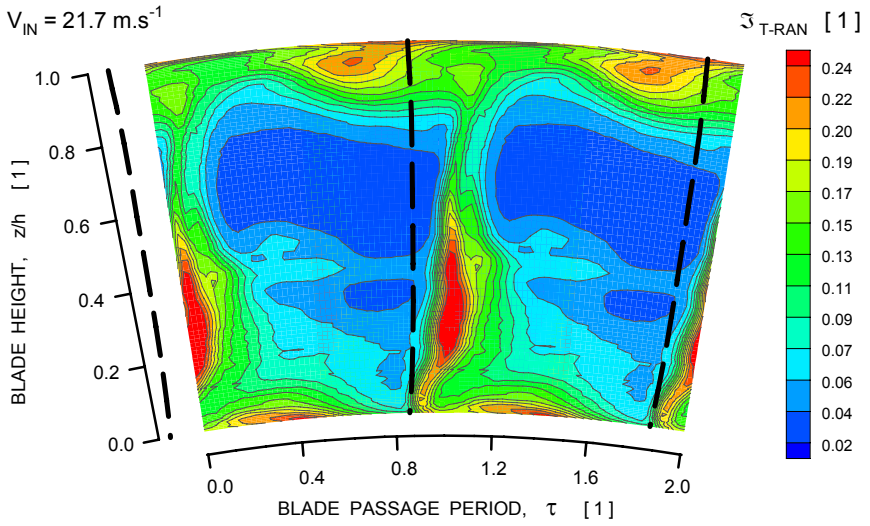


**Fig. 4-18. Contour maps of tangential velocity for a rotor blade passage measured at station *S15A* for flow coefficient of *0.341*.**

***Probe split-fiber R57G, Port S15B, n = 983 min$^{-1}$, Φ = 0.340***

***NORMALIZED TANGENTIAL VELOCITY LEVELS***

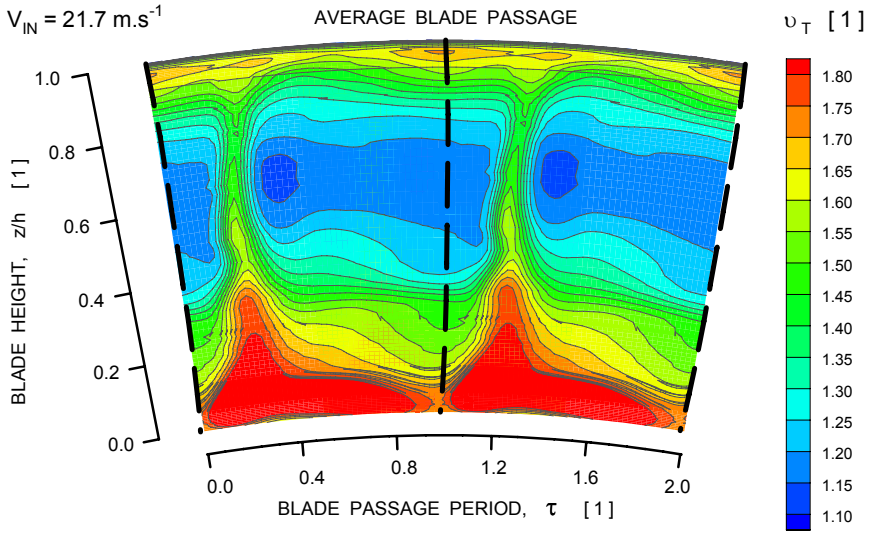


***RANDOM TANGENTIAL VELOCITY UNSTEADINESS***

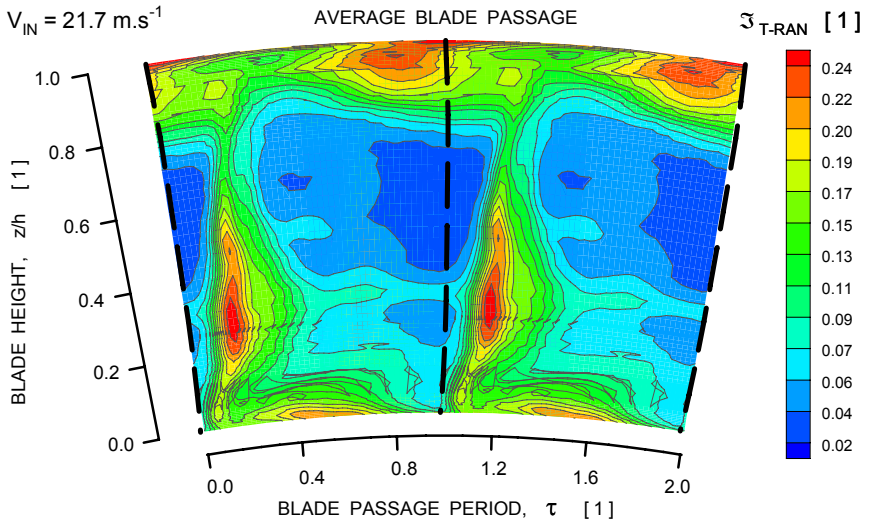


**Fig. 4-19. Contour maps of tangential velocity for a rotor blade passage measured at station *S15B* for flow coefficient of *0.340*.**

***Probe split-fiber R57G, Port S15A, n = 983 min$^{-1}$, Φ = 0.395***

***FLOW ABSOLUTE ANGLE***

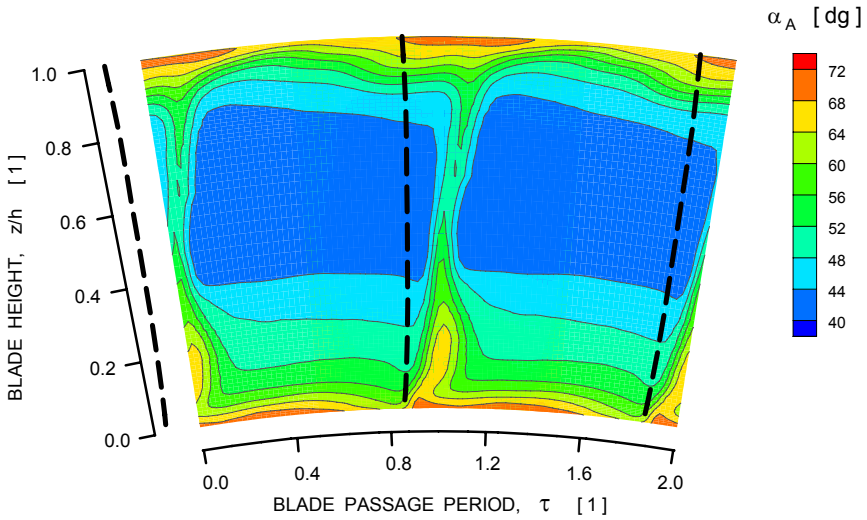


***FLOW DIRECTIONAL UNSTEADINESS***

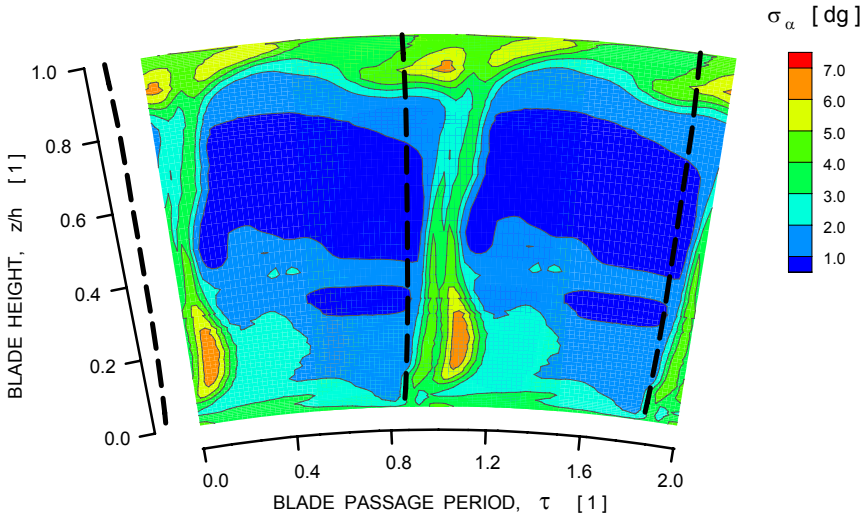


**Fig. 4-20. Contour maps of flow absolute angle for a rotor blade passage measured at station *S15A* for flow coefficient of *0.395*.**

***Probe split-fiber R57G, Port S15B, n = 983 min$^{-1}$, Φ = 0.395***

***FLOW ABSOLUTE ANGLE***

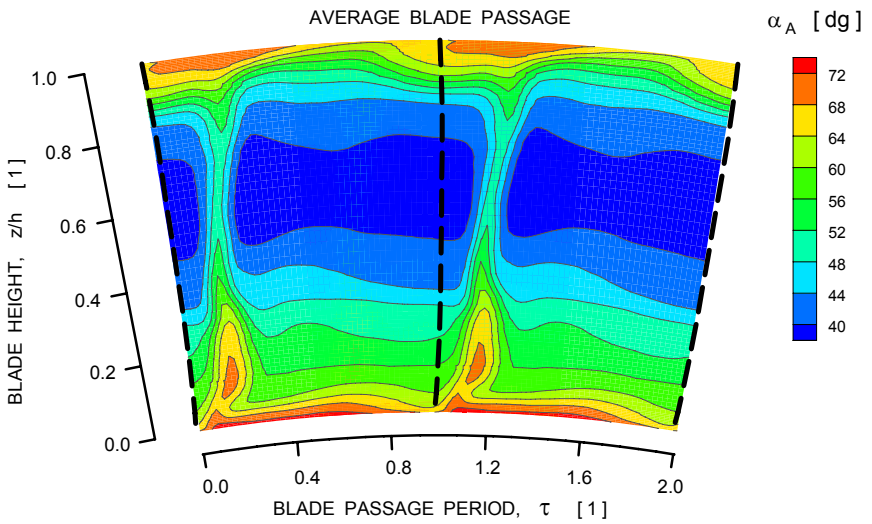


***FLOW DIRECTIONAL UNSTEADINESS***

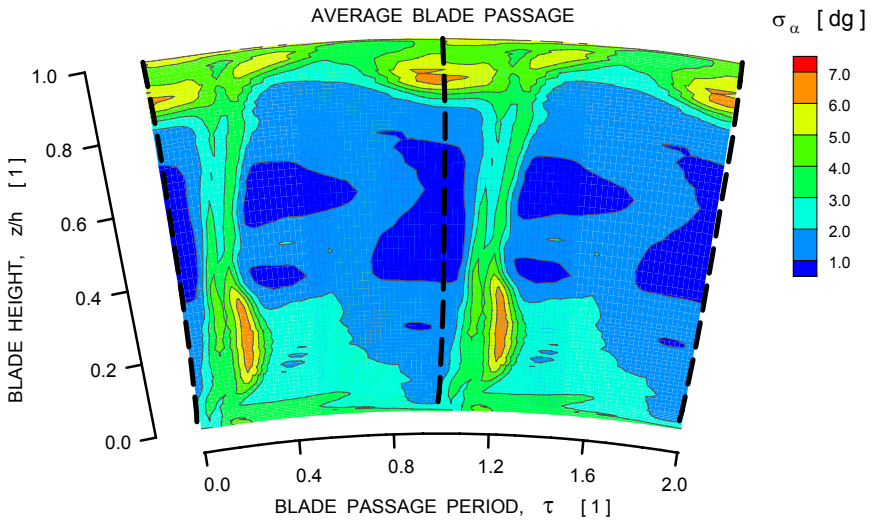


**Fig. 4-21. Contour maps of flow absolute angle for a rotor blade passage measured at station *S15B* for flow coefficient of *0.395*.**

***Probe split-fiber R57G, Port S15A, n = 983 min$^{-1}$, Φ = 0.375***

***FLOW ABSOLUTE ANGLE***

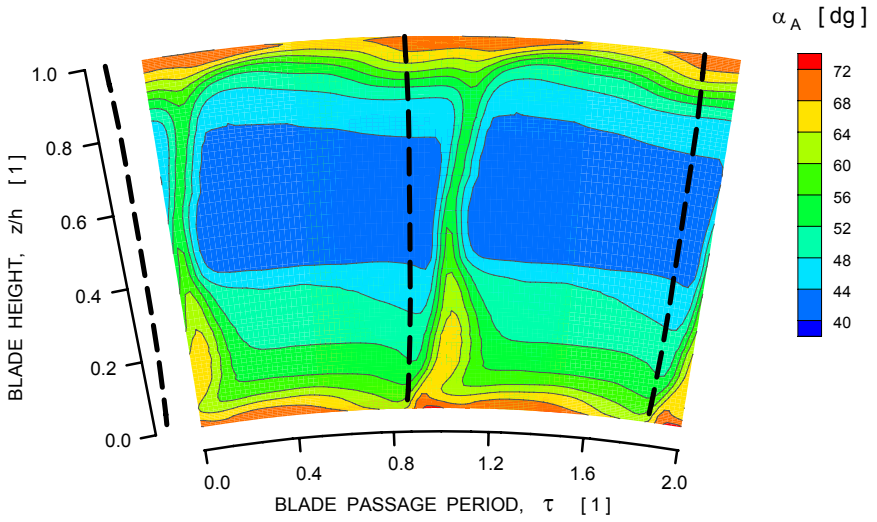


***FLOW DIRECTIONAL UNSTEADINESS***

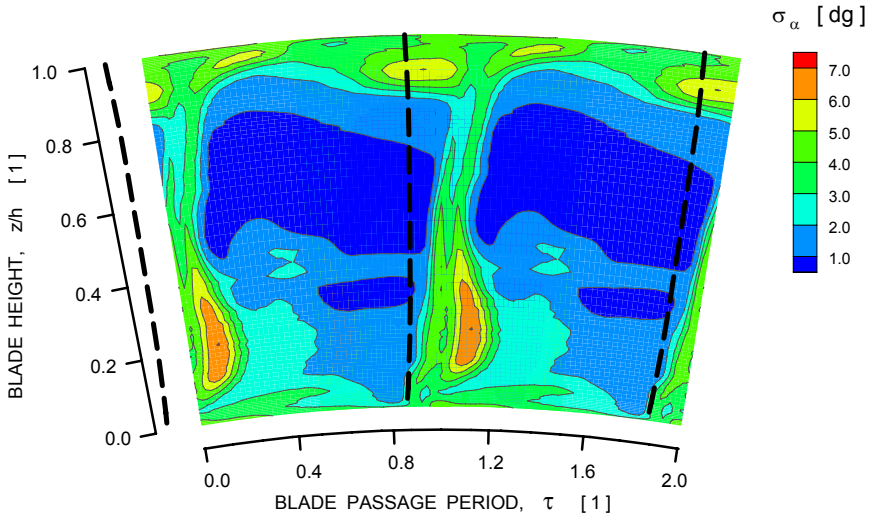


**Fig. 4-22 Contour maps of flow absolute angle for a rotor blade passage measured at station *S15A* for flow coefficient of *0.375*.**

***Probe split-fiber R57G, Port S15B, n = 983 min$^{-1}$, Φ = 0.375***

***FLOW ABSOLUTE ANGLE***

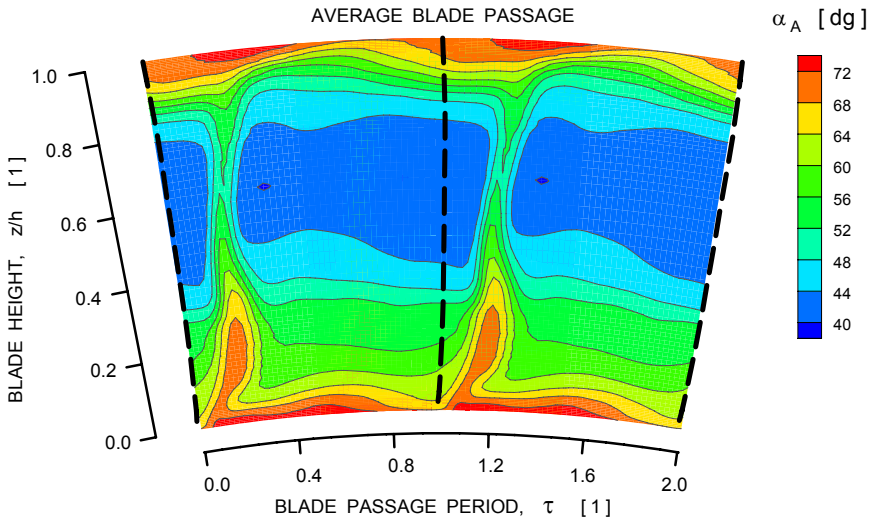


***FLOW DIRECTIONAL UNSTEADINESS***

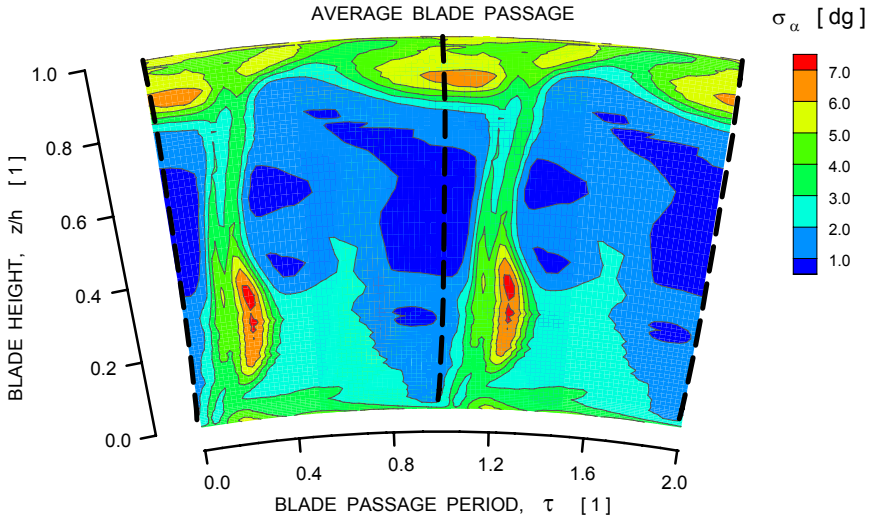


**Fig. 4-23. Contour maps of flow absolute angle for a rotor blade passage measured at station *S15B* for flow coefficient of *0.375*.**

***Probe split-fiber R57G, Port S15A, n = 983 min$^{-1}$, Φ = 0.341***

***FLOW ABSOLUTE ANGLE***

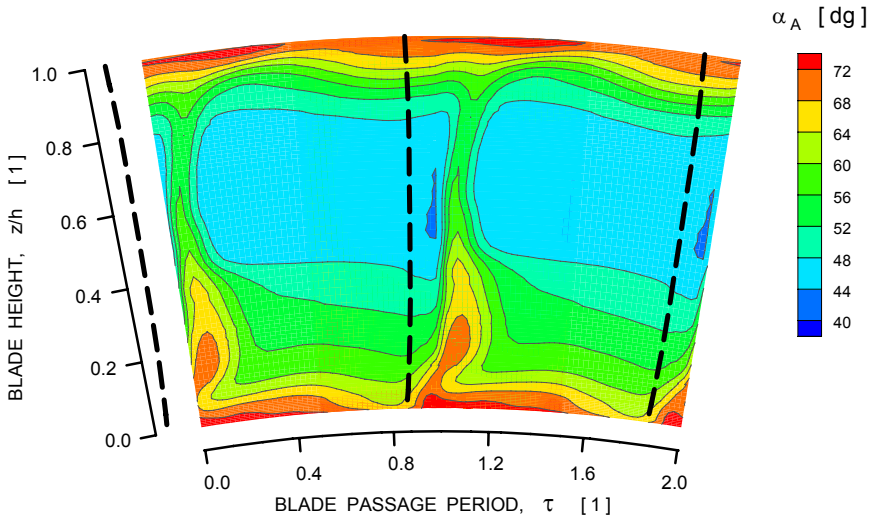


***FLOW DIRECTIONAL UNSTEADINESS***

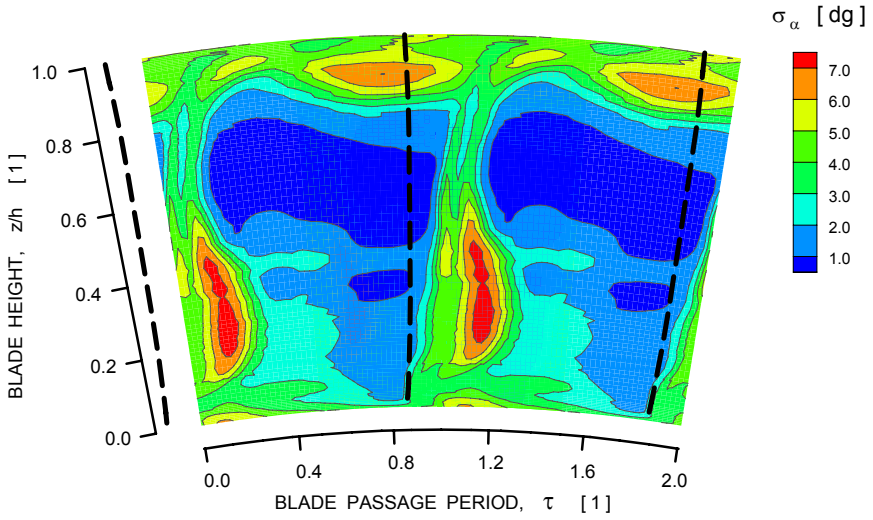


**Fig. 4-24. Contour maps of flow absolute angle for a rotor blade passage measured at station *S15A* for flow coefficient of *0.341*.**

***Probe split-fiber R57G, Port S15B, n = 983 min$^{-1}$, Φ = 0.340***

***FLOW ABSOLUTE ANGLE***

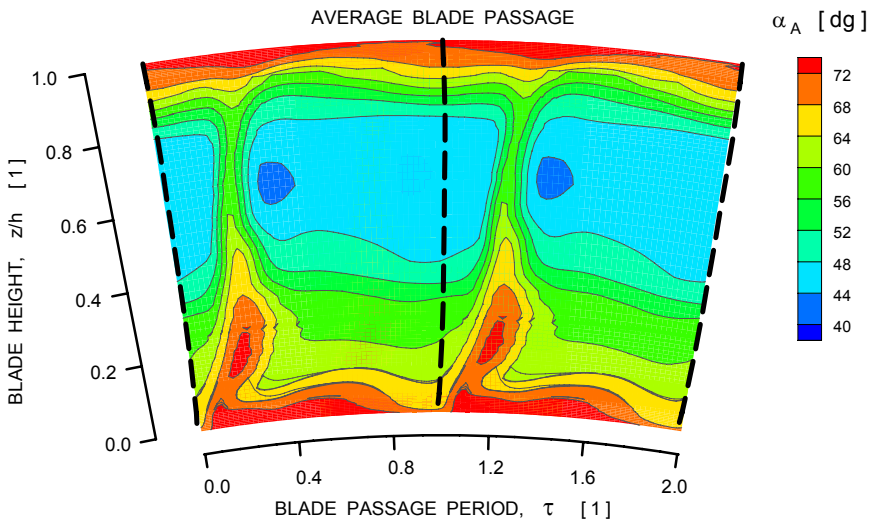


***FLOW DIRECTIONAL UNSTEADINESS***

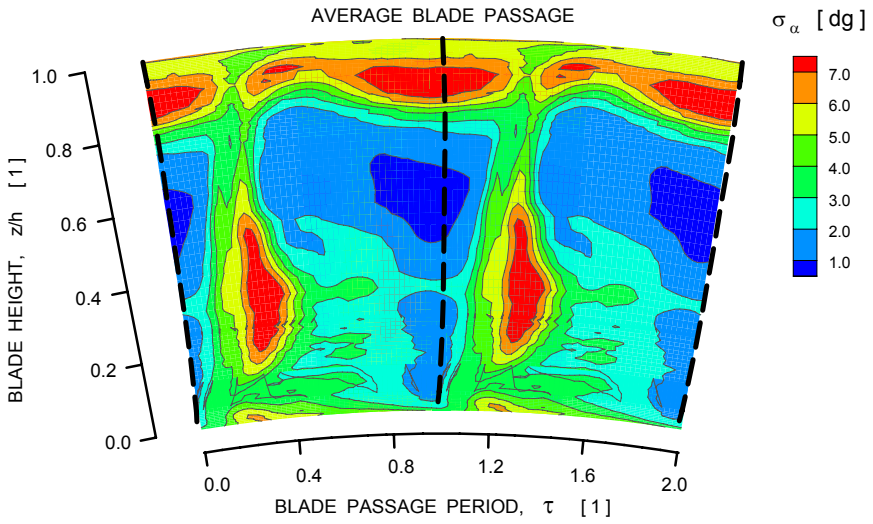


**Fig. 4-25. Contour maps of flow absolute angle for a rotor blade passage measured at station *S15B* for flow coefficient of *0.340*.**

# 5.0 Rotor-Revolution Ensemble Averages

Blade ensemble averaging yields parameter distributions that represent flow in an idealized single blade channel. All variations in the flow due to differences in geometry of individual blade channels or of the entire rotor are suppressed by the blade ensemble averaging process for the averaged signals. These variations, however, contribute to the unsteadiness level of blade ensemble averages. To trace differences among individual blade channels, the ensemble averaging must be based on a time period that is equal to one rotor revolution.

The same sets of unsteady data that were used to generate blade-ensemble averages were reprocessed to generate rotor-ensemble averages. The time segments of unsteady data are *5 s* long, and a period of one rotor revolution is *61 ms*, therefore each rotor-ensemble average is built from *81* consecutive rotor revolutions only, in contrary to *3100* blade passages for the case of blade passage averaging. Still the number of 'revolution samples' is sufficiently high for the results to be statistically meaningful.

## 5.1 Near Stall Operation Point

Rotor ensemble averages for axial and tangential velocity components and the absolute flow angle measured at station *S15B* for a compressor operation condition at a flow coefficient of *0.340* are shown in Figs. 5-1 through 5.3 for 12 positions along the blade span. The particular span positions and mean values of flow parameters are posted at each diagram. A glance at these plots reveals the presence of huge circumferential variations of these parameters in the blade tip region (upper *20%* of the blade span). On the other hand, the flow field is quite steady, on the rotor revolution scale, in the blade midspan region. The circumferential variations increase very slightly in the blade root region, but they are barely detectable. The reasons for the large flow parameter variations along the rotor circumference in the blade tip are not readily obvious. One of the factors might be possible variation in the size of the blade tip clearance due to eccentricity in the rotor motion as indicated by the variations in the OPB signal discussed in the previous section (Fig. 4-2).

## 5.2 Flow Disturbance Due to Rotor Instrumentation

There is a noticeable velocity and direction anomaly in the lower half of the blade span located in the blade passage between the fourth and fifth rotor blade wakes (counted from the left in the diagrams in Figs. 5-1 through 5-3). This flow disturbance was generated by a stem of a total pressure probe located in the first rotor. A photograph of this probe is in Fig. 5-4. Although the probe was not used in this experimental effort to acquire aerodynamic data, in the event it served two very useful purposes. First, it helped in verifying the data reduction methodology, in particular the timing of the rotor-ensemble averaging procedure. Second, it clearly illustrates the extent of unavoidable flowfield distortion due to presence of aerodynamic probes in the flow.

The positions of the rotor total pressure probe, rotor blades, and of the OPR are depicted in photograph in Fig. 5-5. Rotor blades are numbered in the clockwise direction starting with the first blade past the OPR marker. Two aluminum blades, mentioned previously, are labeled *R5* and *R6*. The stator vanes are counted also in the clockwise direction, but numbering starts at the casing top (12 o'clock) as it was shown already in Fig. 1-3. The stationary OPR sensor is located at an angular position of *180.0 dg* and the OPB sensor is at *275.2 d*g; both angular position values are determined in the stator frame of reference.

Mutual positions of casing probes and rotor blades are schematically depicted in Fig. 5-6. The rotor is depicted at a position when the OPR signal was generated, that is, when the rotor marker is facing the OPR sensor mounted in the casing frame. As can be seen here, at this instant the stator and rotor angular reference frames are shifted by *180 dg*. It should be stressed here that rotor blade positions are represented by the blade stacking axes. A plan view of the blade and vane airfoil contours at the blade midspan height is shown in Fig. 5-7 for the same time instant as in Fig. 5-6. Expected positions of the rotor blade wakes

(cyan lines) and the rotor probe wake (magenta line) are also shown in Fig. 5-7. The wake positions are shown for flowfield expected at a compressor flow coefficient of *0.375* as discussed in Fig. 1-6.

Allocation of data signals to individual rotor blades is explained in Fig. 5-8. There are four diagrams in this figure; the first diagram is for the OPR signal, the second diagram is for the OPB signal, the third diagram depicts the axial velocity component as measured at station *S15A*, and finally the last diagram depicts the axial velocity component as measured at station *S15B*. A rotor revolution start time is allocated to the middle of the OPR signal, which thus splits the OPR signal into a 'start half' and 'stop half' as shown in the first diagram in Fig. 5-8. Allocation of the OPB signal to individual blades is straightforward. As seen in Figs. 5-6 and 5-7 the blade labeled *R11* is just to pass the OPB sensor when the timing of the revolution starts, thus the first signal on the left in the second diagram in Fig. 5-8 is of the blade *R11*. Counting down the blade signals along the rotor circumference, which is in the direction of increasing time, it appears that the two tall signal spikes are generated by aluminum blades *R6* and *R5* (see Fig. 5-5). Allocation of blades and their wakes in the axial velocity diagrams in Fig. 5-8 can be done with help of the airfoil layout and expected wake trajectories as shown in Fig. 5-8. As seen here at the rotor 'time zero' (*0 dg*), the wake of blade *R9* is just passing the probe inserted at station *S15A*. It follows that just before the rotor revolution is complete, the last blade wake passing the probe at *S15A* will be the one of blade *R10*, closely followed by wake of the rotor probe. The situation is similar for measurement station *S15B*, however in this case the first wake to pass the probe is of blade *R13*. Using these sequences the recorded wakes in the third and forth diagrams of Fig. 5-8 can be allocated to rotor blades.

Knowing the allocation of data signals to rotor blades, data acquired at two measurement stations can be mutually shifted in order to be plotted respective to the blade rather than to the individual measurement stations. An example is shown in Fig. 5-9. Here, changes of the rotor blade-to-blade velocity profiles caused by the probe wake interaction with stator vanes, either in the stator vane midpitch or vane stagnation regions, can be directly investigated for a given rotor blade.

### 5.3 Rotor Average Contour Maps

Contour maps based on rotor-revolution ensemble averaging are presented in Figs. 5-10 through 5-12. The contour maps are shown for the axial velocity levels at the measurement station *S15B* only. The maps depict three adjacent rotor blade passages, namely passages between blades *R11-R10*, *R10-R9*, and *R9–R8*, unlike in the case of blade-ensemble averaging where the same blade passage was depicted repeatedly in two adjacent channels for clarity. As already shown above, the passage between blades *R10-R9* confines the wake of the rotor total pressure probe (see Figs. 5-4 through 5-7).

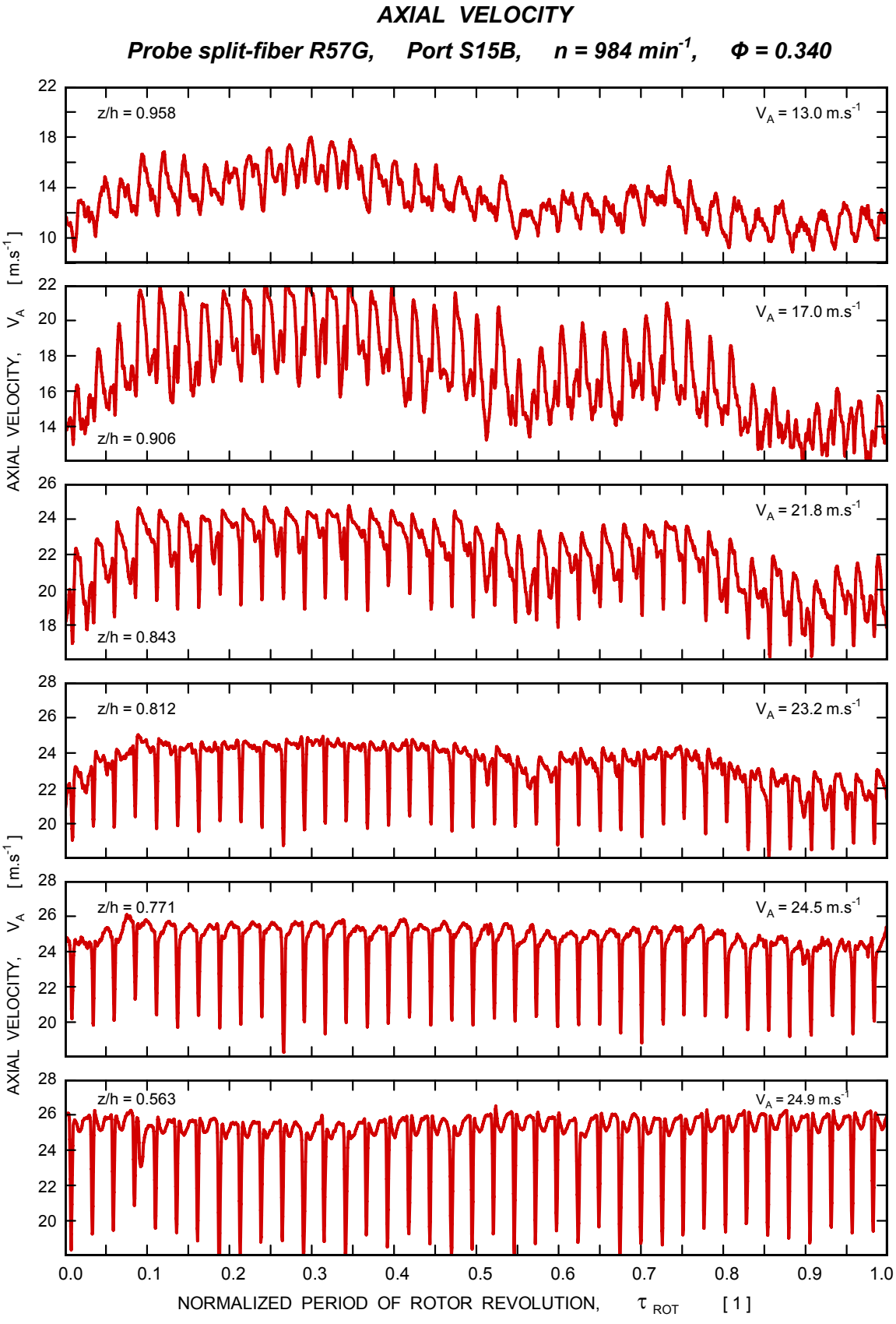


**Fig. 5-1a. Rotor-ensemble averages of axial velocity component measured at station *S15B* for a flow coefficient of *0.340*.**

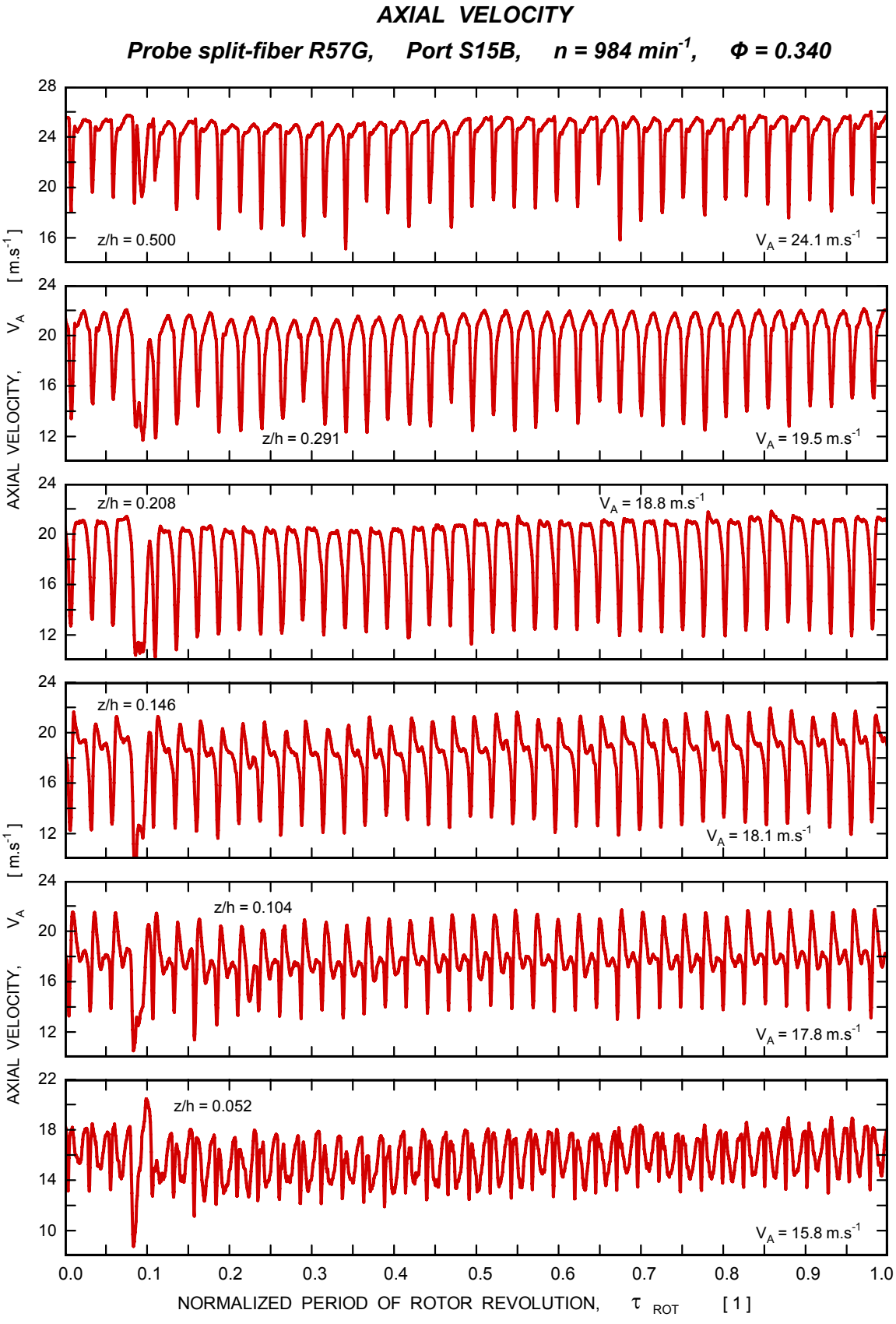


**Fig. 5-1b. Rotor-ensemble averages of axial velocity component measured at station *S15B* for a flow coefficient of *0.340*.**

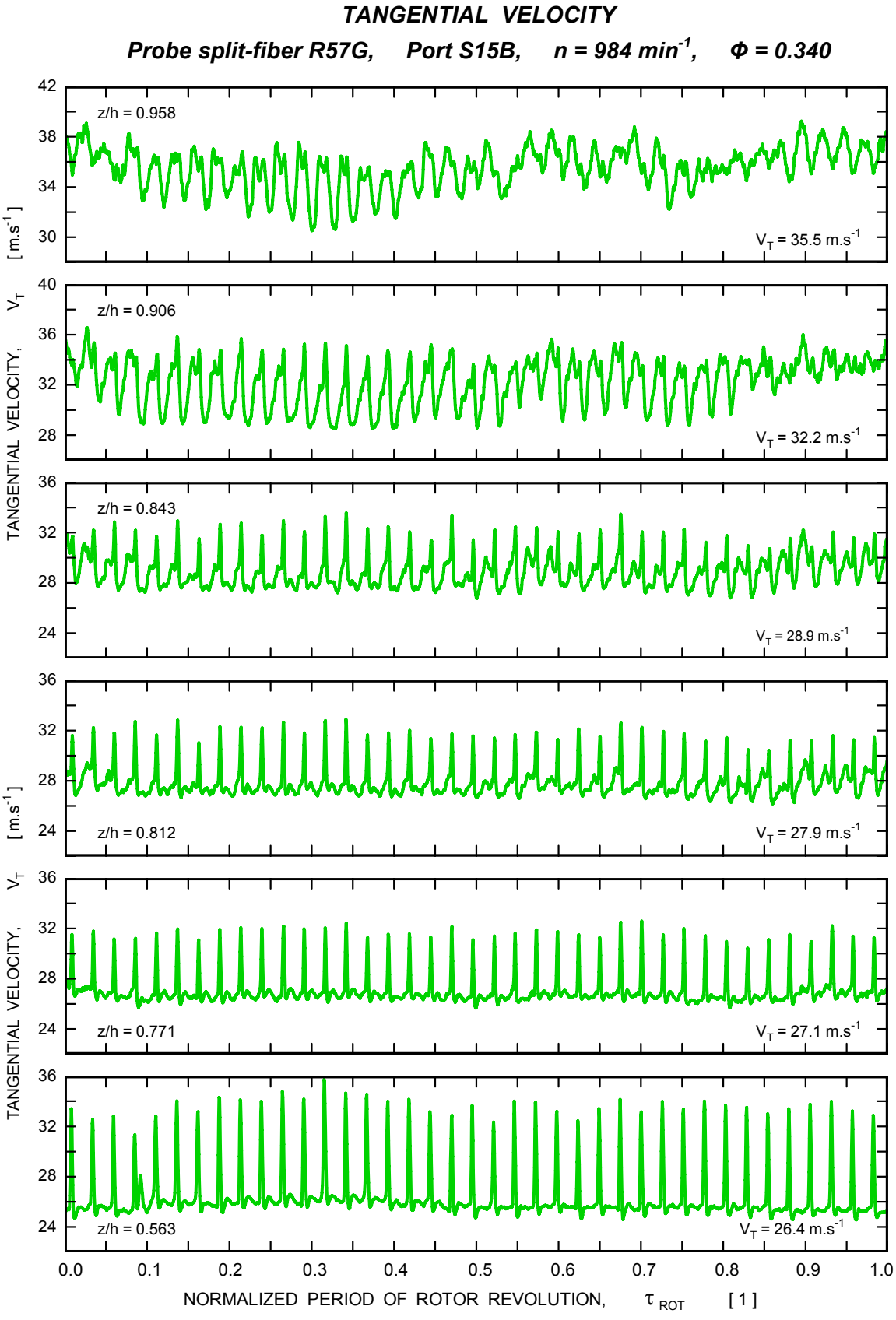


**Fig. 5-2a. Rotor-ensemble averages of tangential velocity component measured at station *S15B* for flow coefficient of *0.340*.**

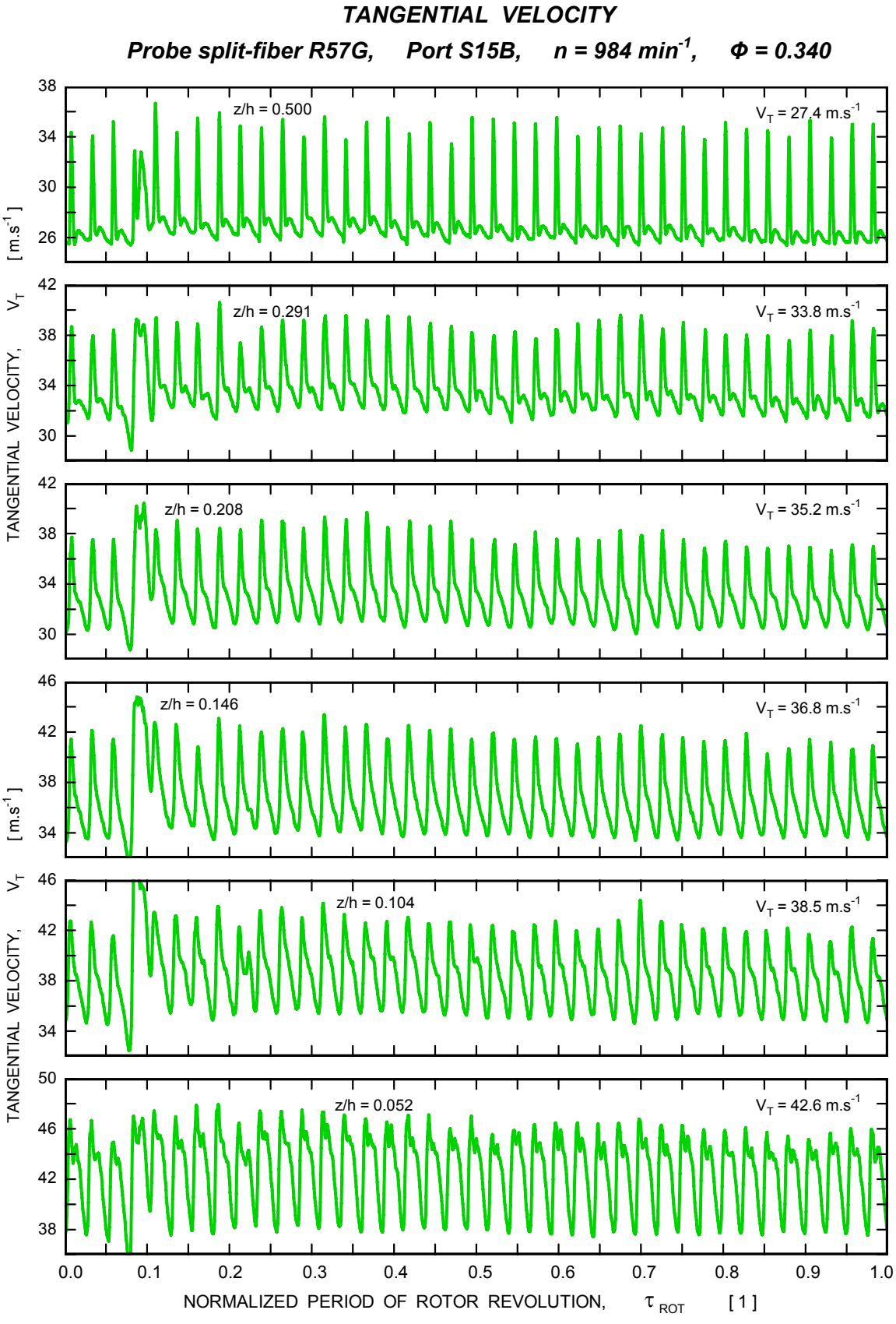


**Fig. 5-2b. Rotor-ensemble averages of tangential velocity component measured at station *S15B* for flow coefficient of *0.340*.**

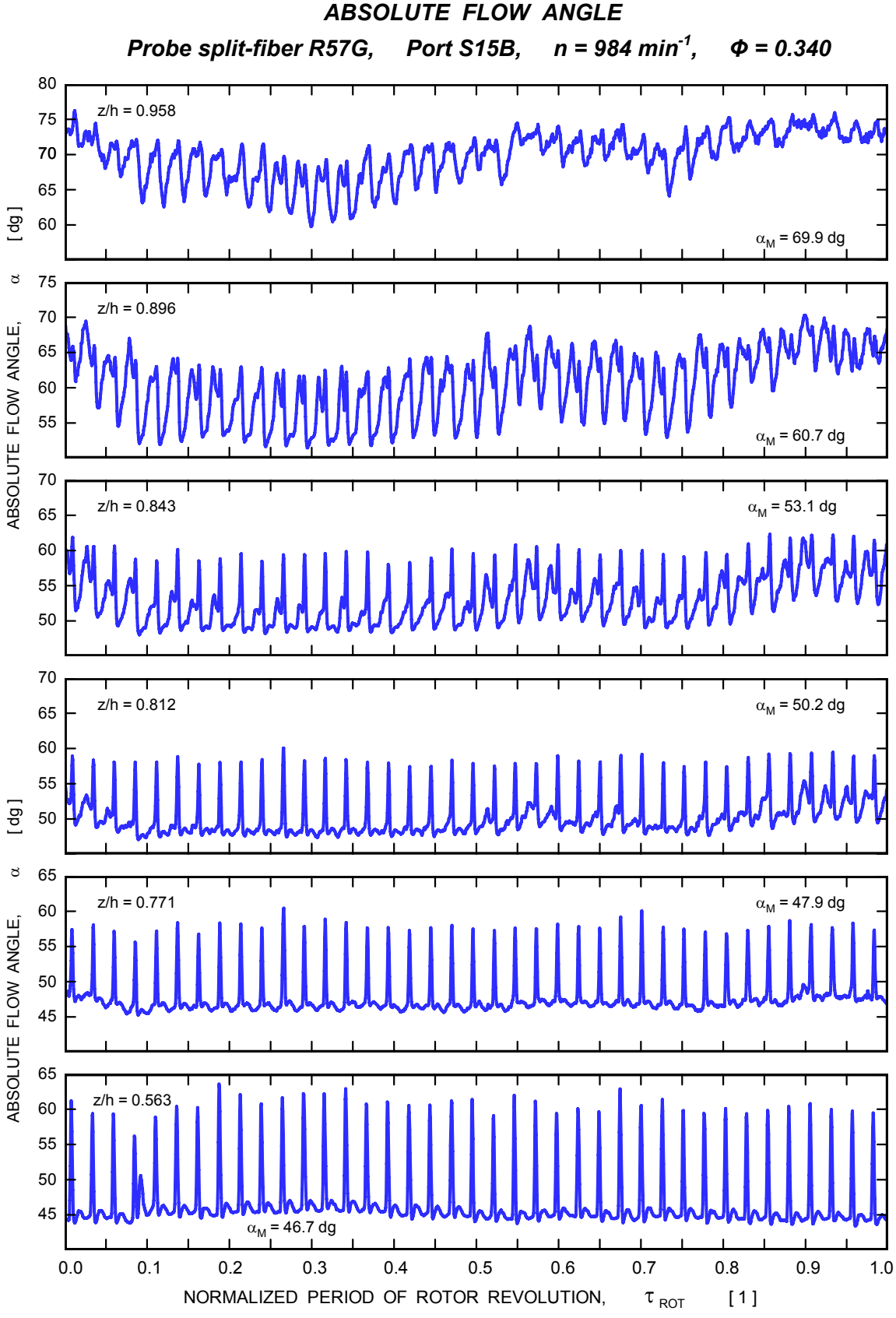


**Fig. 5-3a. Rotor-ensemble averages of absolute flow angle measured at station *S15B* for flow coefficient of *0.340*.**

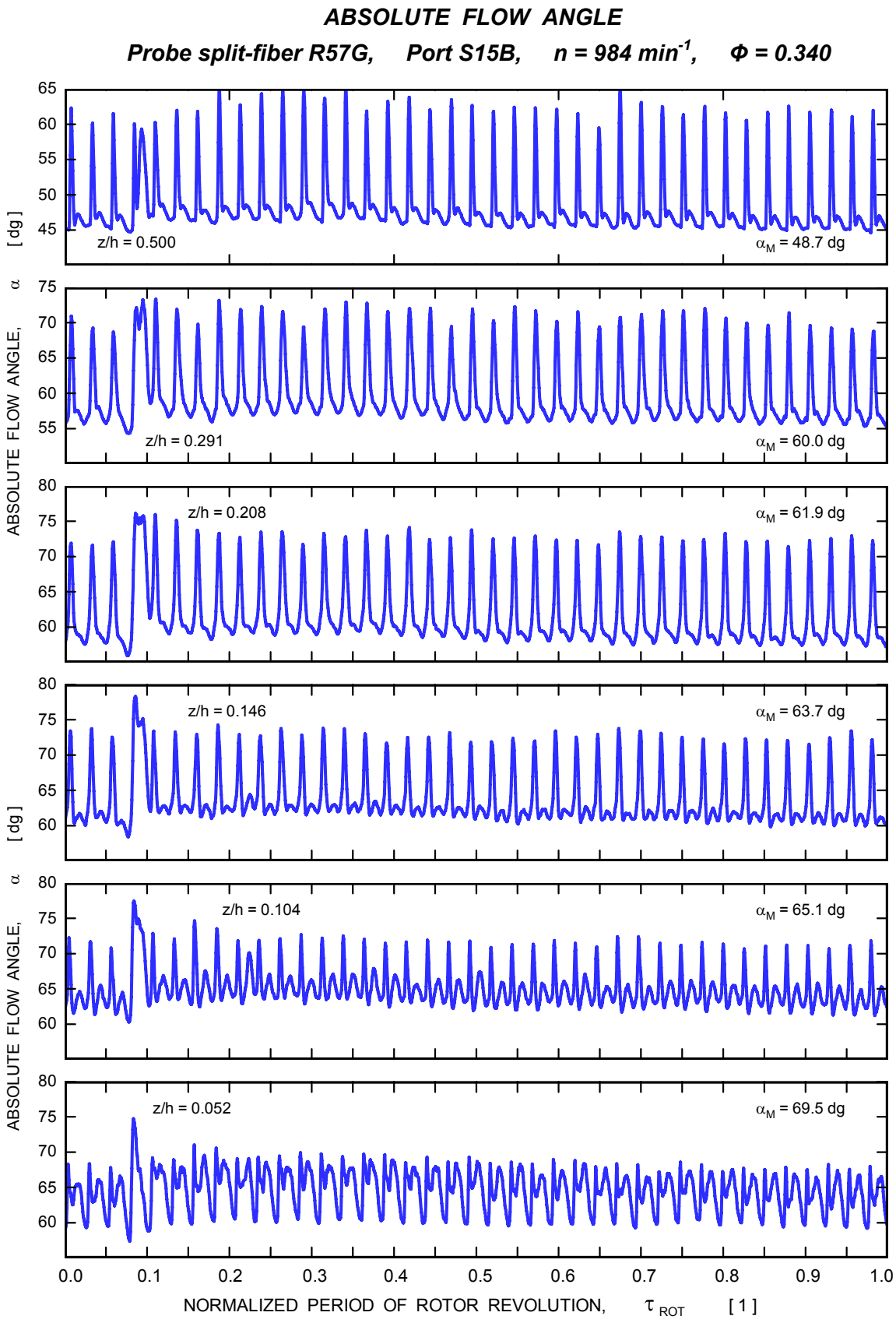


**Fig. 5-3b. Rotor-ensemble averages of absolute flow angle measured at station *S15B* for flow coefficient of *0.340*.**

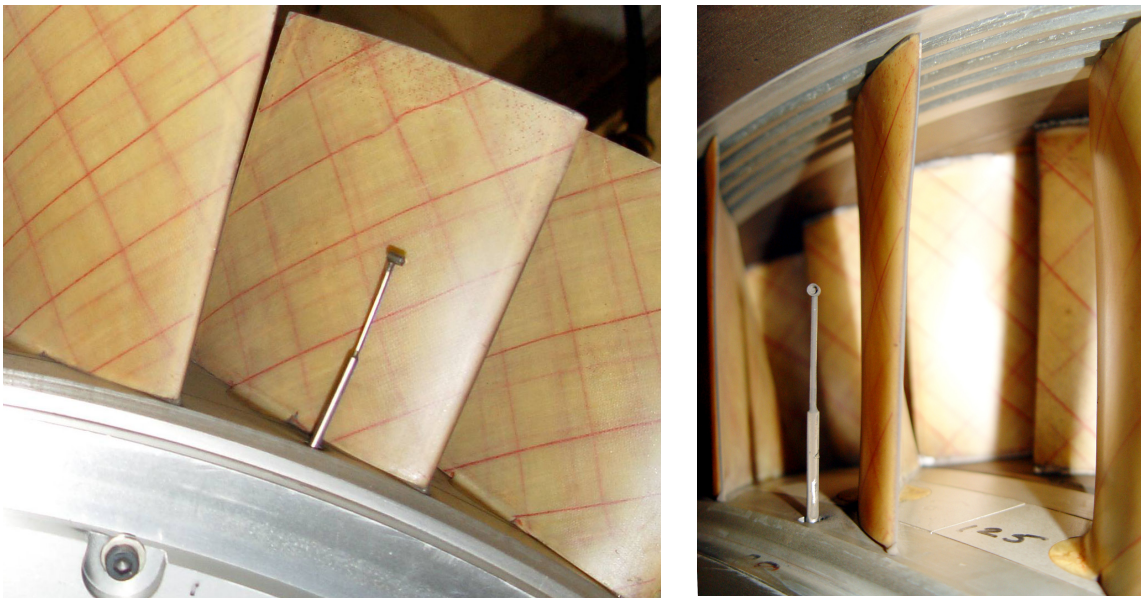

Fig. 5-4. Total pressure probe in a rotor blade passage.

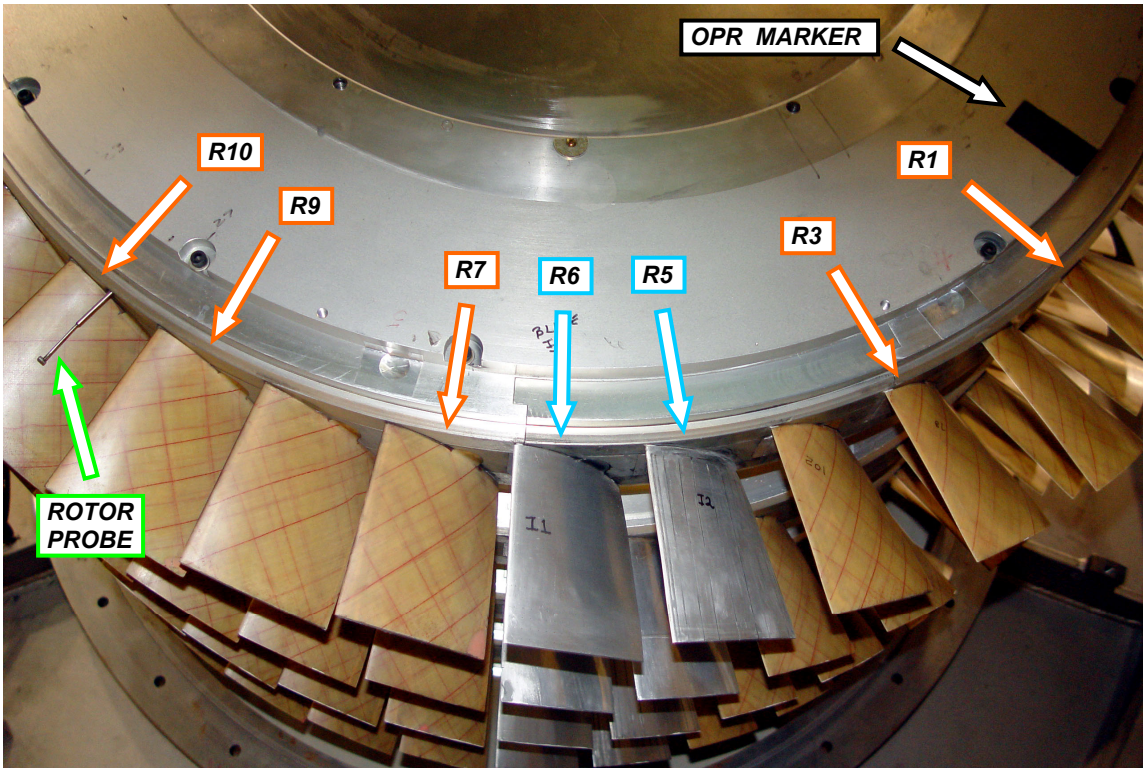


Fig. 5-5. View of the first rotor.

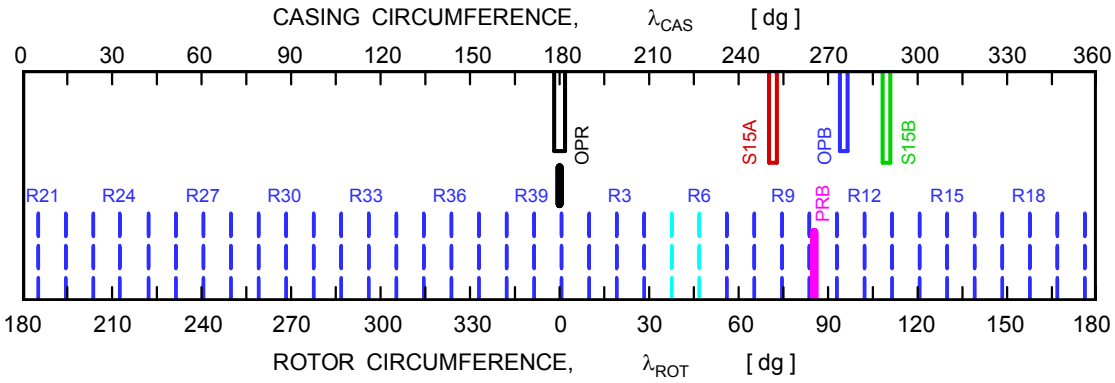


**Fig. 5-6. Layout of probes and rotor blades on the compressor casing and first stage rotor.**

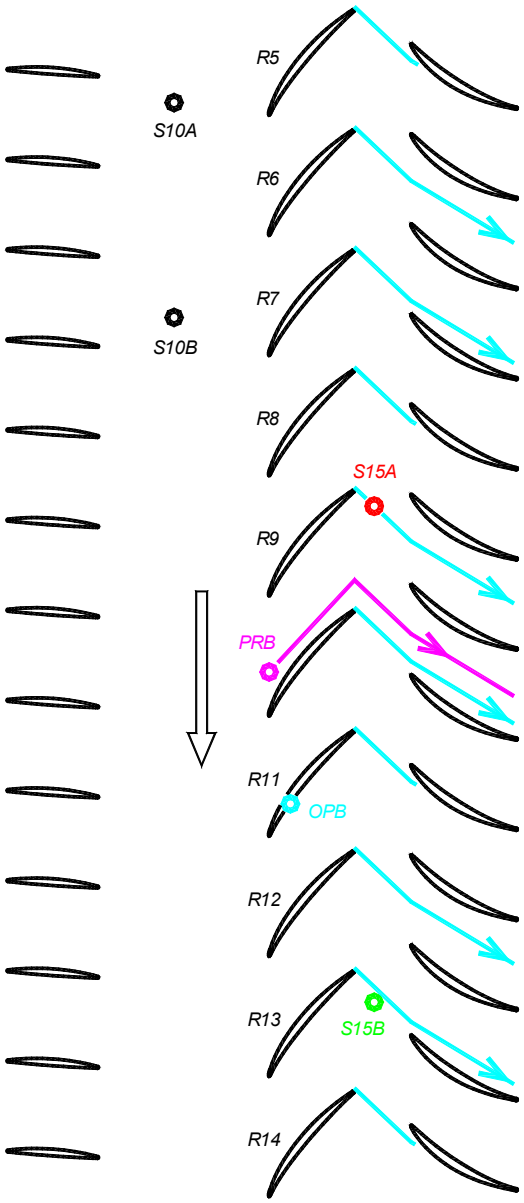


**Fig. 5-7. Layout of probes and rotor blades at blade midspan height, and expected blade and rotor probe wakes at a time instant when OPR mark signal is generated.**
**PRB indicates location of the rotor probe shown in Figs. 5-4 and 5-5.**

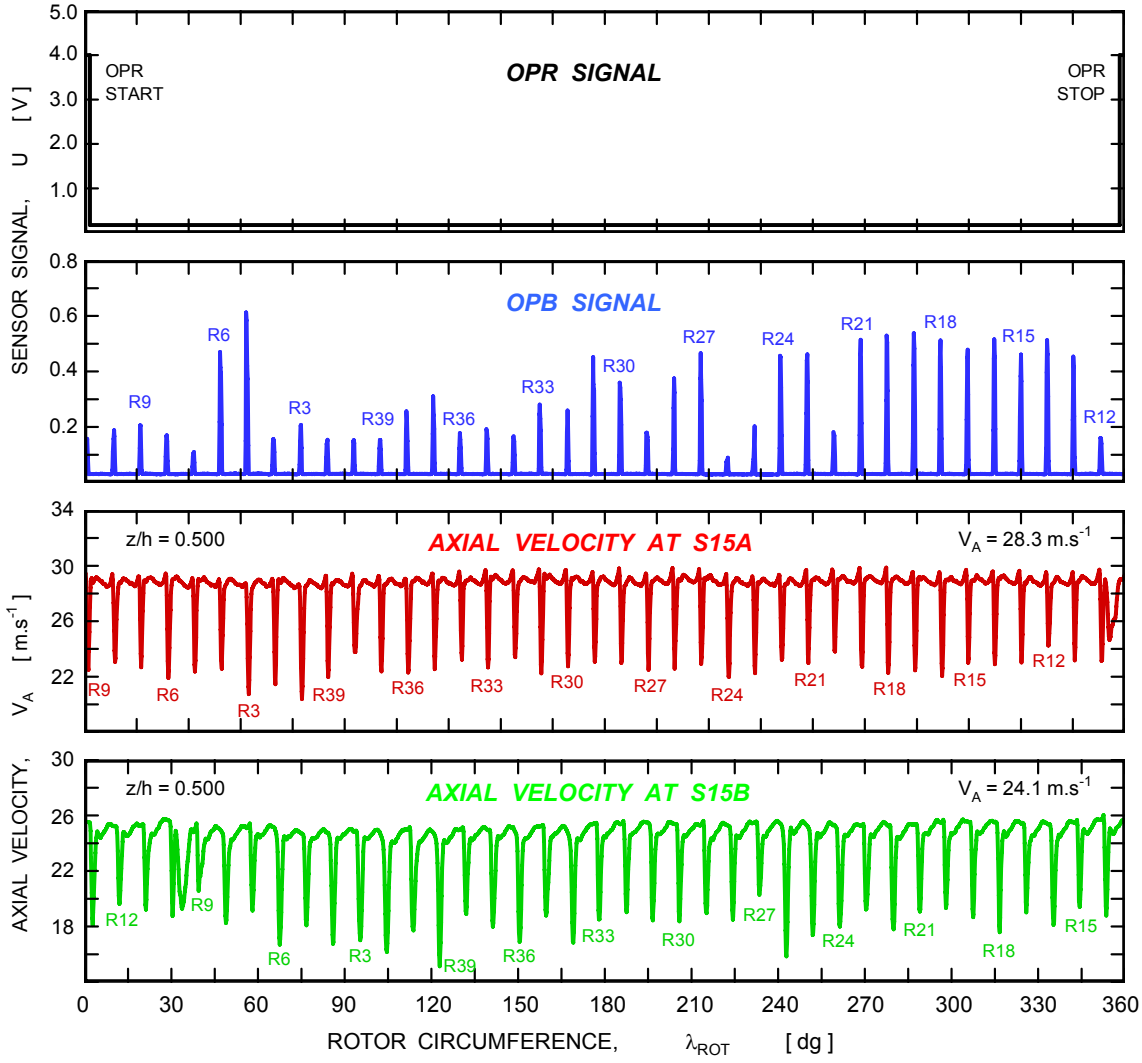


**Fig. 5-8. Allocation of data signals to rotor blades.**

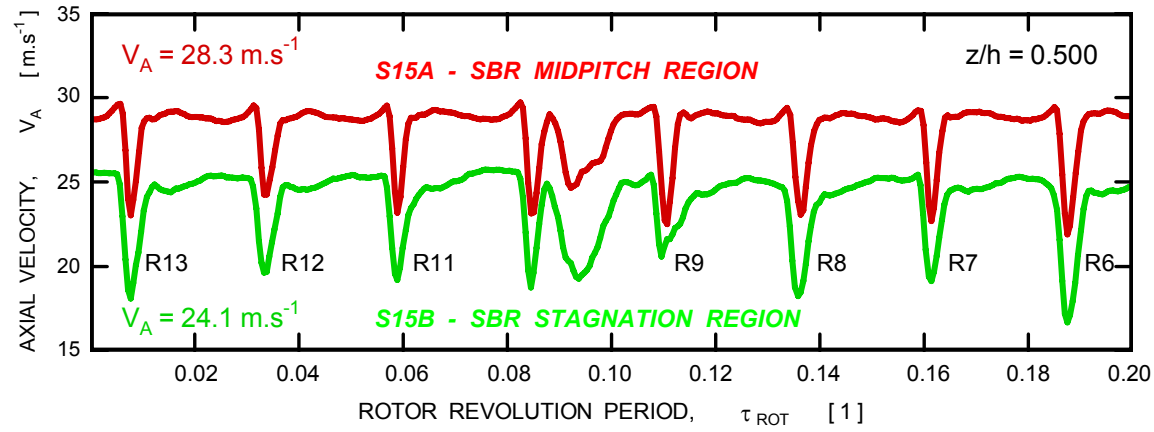


**Fig. 5-9. Axial velocity disturbance due to a rotor probe.**

***Probe split-fiber R57G, Port S15B, n = 983 min$^{-1}$, Φ = 0.395***

***NORMALIZED AXIAL VELOCITY LEVELS***

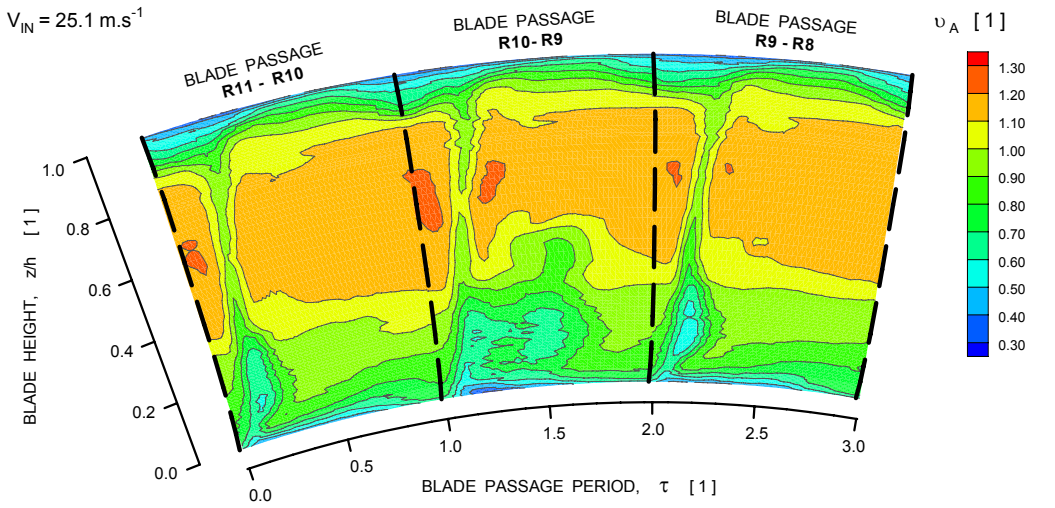


***RANDOM AXIAL VELOCITY UNSTEADINESS***

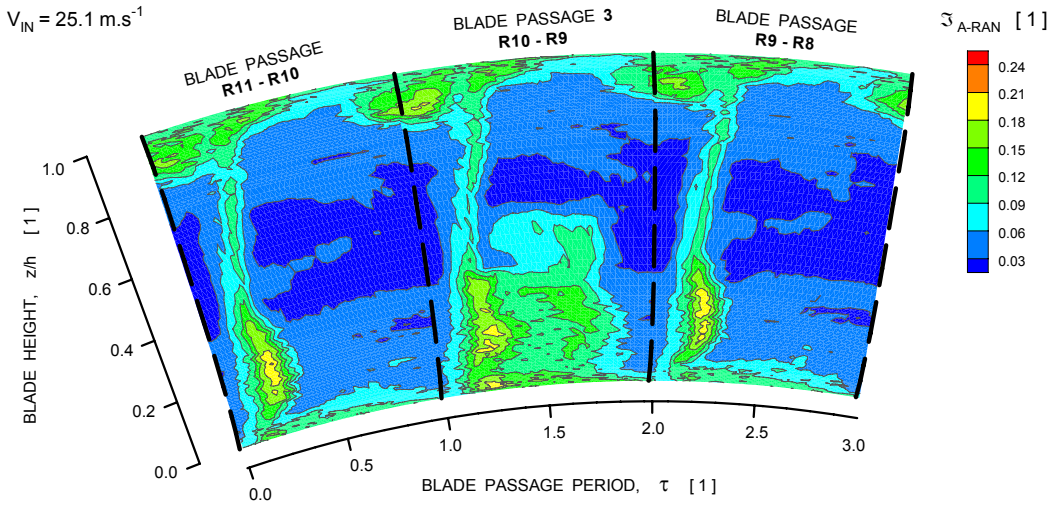


**Fig. 5-10. Contour maps of axial velocity for a rotor blade passage measured at station *S15B* for flow coefficient of *0.395*.**

***Probe split-fiber R57G, Port S15B, n = 983 min$^{-1}$, Φ = 0.376***

***NORMALIZED AXIAL VELOCITY LEVELS***

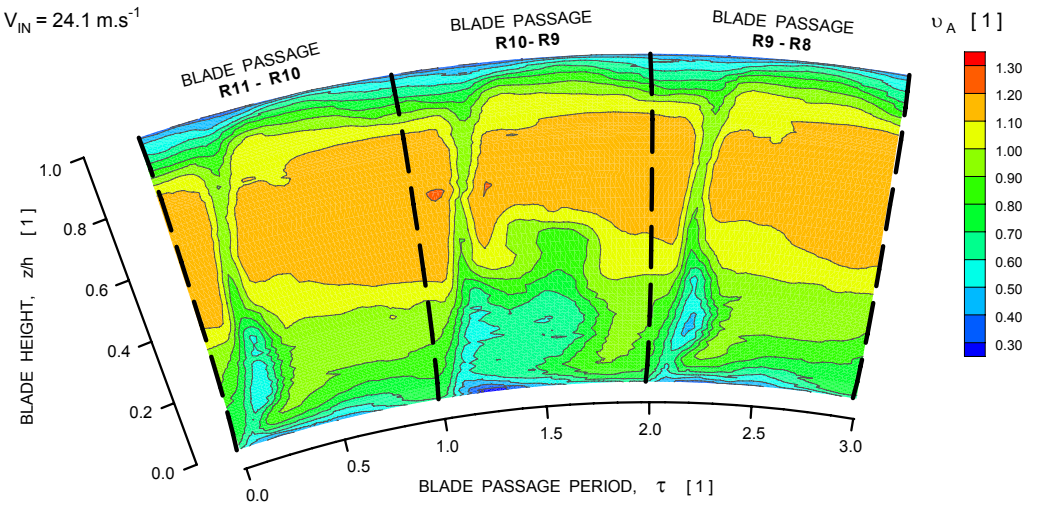


***RANDOM AXIAL VELOCITY UNSTEADINESS***

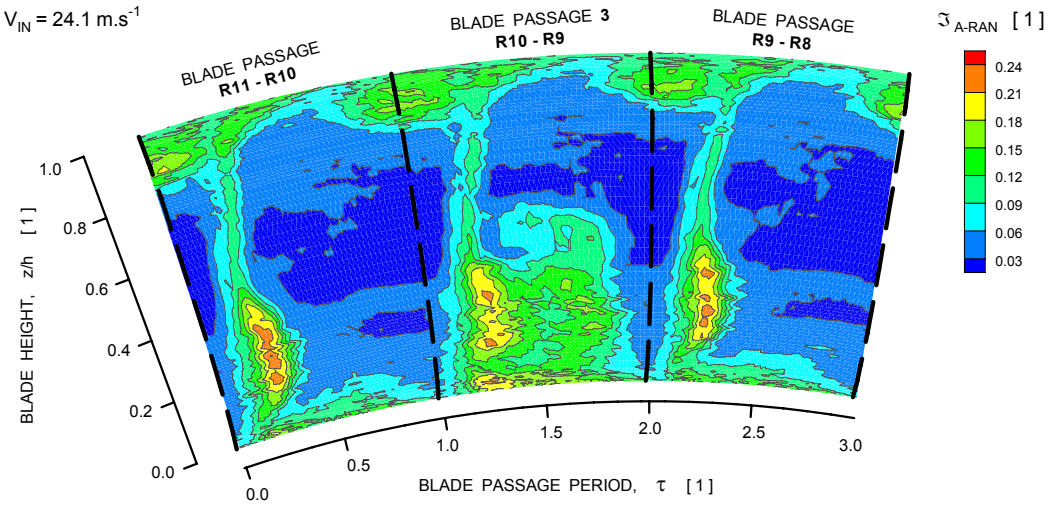


**Fig. 5-11. Contour maps of axial velocity for a rotor blade passage measured at station *S15B* for flow coefficient of *0.376*.**

***Probe split-fiber R57G, Port S15B, n = 983 min$^{-1}$, Φ = 0.340***

***NORMALIZED AXIAL VELOCITY LEVELS***

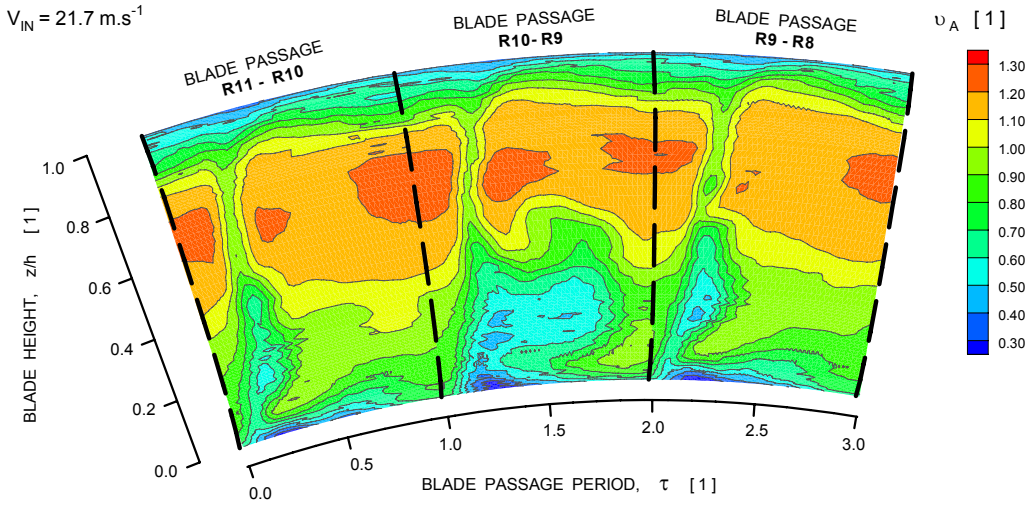


***RANDOM AXIAL VELOCITY UNSTEADINESS***

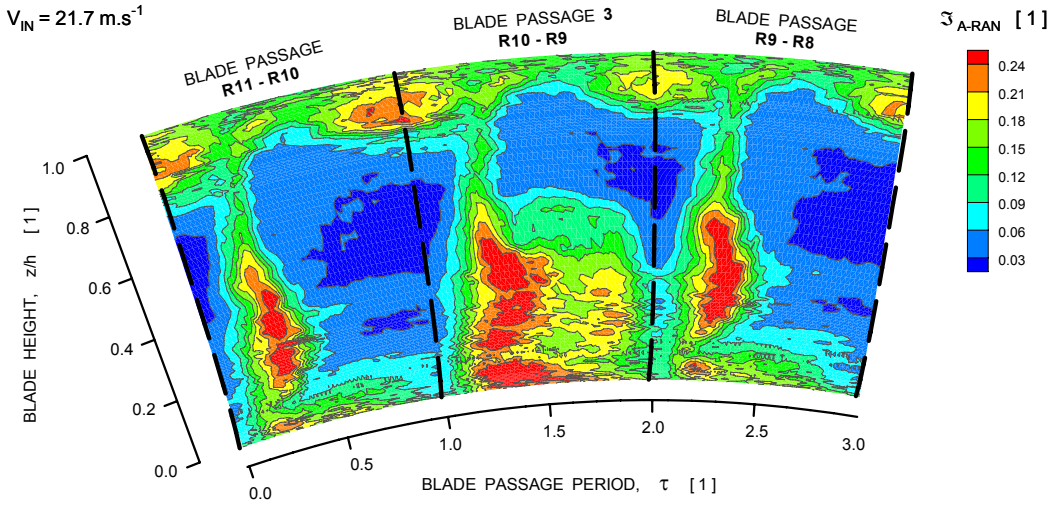


**Fig. 5-12. Contour maps of axial velocity for a rotor blade passage measured at station *S15B* for flow coefficient of *0.340*.**

# 6.0 Spectral Analysis

The acquired experimental data, reduced to unsteady velocity signals, were subjected to spectral analysis using the Fast Fourier Transform (FFT) algorithm from the LabVIEW subroutine library (Ref. 6-1). All data presented were computed as amplitude spectra. First, two types of spectra were generated that are labeled overall and averaged spectra. Second, an additional spectrum, labeled asynchronous component, was generated to enhance velocity fluctuations that are not multiples of the compressor shaft speed (frequency).

## 6.1 Overall and Averaged Velocity Spectra

The overall spectra were generated by applying the FFT algorithm to the entire *5 s* long segment of velocity magnitude data. As mentioned before, each data segment contains *81* rotor revolutions or over *3100* blade passages. Spectrum analysis was performed over a frequency range from *0* to *10 kHz*. Each velocity data segment contained *160 000* velocity samples acquired at a rate of *32 kHz*. Because each data segment represents an interval of velocity data *5 s* long, the frequency resolution of the overall spectra data is very fine, about *0.2 Hz*.

Besides overall spectra, averaged spectra were also computed. Generally, the advantage of spectra averaging is an increased confidence in the amplitude levels. However, to utilize fully this advantage long segments of data are needed. The length of data segments in our case was restricted to *5 s* due to storage memory restrictions. Because the same data segments were used for raw spectra as well as for data averaging, the averaged spectra have coarser frequency resolution as described further.

In order to generate averaged spectra, each velocity data segment was divided into *16* subsegments, which resulted in each new subsegment being equal to an interval of *5* rotor revolutions. Then, a separate amplitude spectrum was calculated for each subsegment, and a resulting spectrum was obtained as an average of *16* individual spectra. The averaging was done as a square root of one sixteenth of the sum of amplitude squares for all *16* subsegments. Each individual spectrum was generated from a segment that is *0.3125 s* in duration. Consequently, as mentioned above, the resulting frequency resolution for the averaged spectra is only *3.2 Hz*, which is significantly worse than is the one for the raw spectra (*0.2 Hz*).

Raw and averaged spectra for probe port *S10B*, which is the station upstream of the rotor, are depicted in Figs. 6-1 and 6-2 (the frequency axis uses a logarithmic scale). These two sets of data were acquired by a split-fiber probe (*R57G*) for practically identical conditions which were close to the last stable point on a speed line. A high similarity of these two data sets indicates good repeatability of test conditions and reliability of data acquisition procedures. The location of probe port *S10B* is indicated in Figs. 1-3 and 5-7. Each figure shows the spectra for five radial positions in the shroud area. For the precise probe position with respect to the rotor blade tip see Fig. 2-3. As seen in Figs. 6-1 and 6-2, the blade passing frequency (*639 Hz*) is detectable for the probe located at the shroud radius. As the probe is traversed deeper inside the flowpass, the blade passing frequency spike disappears, and only the shaft frequency (once per revolution, *16 Hz*) is detectable.

Raw and averaged velocity spectra generated from signals acquired behind the first rotor are shown in Figs. 6-3 through 6-6. Data in the first two figures were taken at probe port *S15A* and data in Figs. 6-5 and 6-6 were taken at probe port *S15B*. Location of probe ports *S15A* and *S15B* are shown in Figs. 1-3 and 5-7. Data presented were taken by two different probes: split-fiber probe (*R57G*), and single-wire probe (*P13B*). As seen in the spectra acquired by these probes, the shaft frequency (*16 Hz*) is detectable throughout the range traversed. The blade passing frequency and its second harmonic (*639* and *1278 Hz*) are represented by narrow spikes, particularly in the raw spectra plots (high frequency resolution). Contrary to the spectra acquired upstream of the first rotor, the spectra behind the rotor show the blade passing frequency as a dominant one, in particular past the rotor blade out of the blade tip region. In the tip gap region, close to the compressor shroud, the blade passing frequency is manifested by its second harmonic. The dominance of the second harmonic is consistent with the blade ensemble averaged data shown in Section 4.3 (top diagram in Fig. 4-5a). In addition to the shaft and blade passing frequencies, the spectra behind the rotor indicate broad-band strong frequency spikes, just below the blade passing second harmonic; these spikes seem not to be related to the rotor shaft speed.

## 6.2 Asynchronous Velocity Fluctuations

In order to investigate velocity fluctuations, which are not related to the compressor shaft speed, the unsteady velocity signals were treated in a manner similar to analysis used with quasi steady flows, where the overall signal is averaged to recover the mean velocity component, which is subtracted from the overall signal to recover the random velocity fluctuations. This approach was modified for periodic flows, like compressor flow, so that instead of mean velocity an ensemble averaged velocity was used to extract the 'random' velocity fluctuations from the overall velocity signal. Strictly speaking, the 'randomness' in the case of compressor flow should be understood in relation to the rotor shaft and blade passing frequency. In this context, an extracted 'random' signal still may contain a periodic component that, however, is not an integer harmonic of the compressor shaft frequency. Therefore, the extracted signal was labeled as an asynchronous component. This component contains asynchronous periodic velocity fluctuations as well as true velocity random fluctuations (turbulence).

The process depicting extraction of the asynchronous signal component is shown in Fig. 6-7. The top diagram shows the OPR signal for the first *240 ms* of the *5 s* long time interval. The second plot shows recorded axial velocity. The velocity signal was ensemble averaged using the rotor revolution period as a base for averaging. The resulting ensemble averages were already shown in Fig. 5-1a, and is plotted again in the third diagram from the top in Fig. 6-7. Then a new rotor-averaged signal in duration of *5 s* or *80* rotor revolutions was created simply by repeating the rotor ensemble-averaged signal *80* times. The first four cycles, distinguished by color, are shown in the fourth diagram. This new signal was labeled as the periodic signal. Finally an asynchronous velocity signal was created by subtracting the periodic signal from the original overall raw signal, and is shown in the bottom diagram in Fig. 6-7. In this way, all velocity fluctuations associated with the rotor shaft frequency, and for that matter also blade passing frequency, are removed from the velocity signal. The resulting asynchronous signal was then subjected to frequency analysis in an identical manner as already described above.

The overall and asynchronous component spectra for ports *S15A* and *S15B* are presented in Figs. 6-8 through 6-10. Although the spectra were generated for the frequency range up to *10 kHz*, only the portion up to *1.6 kHz* is shown, because there were no detectable frequency spikes above this limit. Note that the frequency axis uses a linear scale. In each figure, the column of plots on the left hand side presents overall spectra, whereas the asynchronous component spectra are shown in the right hand column of plots. As seen here, the blade passing frequency and its harmonics are not present in the asynchronous component spectra, which results in a better visibility of asynchronous fluctuations not associated with rotor shaft frequency.

In general, the data for both ports behind the first rotor, and taken by two different probes, show highly similar variations in the velocity spectra as the probes were traversed along the blade span from the shroud. Starting at the compressor shroud, there is a relatively narrow-band frequency spike at frequencies just above *1100 Hz*, which rapidly disappears as the probe is moved into the blade wake. Once the probe is in the blade wake, a weak broad-band frequency is detectable in the frequency range between *200* and *400 Hz*.

These findings are summarized in Fig. 6-11, where peak frequency, peak amplitude, and local maximum amplitude of velocity random fluctuations are plotted. Once again, it should be remembered that the term random fluctuations is used here in relation to the rotor shaft and blade passing frequencies. As seen in Fig. 6-11, the high frequency spike is restricted to the blade-tip gap region only. The amplitude of velocity fluctuations rapidly drops below a level $0.2\ m.s^{-1}$ once the probe is immersed past the blade tip. The frequency of these velocity fluctuations is remarkably steady in the blade-tip region. Outside of the blade-tip region, however, where the signal amplitude is very low, the accuracy of frequency spike detection is rather poor, which is demonstrated by a large scatter of frequency data. As seen in bottom diagrams in Fig. 6-12, the local maximum amplitude is about *12 dB* above the background in the blade-tip region, and then rapidly drops down which makes detecting local frequency peaks very unreliable.

The low frequency spikes in the spectra of asynchronous velocity fluctuations are much weaker than is the case for high-frequency fluctuations as seen in Fig. 6-11. Asynchronous velocity fluctuations in a frequency range between *300* and *400 Hz* can be detected in a region above *80%* of the blade height. The scatter of the frequency data is relatively large for the same reasons as already discussed above.

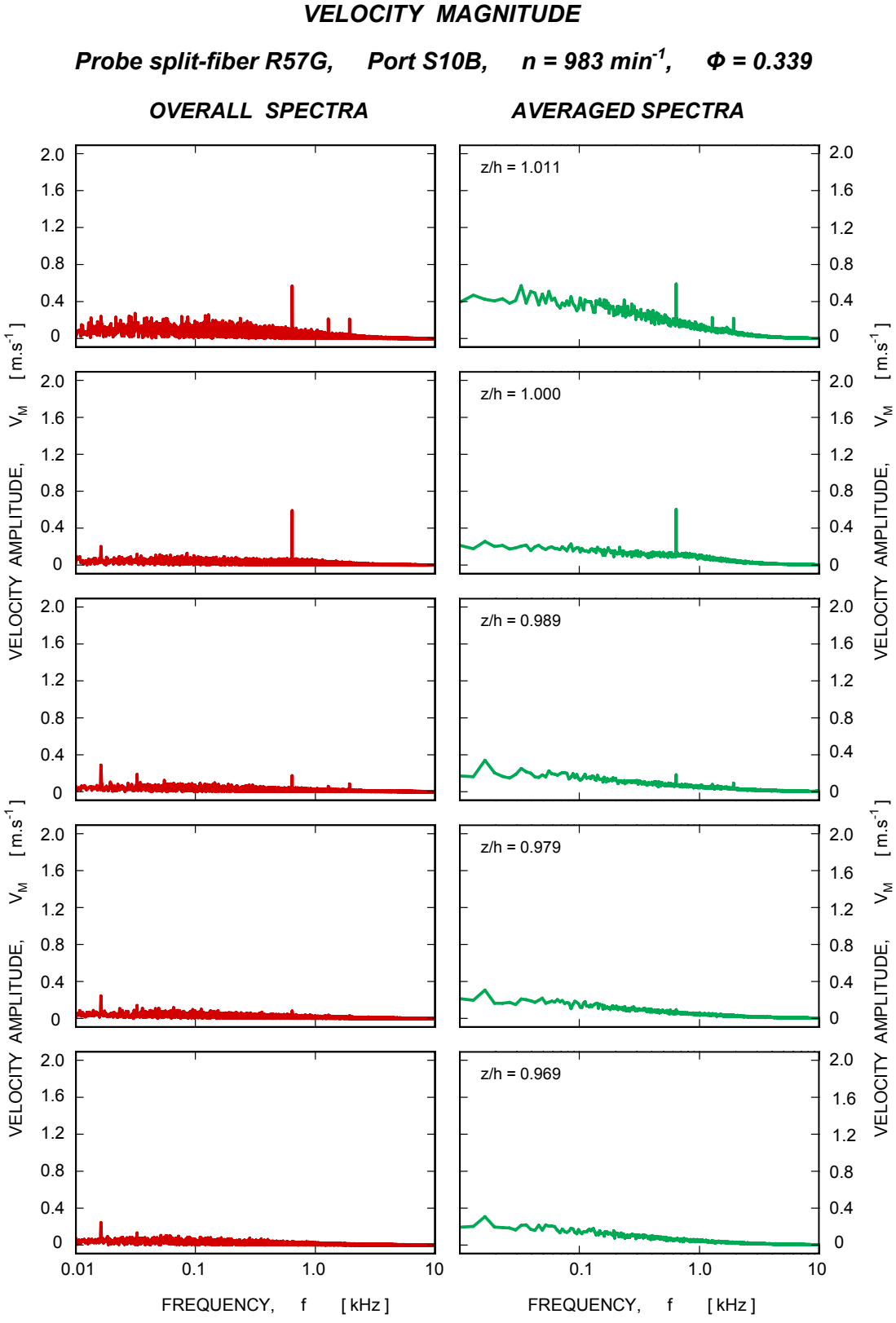


**Fig. 6-1. Overall and averaged spectra of velocity magnitude at station *S10B* for a flow coefficient of *0.339*.**

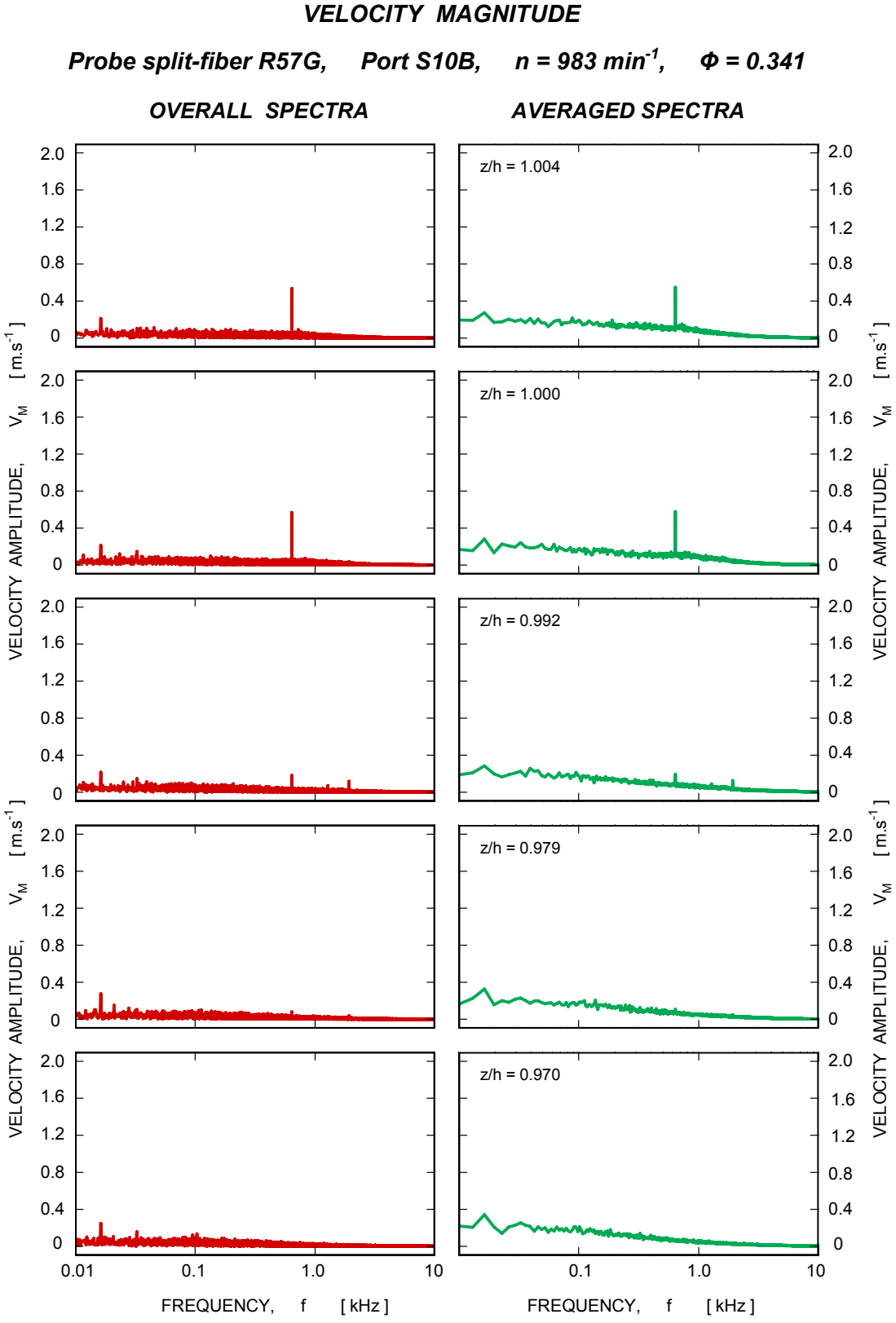


**Fig. 6-2. Overall and averaged spectra of velocity magnitude at station *S10B* for a flow coefficient of *0.341*.**

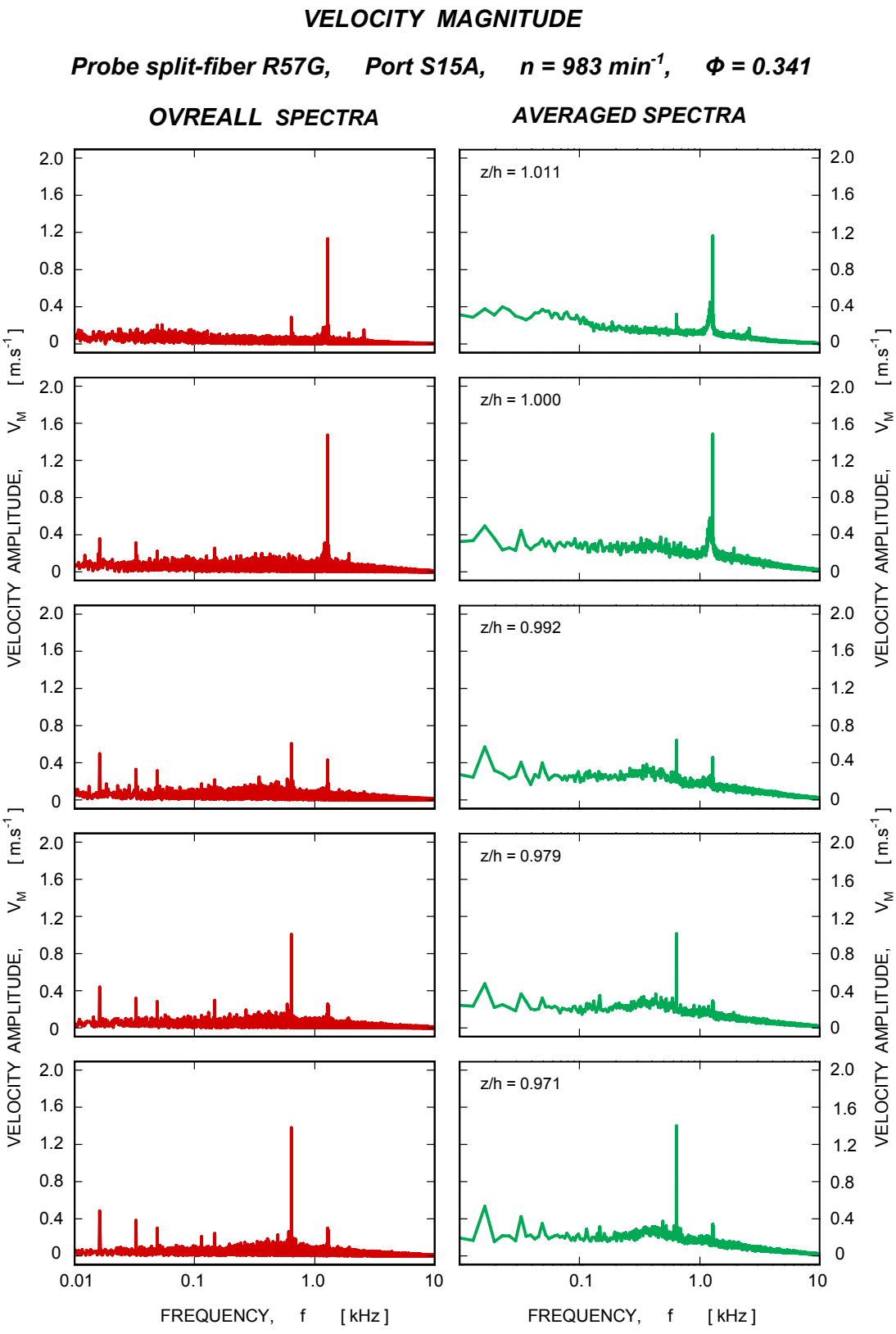


**Fig. 6-3. Overall and averaged spectra of velocity magnitude at station *S15A* for a flow coefficient of *0.341*.**

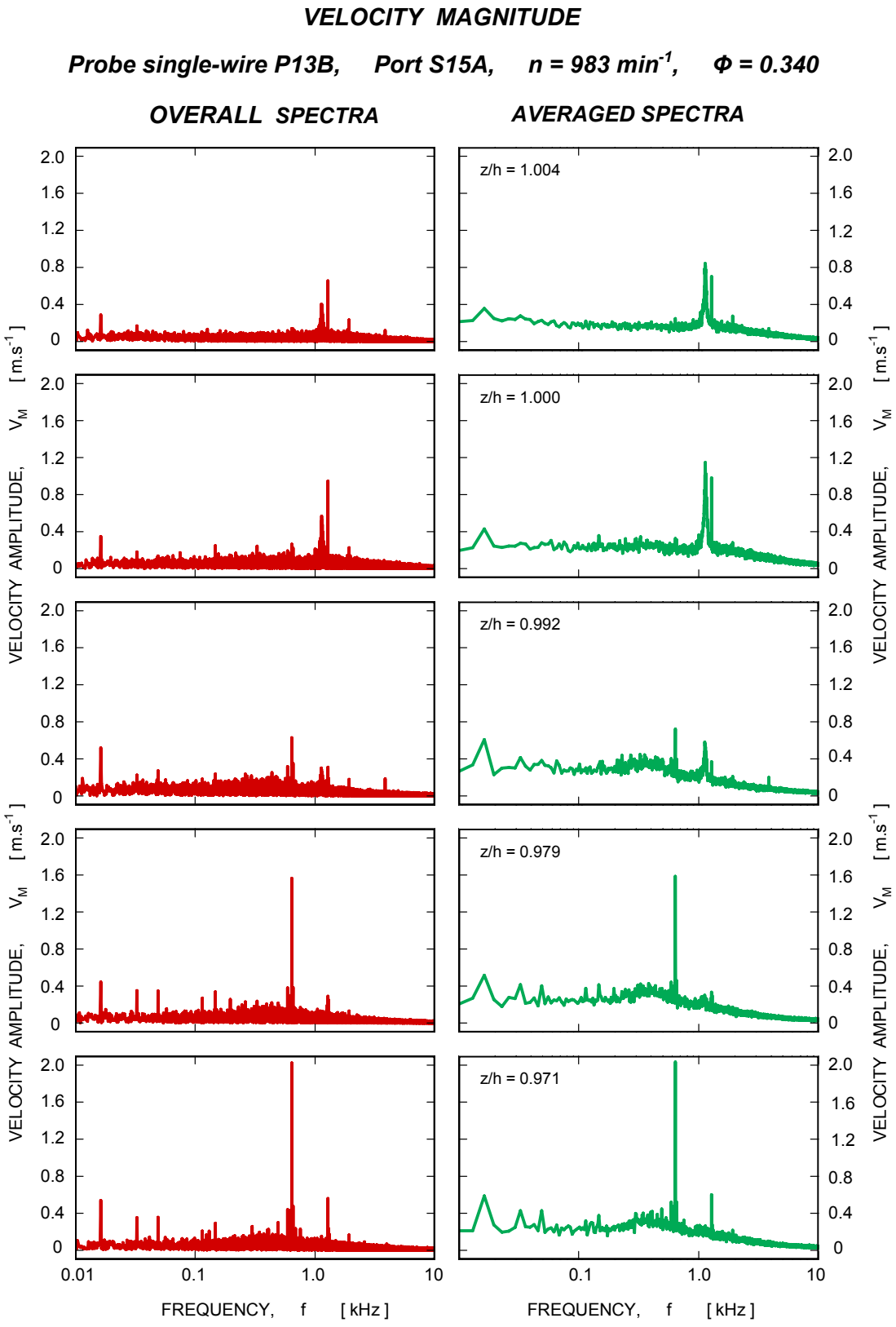


**Fig. 6-4. Overall and averaged spectra of velocity magnitude at station *S15A* for a flow coefficient of *0.340*.**

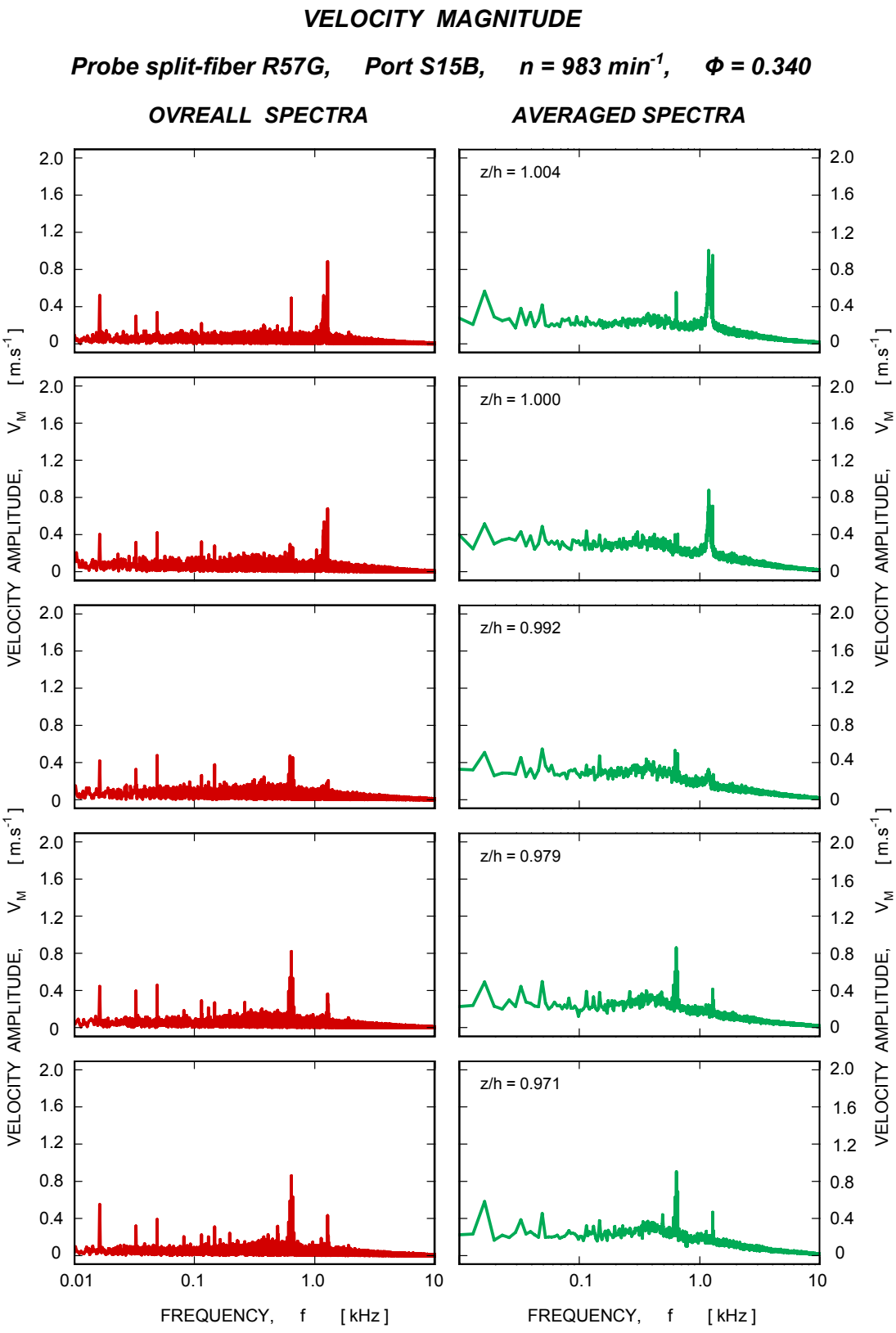


**Fig. 6-5. Overall and averaged spectra of velocity magnitude at station *S15B* for a flow coefficient of *0.340*.**

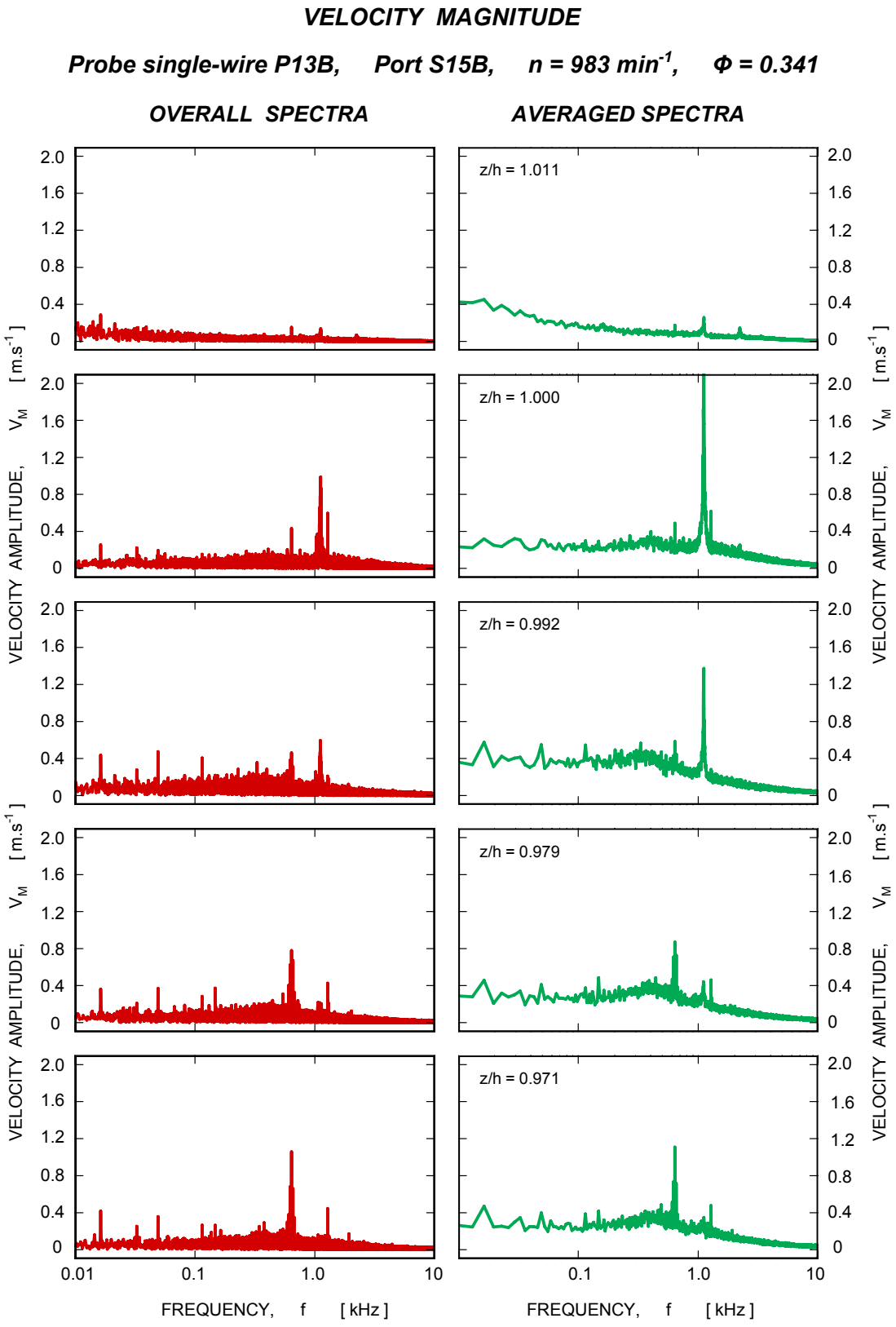


**Fig. 6-6. Overall and averaged spectra of velocity magnitude at station *S15B* for a flow coefficient of *0.341*.**

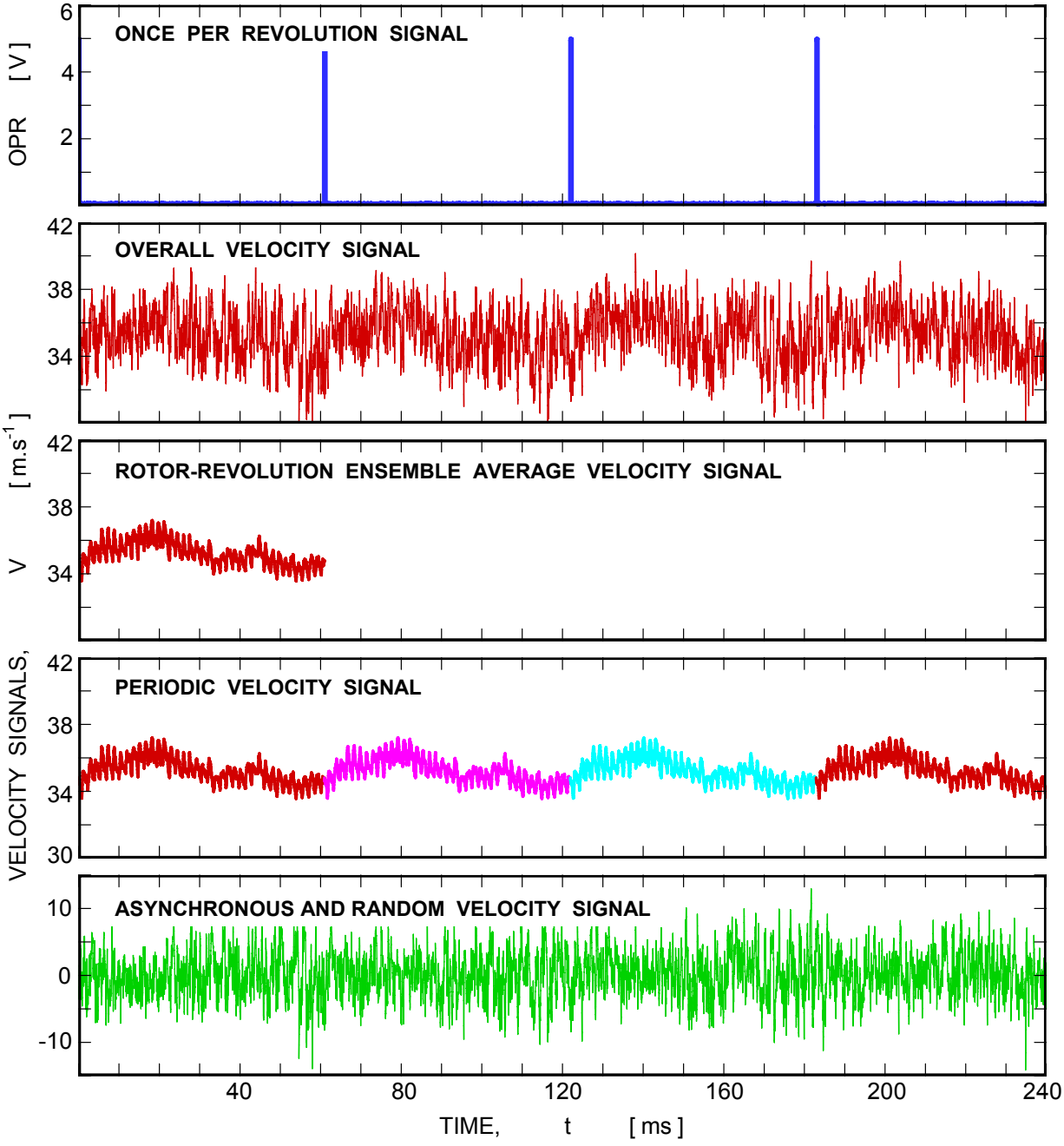


**Fig. 6-7. Procedure to extract ASYNCHRONOUS AND random velocity fluctuations from overall velocity signal.**

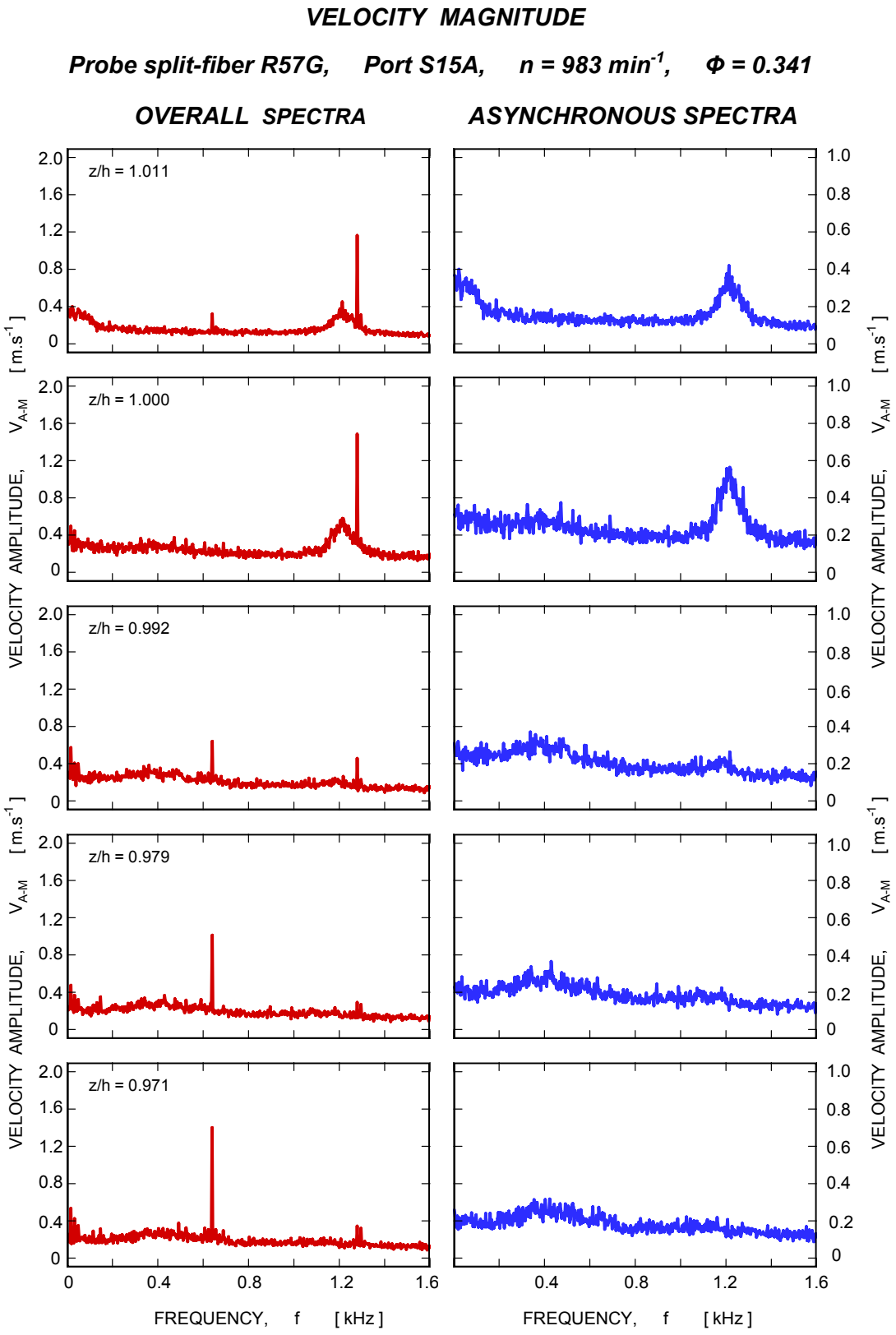


**Fig. 6-8. Spectra of velocity magnitude and asynchronous velocity component at station *S15A* for a flow coefficient of *0.341*.**

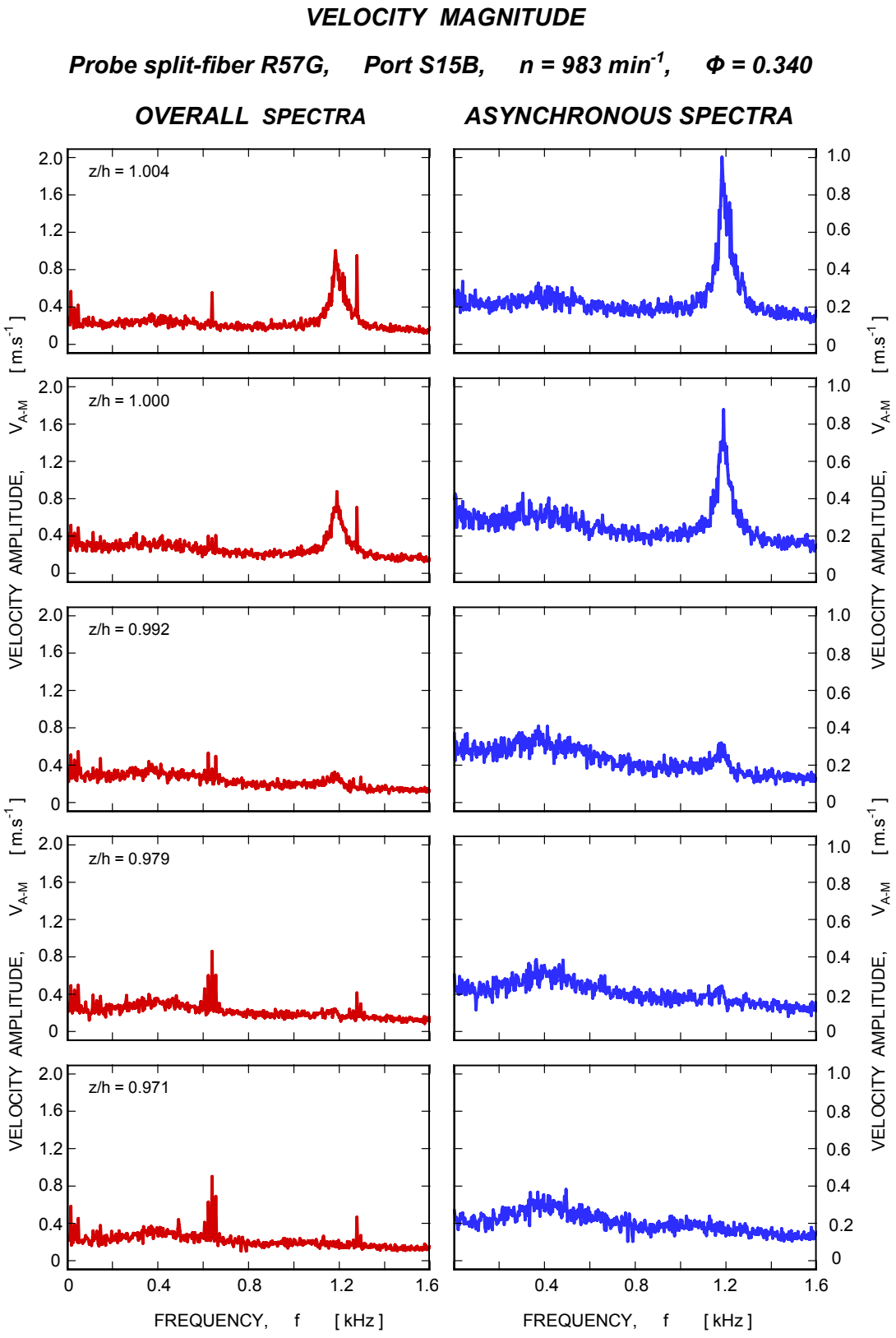


**Fig. 6-9. Spectra of velocity magnitude and asynchronous velocity component at station *S15B* for a flow coefficient of *0.340*.**

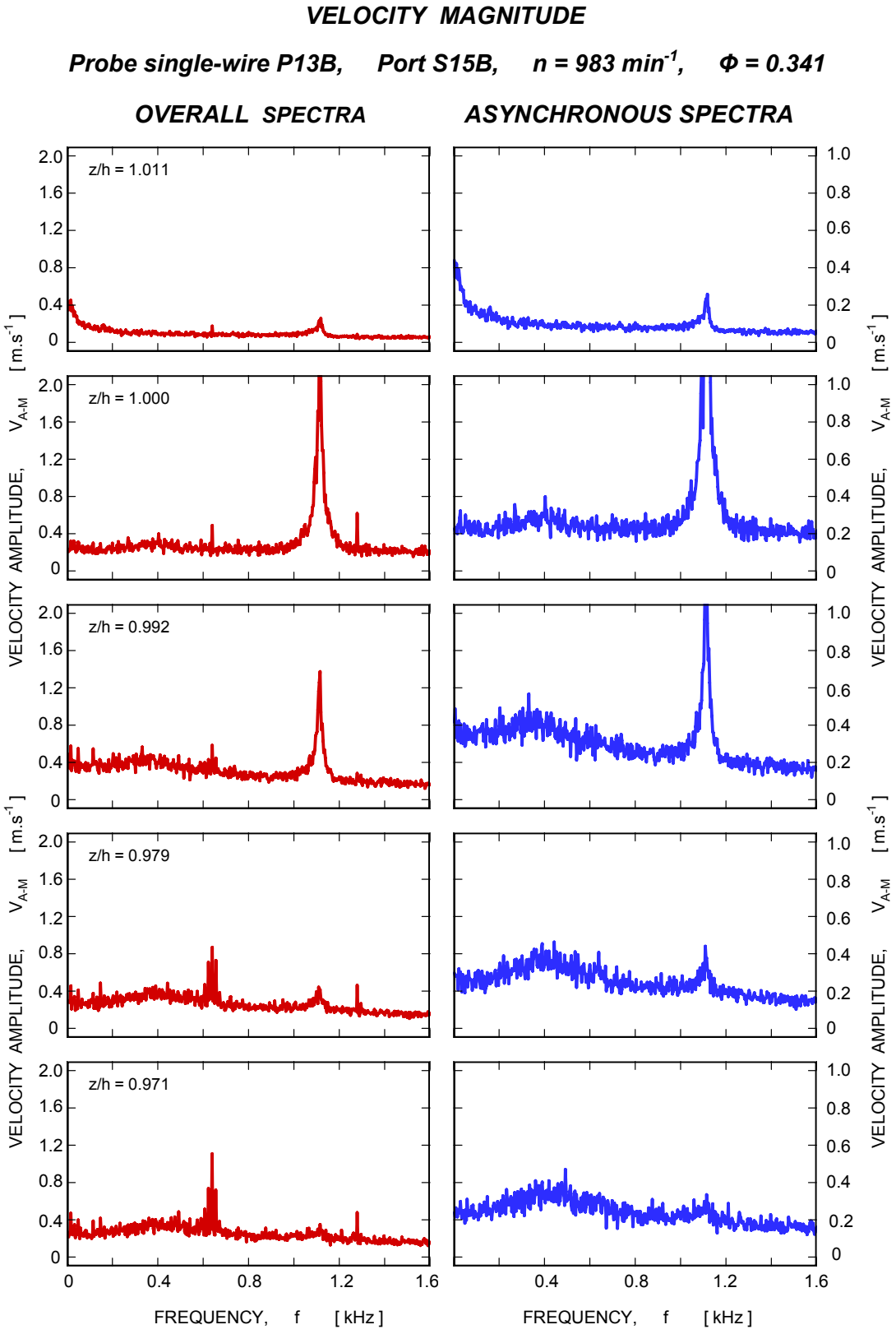


**Fig. 6-10. Spectra of velocity magnitude and asynchronous velocity component at station *S15B* for a flow coefficient of *0.341*.**

***VELOCITY MAGNITUDE***

***Probe single-wire P13B, Port S15B, n = 983 min$^{-1}$, Φ = 0.348***

***HIGH FREQUENCY PEAK***

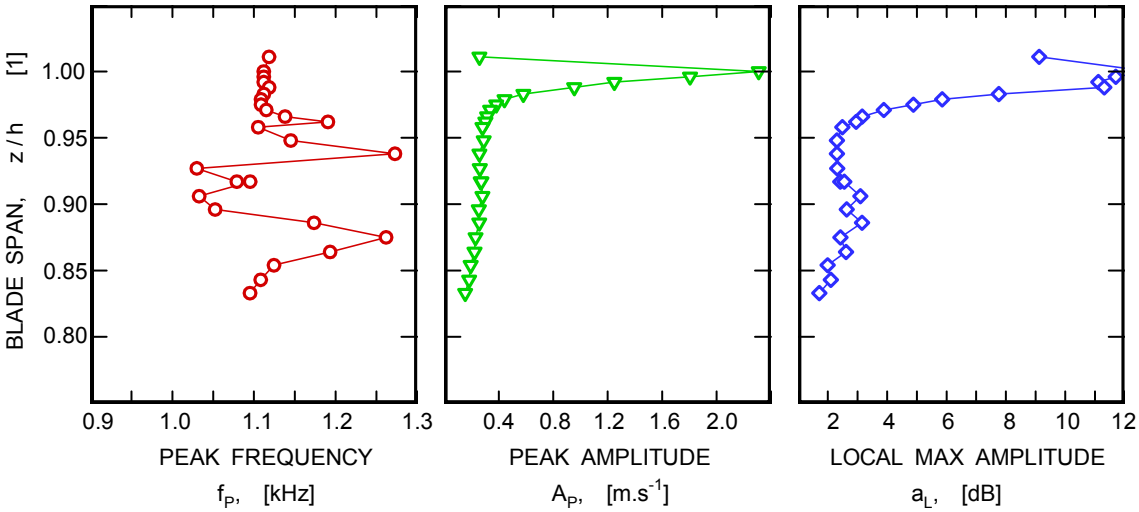


***LOW FREQUENCY PEAK***

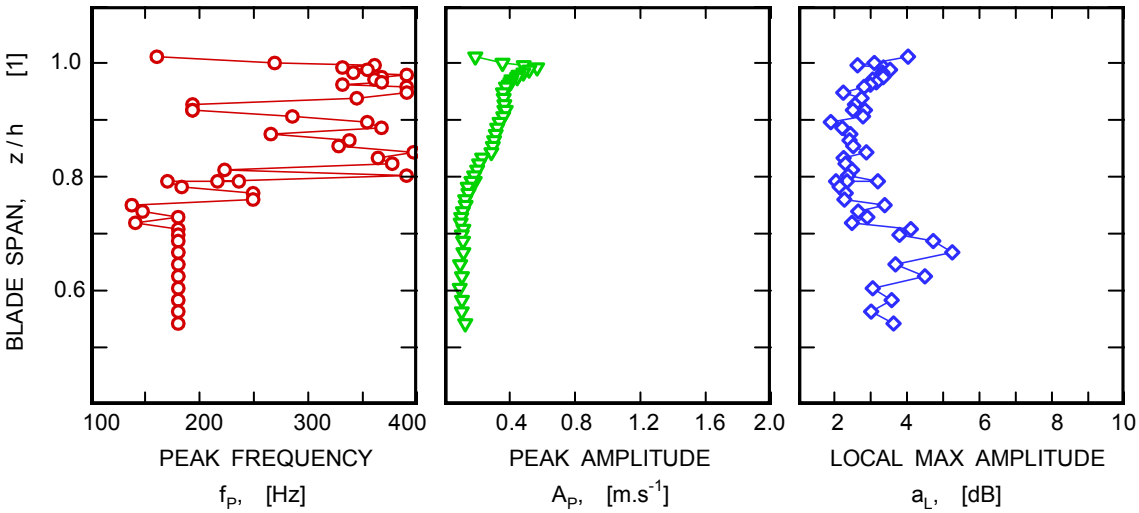


**Fig. 6-11. Distributions of peak frequency and amplitude of velocity fluctuations not associated with rotor shaft frequency at station *S15B* for a flow coefficient of *0.348*.**

## Summary of Results

The results of unsteady velocity and flow direction measurements carried out in the first stage of the NASA Low Speed Axial Compressor were presented in this report. The compressor was in its basic configuration with a smooth (solid) shroud inner wall over the first rotor without any special treatment to modify compressor performance. Specifics of the compressor geometry and probe ports, needed to analyze acquired data, were presented in Section 1. Three different thermo-anemometric probes were used during the course of this investigation. The probes were: a split-fiber probe (Dantec 55R57), a single-fiber probe (Dantec 55R03), and a single-wire probe (Dantec 55P13). The split-fiber probe was used to measure simultaneously two velocity components (velocity magnitude and velocity angle) in a plane perpendicular to the probe cylinder, whereas the other two probes were used to measure the velocity magnitude only. The probes as well as the in-house developed signal decomposition procedure for the split fiber probe were described in Section 2.

Data analysis started with inspection of velocity and flow angle radial profiles, presented in Section 3. These profiles were acquired at two probe ports upstream of the first rotor, and at two probe ports downstream of the first rotor. An unusual radial distribution of flow velocity with two distinct velocity depressions for one probe port upstream of the first rotor was caused by double crossing of the IGV wake as explained in this chapter. Radial profiles showed good agreement; observed small differences reflect probe position (mid pitch, wake, or stagnation region). Because axial and tangential velocity components were measured simultaneously, the Reynolds shear stress component in unsteady flow could be determined. Tangential velocity components acquired for probe positions downstream and upstream of the rotor were used to calculate rise of flow total temperature across the rotor. In this particular case of a low speed axial compressor, the total temperature rise was very small, and of the order of the error band for the existing experimental techniques for flow temperature measurements. Also, flow coefficient and stage loading factor distributions along the rotor blade span based on unsteady velocity measurements were presented in this chapter.

Blade passage ensemble averages of unsteady flow data were presented in Section 4. Data for axial and tangential velocity components were shown first in a form of line plots for selected blade span positions. This was followed by similar distributions for flow angle and velocity magnitude. The reason for velocity magnitude plots was to enable direct comparison of split-fiber probe data with results obtained by single-fiber and wire probes. Blade passage ensemble averages were also used to generate contour maps for velocity components and flow direction over the entire area of the rotor blade channel. Blade ensemble averaging yields parameter distributions that represent flow in an idealized single blade channel. All variations in the flow due to differences in geometry of individual blade channels or of the entire rotor are suppressed by a blade ensemble averaging process for the averaged signals. To trace differences among individual blade channels, the ensemble averaging must be based on a time period that is equal to one rotor revolution.

Ensemble averages, based rotor revolution, are presented in Section 5. The line plots of axial and tangential velocity components and flow angle are arranged similarly as in the previous chapter. Attention was paid to an anomaly seen in the lower part of one of the rotor blade channels. This anomaly was traced to a total pressure probe mounted between two rotor blades, which was left in the compressor rotor since the previous test program. This omission was in fact very helpful in verifying the data reduction methodology and reliability of the entire unsteady data measurement system. Contour maps based on rotor-revolution ensemble averaging are also presented in this chapter, albeit only for the axial velocity component. The maps depict three adjacent rotor blade passages; the middle passage is the one with built-in total pressure probe. The large wake of the rotor probe in the middle channel clearly illustrates the extent of unavoidable flowfield distortion due to presence of aerodynamic probes in the flow.

Finally, the last section (Section 6) presents results of spectral analysis. All data presented were computed as amplitude spectra. First, the spectra were generated raw and averaged overall spectra. The reason for spectral averaging is to increase confidence in the amplitude levels. However, an unwanted

consequence of spectral averaging for limited segments of velocity signals is coarser frequency resolution of the averaged spectra.

In order to investigate velocity fluctuations that are not related to the compressor shaft speed, the unsteady velocity signals were decomposed into mean periodic velocity signals and signals of velocity random fluctuations; however, this approach was modified for periodic flows, like compressor flows. Using this approach, asynchronous velocity fluctuations were recovered. These fluctuations are periodic in the time domain but their frequency is not a multiple of the compressor shaft frequency. Overall and asynchronous velocity component spectra are presented for frequency range up to *1.6 kHz* only, because there were no detectable frequency spikes above this limit. The spectra of the random velocity component exhibit high and low frequency peaks. The high frequency peak (about *1100 Hz*) is detectable only in the blade tip gap, whereas the low frequency peak (about *350 Hz*) extends from the blade tip down to *80%* of the blade height. The low frequency peak is noticeably weaker than the high frequency one.

Cross-examination of all the data acquired confirms that the data set described in this report represents consistent and accurate velocity and flow direction data that can serve as a reliable benchmark data set for analysis of the compressor characteristics and performance, and help with further improvements of CFD design codes.

# Appendix A—Performance of Thermo-Anemometric Probes

As mentioned in previous chapters, it was expected that the dynamic response of a split fiber probe was restricted to lower frequencies than that of a single wire probe. Therefore, single-fiber and single-wire probes were also used at measurement stations *S15A* and *S15B* past the first rotor to verify that no important unsteady phenomena in the flow are missed due to a lower dynamic range of split-fiber probes. The results are summarized in Figs. A-1 and A-2. Only the velocity magnitude and magnitude unsteadiness are presented here because single-element probes are insensitive to velocity direction in the plane perpendicular to the sensing element.

The left hand side diagrams in Figs. A-1 and A-2 are for velocity magnitude. The results for three different probes, measured during three different test runs, agree remarkably well with each other. It confirms three things: first, there was an excellent repeatability in setting the operation conditions of the NASA research compressor; second, the measured velocity distributions were reliable, which was the result of careful calibration of all three probes; and third, the complex data reduction procedure for the split-fiber probe, developed in house, worked correctly. The verification of the data reduction method for the split-fiber probe guaranties that the axial and tangential velocity components (and for that matter also the flow angle) were determined correctly. Recall that velocity data for the split-fiber probe were generated by combining two nonlinear independent signals, while for a single-element thermo-anemometric probe, the velocity data were obtained by a relatively simple nonlinear conversion of a single signal.

The right hand side diagrams in Figs. A-1 and A-2 contain unsteadiness distributions of velocity magnitude. As seen in these plots, the single-wire probe (green line) records the highest unsteadiness level; this probe was expected to have very high dynamic response and therefore recorded contributions of high frequency oscillations. The split-fiber probe recorded unsteadiness levels lower than the single-wire probe but noticeably higher than the levels recorded by the single-fiber probe. It agrees with findings in Ref. 2-4 that the split-fiber probe, despite its larger diameter, has a frequency response that extends to higher frequencies than the one for the single-fiber probe. As already stated in the previous chapter, it is believed that the frequency response of a split-fiber probe was flat to at least *10 kHz*, which is sufficient for unsteady velocity acquisition in the NASA Low Speed Axial Compressor.

The differences in velocity unsteadiness levels, as seen in the previous two figures, cannot, however, be explained solely on the account of limited frequency responses of these three probes in a sense of filtering out the energy contributions contained in higher frequency oscillations. Assuming for a moment that the single-wire probe data represent *100%* of energy associated with velocity fluctuations, and then the split-fiber probe data contain only *70%* of this energy, and the single-fiber probe data only *56%* of the energy associated with velocity fluctuations. These findings seem to indicate that all three probes differ not only as far as the cut-off frequency is concerned, but mainly that their dynamic performance is governed by noticeably different transfer functions.

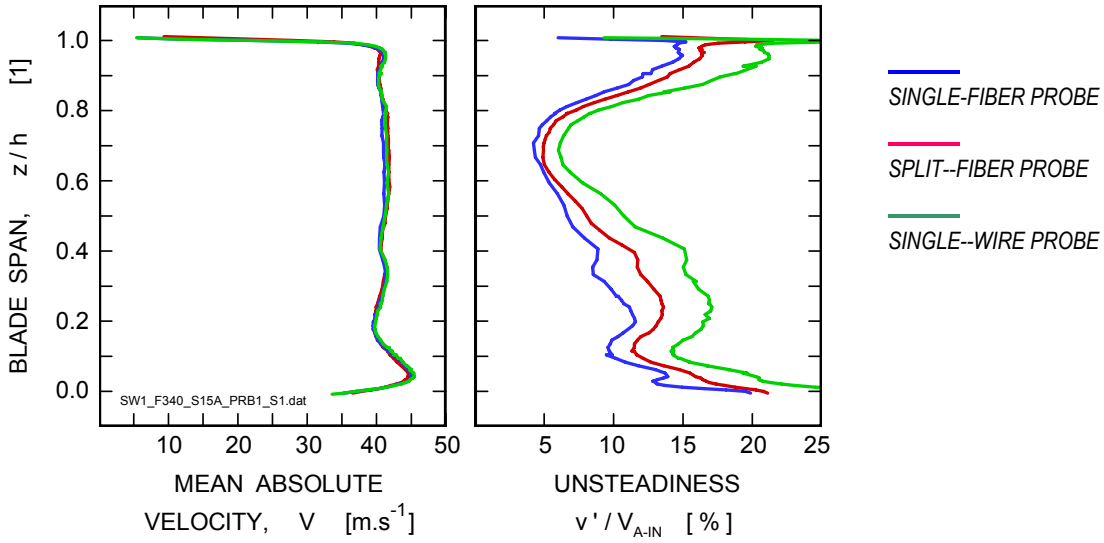


**Fig. A-1.** **Comparison of experimental data acquired by three types of thermo-anemometric probes for flow coefficient of *0.340* at measurement station *S15A*.**

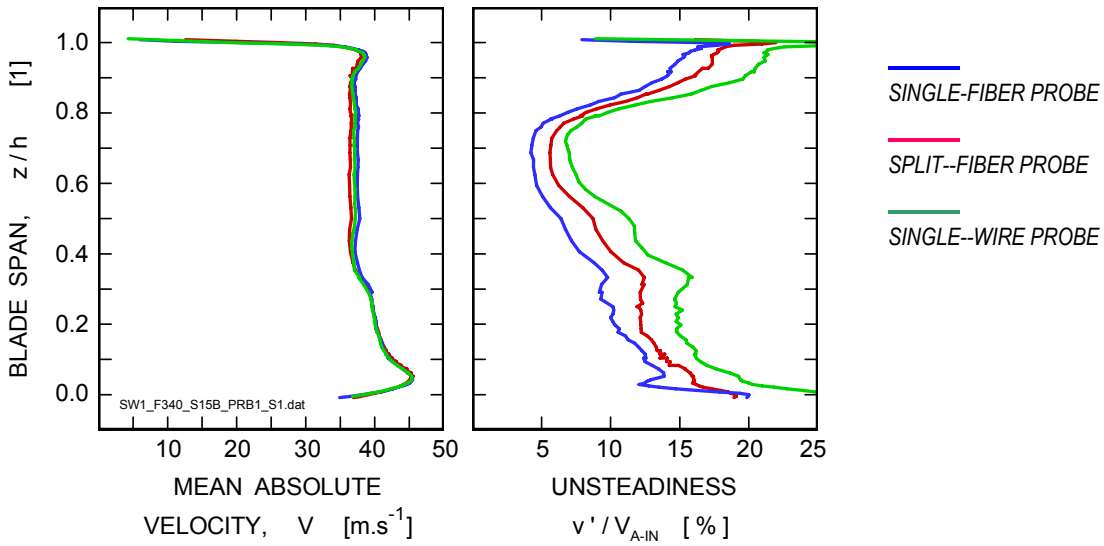


**Fig. A-2.** **Comparison of experimental data acquired by three types of thermo-anemometric probes for flow coefficient of *0.340* at measurement station *S15B*.**

# Appendix B—Dynamic Response of Thermo-Anemometric Probes

A probe transfer function dictates dynamic response of the probe to velocity fluctuations. In order to compare probe dynamic performance, data acquired by single-wire and single-fiber probes are presented in Figs. B-1 and B-2. Both data sets are blade ensemble averages that were acquired at probe port *S15A* for a flow coefficient of *0.340*. Data acquired by the split-fiber probe for the same compressor operation point were already presented in Fig. 4-7. As mentioned above, the single element probes can respond only to changes in velocity magnitude in the plane perpendicular to the probe sensing element. Therefore, the data acquired by the split-fiber probe were reduced in a manner yielding also the velocity magnitude. Ensemble averages of velocity magnitude and magnitude unsteadiness are plotted for several positions along the blade height in the same way for all three probes.

Inspection of Figs. 4-7, B-1, and B-2 indicates that the single-fiber probe performance visibly lags behind the other two probes. A one-to-one comparison of probe performances is in Fig. B-3 for three blade height stations of *z/h = 0.9*, *0.5*, and *0.1*. Data for individual probes are distinguished by color: single-wire probe is shown in green, split-fiber in red, and single-fiber in blue color. Both blade-to-blade magnitude distributions as well as unsteadiness distributions show the same trends. The response of fiber probes is lagging behind the single-wire probe, which is demonstrated by lower amplitude of unsteady signals as well as by increase in the time delay of recorded signals (phase delay). This is a typical response of probes with restricted frequency characteristic (longer time constant). This outcome was expected. What is surprising is that whereas the split-fiber probe signal is not found to be lagging behind the single-wire probe signal significantly, the performance of the single-fiber probe is unacceptably poor. It should be stressed here again that the split-fiber probe has a diameter of *200 μm*, which is nearly three times larger than the one of the single-fiber probe (*70 μm*). This reversed trend in the frequency response with an increasing fiber diameter was first time indicated in Ref. 4-3, and recently confirmed by measurement in a free jet (Ref. 2-4). In any case, the cut-off frequency of the single-wire probe was determined to be *75 kHz* based on the square wave test (Ref. 4-4). The cut-off frequency of the split-fiber probe is obviously lower than that, but we believe it is above a *10 kHz* level which is fully sufficient for this investigation. The estimate for the split-fiber probe cut-off frequency is based on results of signal frequency analysis that will be discussed later. The cut-off frequency of the single-fiber probe is below *10 kHz* and therefore data acquired by the single-fiber probe were not used to analyze unsteady flow behavior in the NASA Low Speed Axial Compressor.

Contour maps of velocity magnitude as measured by a split-fiber probe and a single-wire probe are presented in Figs. B-4 and B-5. As discussed before a single-wire probe can measure velocity magnitude only, but it possesses superior dynamic characteristics. To facilitate comparative plots the split-fiber probe signals were reduced in a manner that yielded velocity magnitude and velocity unsteadiness similar to those produced by a single element thermo-anemometric probe. The contour maps are shown only for the operation condition with the highest level of velocity unsteadiness; it is for a flow coefficient of *0.341* and the stator vane stagnation region (measurement station *S15B*). As seen here, both probes detect nearly identical contour maps for both velocity magnitude and velocity unsteadiness. The only detectable difference is that the single-wire probe records slightly larger areas of intense velocity unsteadiness, due to its significantly faster dynamic response than the split fiber probe has.

A poor response of the single-fiber probe is also reflected in the velocity spectra generated from signal recorded by this probe. The velocity spectra are shown in Fig. B-6; data were taken at probe port *S15A* for a flow coefficient of *0.341*. The results should be compared with data for the same operation conditions, however, taken by a split-fiber and single-wire probes as shown in Fig. 6-3 and 6-4, respectively. As seen in figure B-6 for the single-fiber probe, the amplitudes are flat for frequencies above *3 kHz*. This is a consequence of limited dynamic response of the single-fiber probe (Ref. 6-2).

The comparison of spectral data between the split-fiber and single-wire probes confirms that the split-fiber probe is fully capable to detect reliably unsteady velocity field in a frequency range that is fully sufficient for the unsteady flow phenomena encountered in the NASA Low Speed Research Compressor.

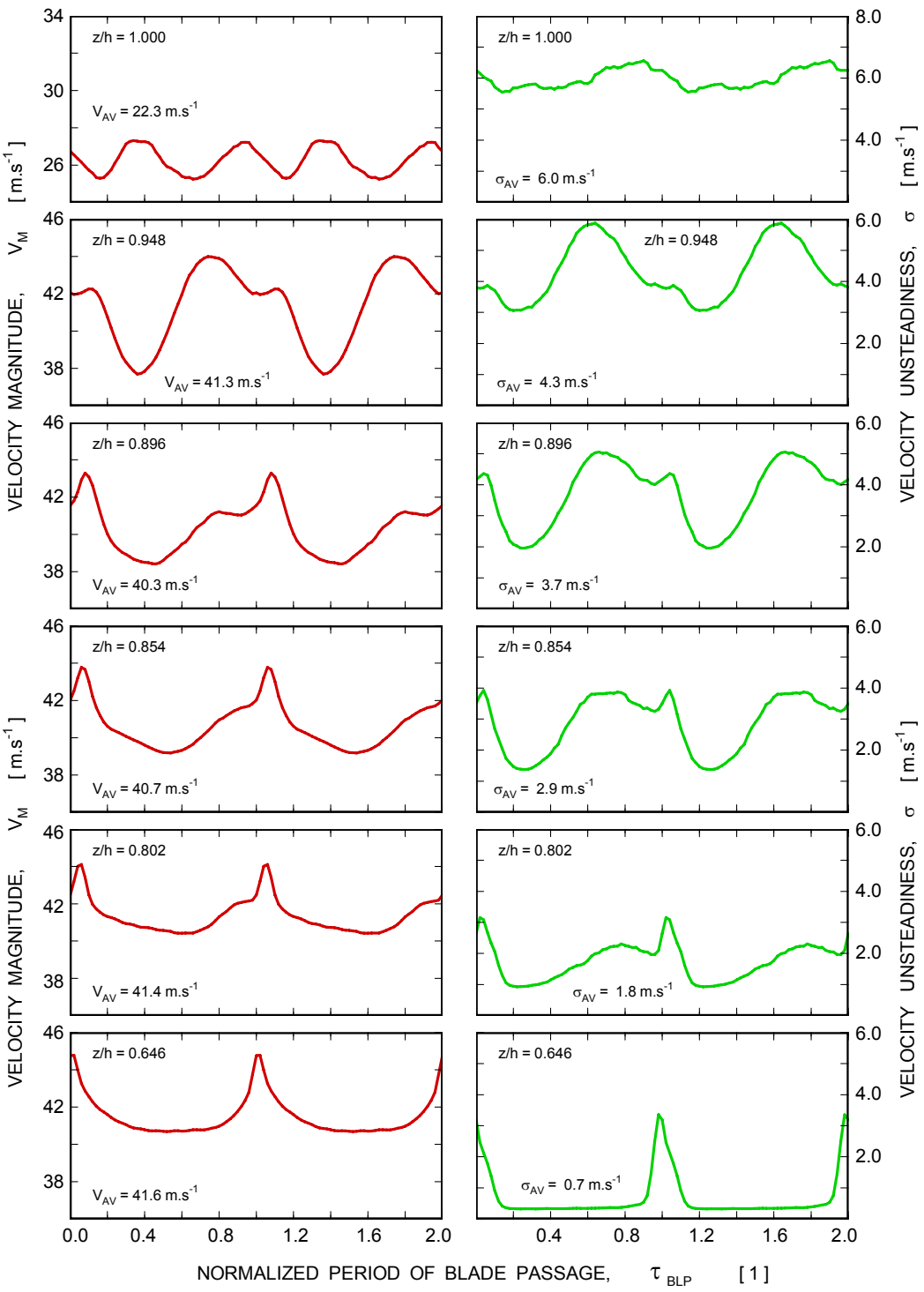


**Fig. B-1a. Blade passage ensemble averages of velocity magnitude at station *S15A* for flow coefficient of *0.340* recorded by a single-wire probe.**

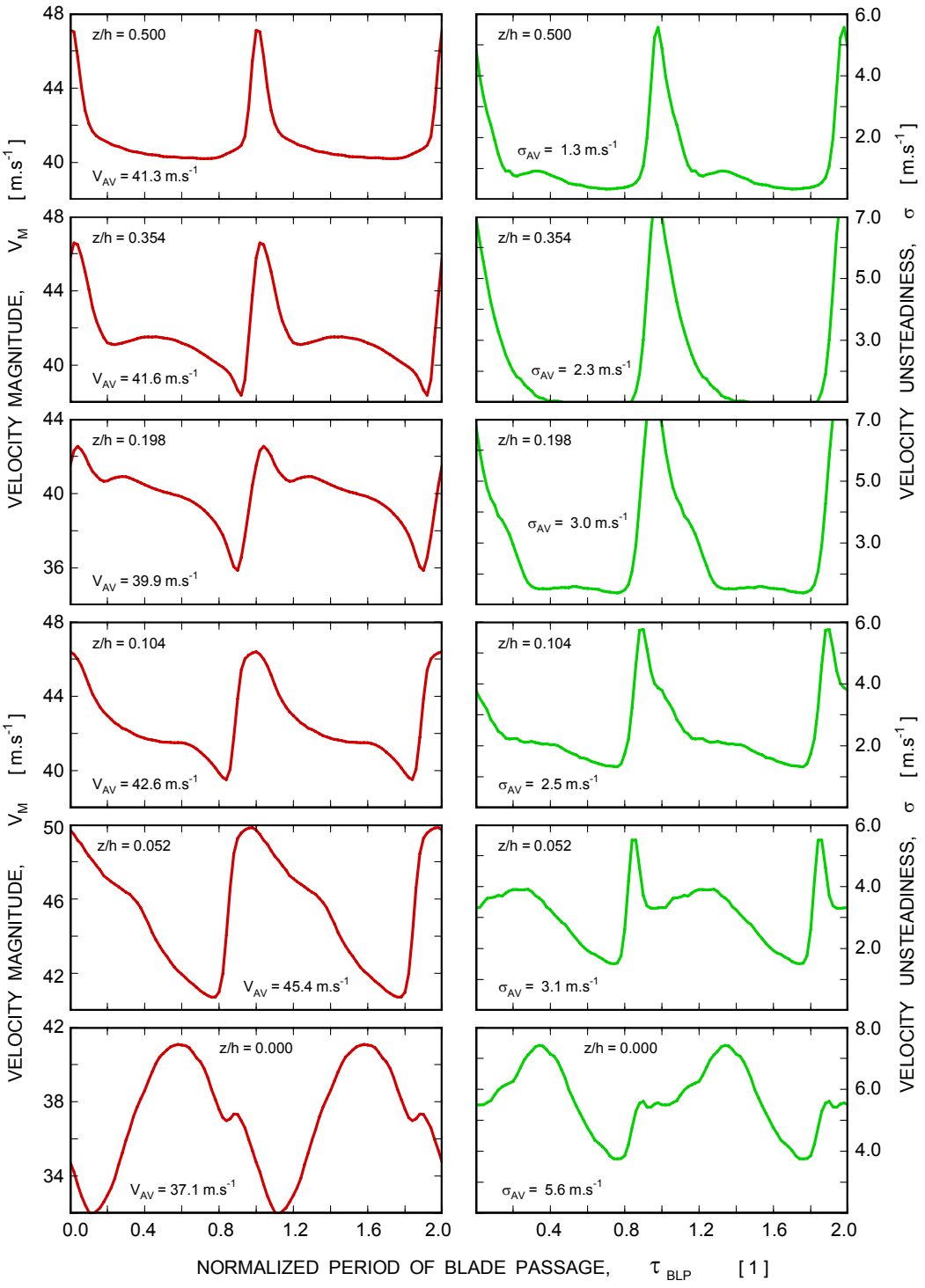


**Fig. B-1b. Blade passage ensemble averages of velocity magnitude at station *S15A* for flow coefficient of *0.340* recorded by a single-wire probe.**

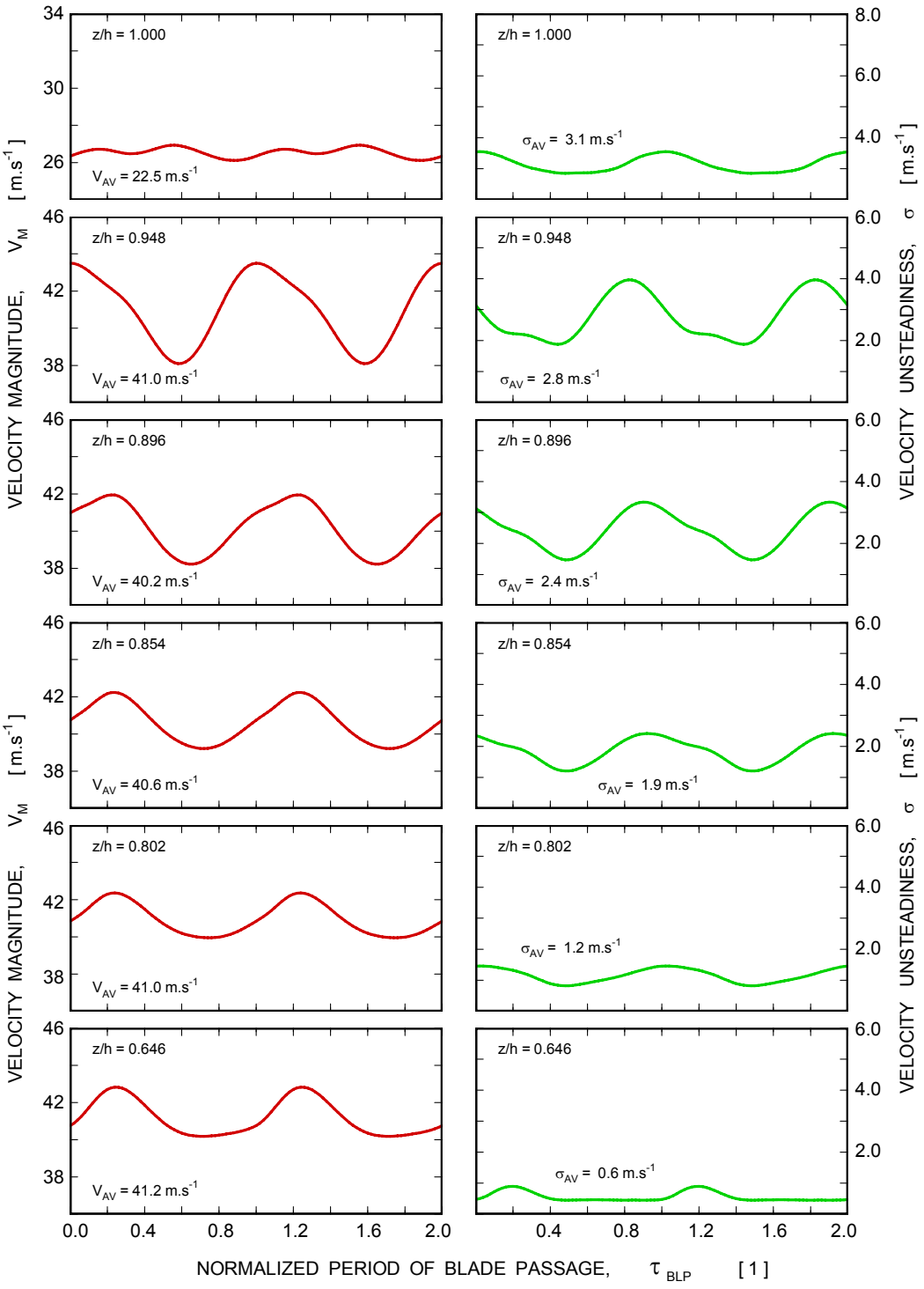


**Fig. B-2a. Blade passage ensemble averages of velocity magnitude at station *S15A* for flow coefficient of *0.340* recorded by a single-fiber probe.**

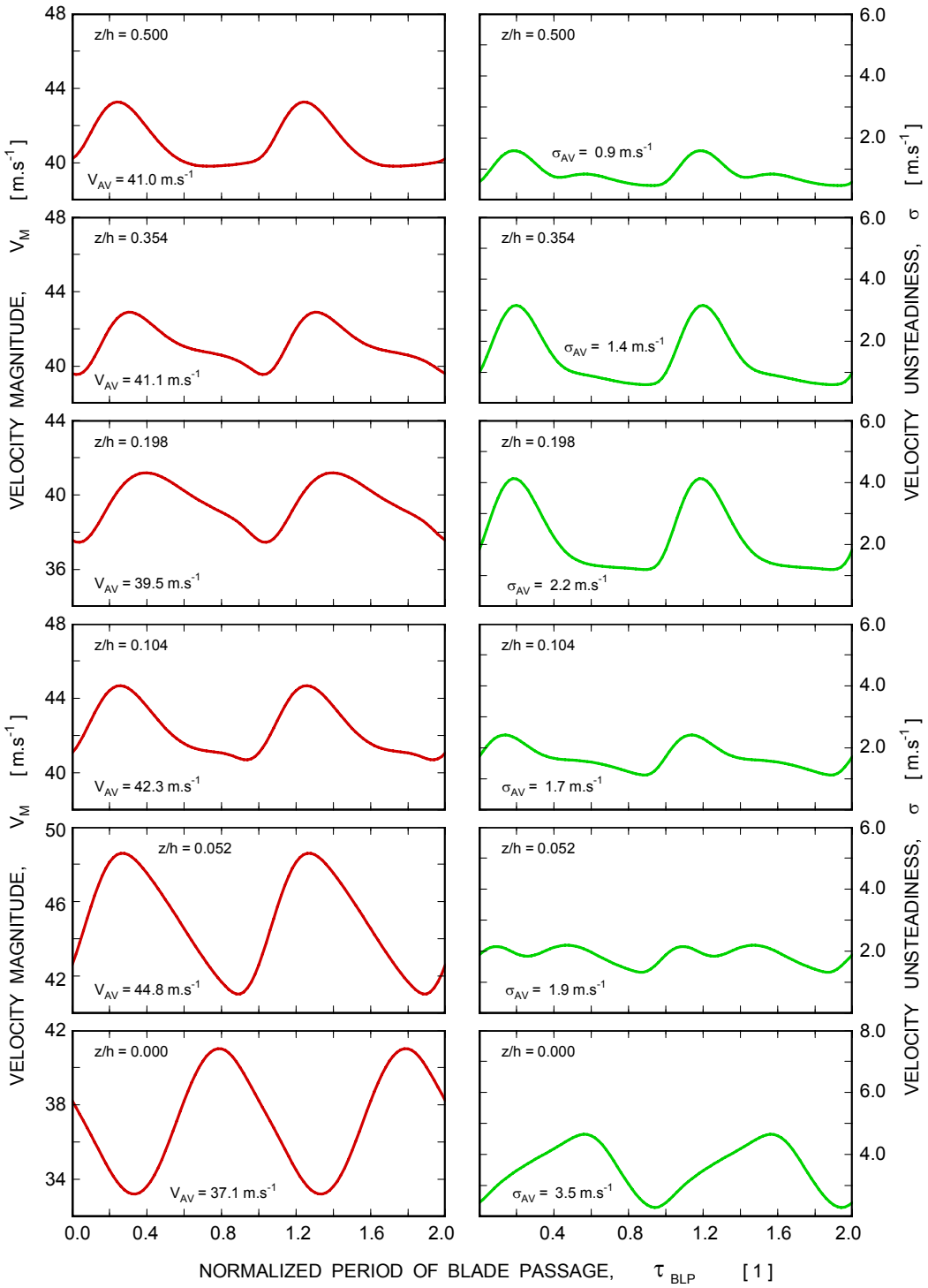


**Fig. B-2b. Blade passage ensemble averages of velocity magnitude at station *S15A* for flow coefficient of *0.340* recorded by a single-fiber probe.**

***Port S15A,  n = 984 min$^{-1}$,  Φ = 0.340***

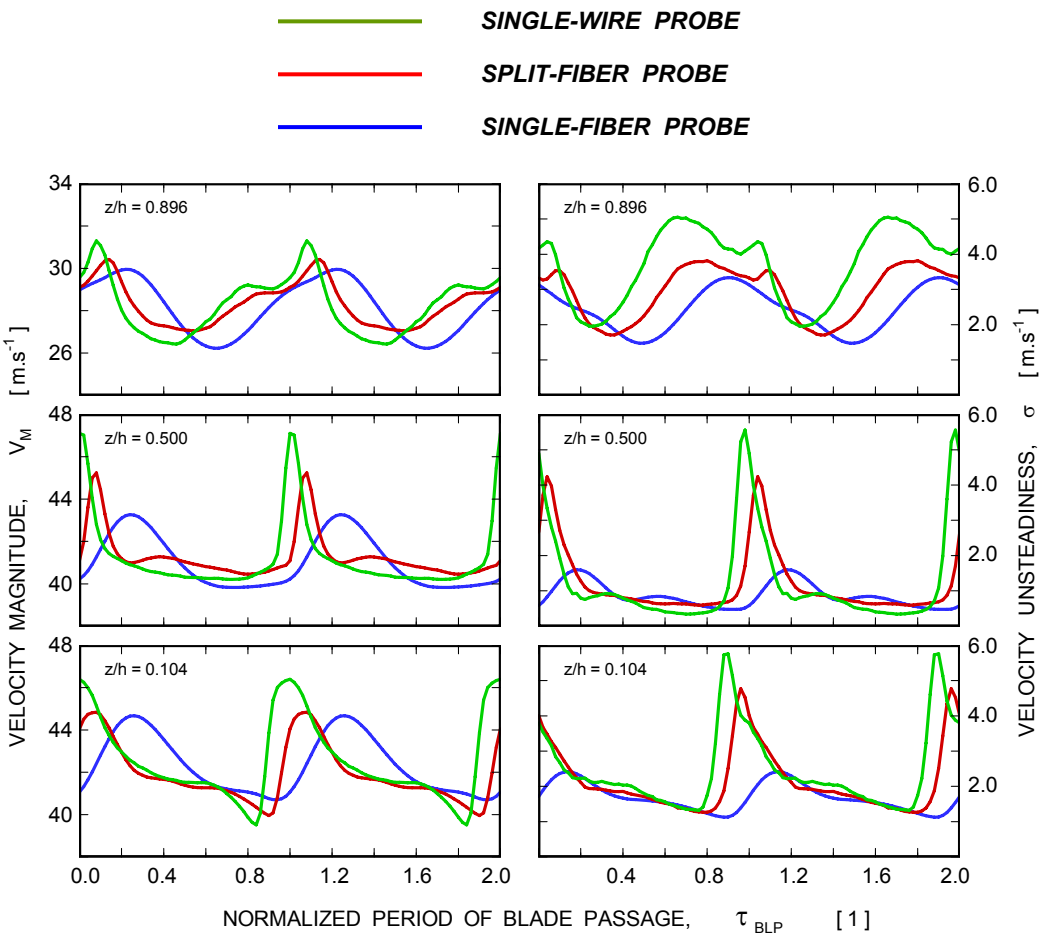


**Fig. B-3.  Comparison of dynamic behavior of single-wire, split-fiber, and single-fiber thermoanemometric probes.**

***VELOCITY MAGNITUDE***

***Port S15B, n = 983 min$^{-1}$, Φ = 0.341***

***SPLIT FIBER PROBE R57G***

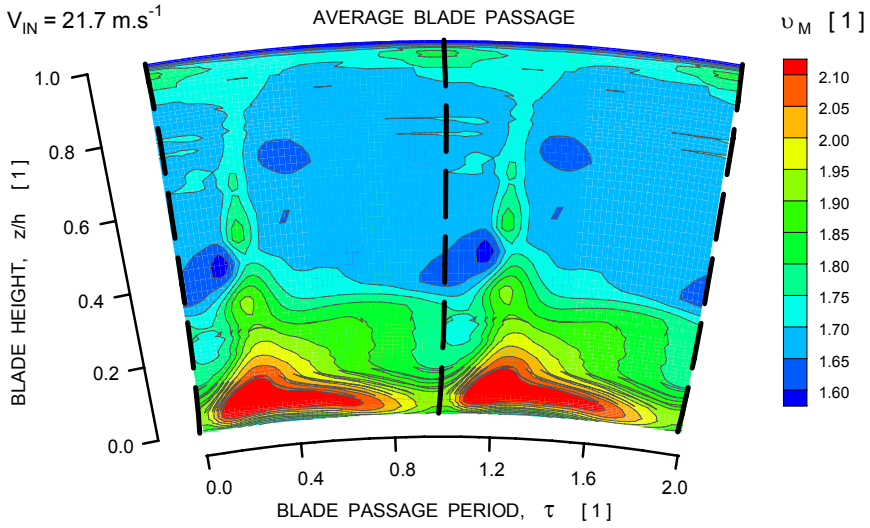


***SINGLE WIRE PROBE P13B***

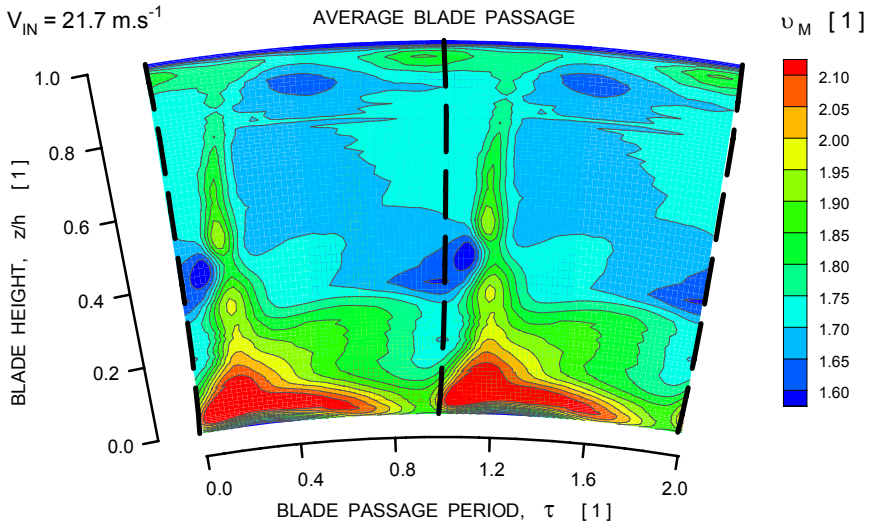


**Fig. B-4. Contour maps of velocity magnitude for a rotor blade passage as measured by split-fiber and single-wire probes at station *S15B* for flow coefficient of *0.341*.**

## *VELOCITY UNSTEADINESS*

### *Port S15B, n = 983 min$^{-1}$, Φ = 0.341*

***SPLIT FIBER PROBE R57G***

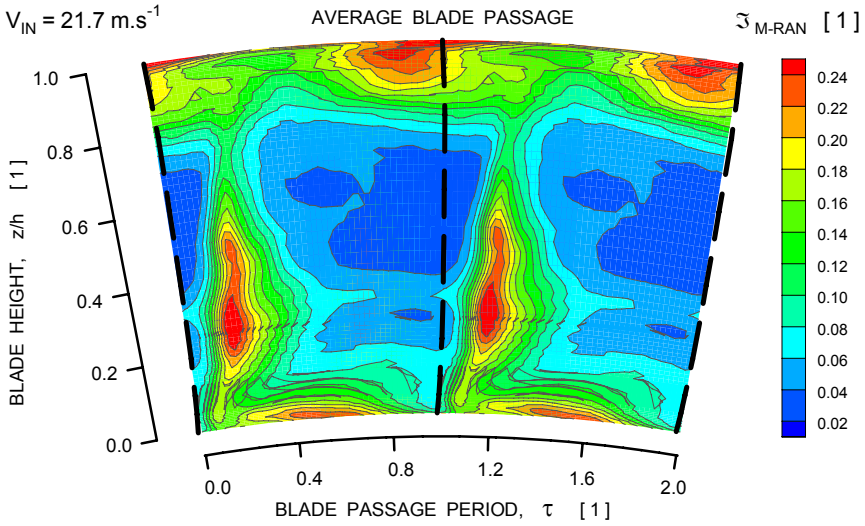


***SINGLE WIRE PROBE P13B***

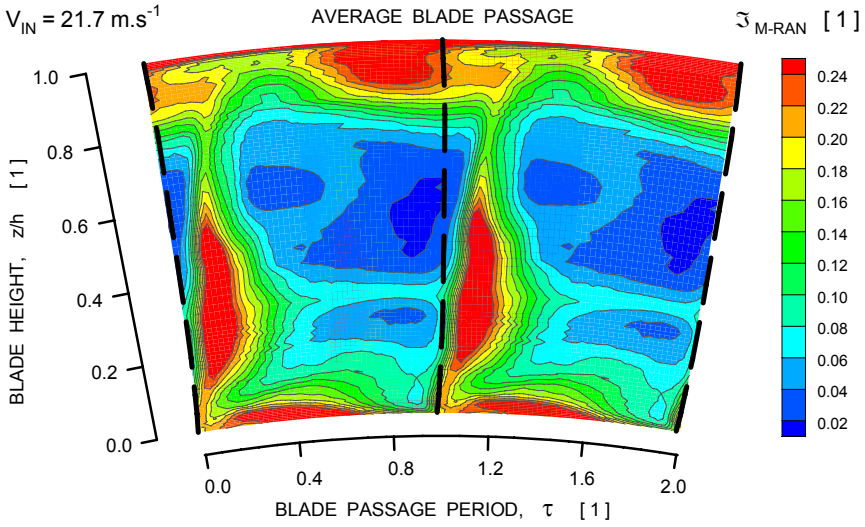


**Fig. B-5. Contour maps of velocity unsteadiness for a rotor blade passage as measured by split-fiber and single-wire probes at station *S15B* for flow coefficient of *0.341*.**

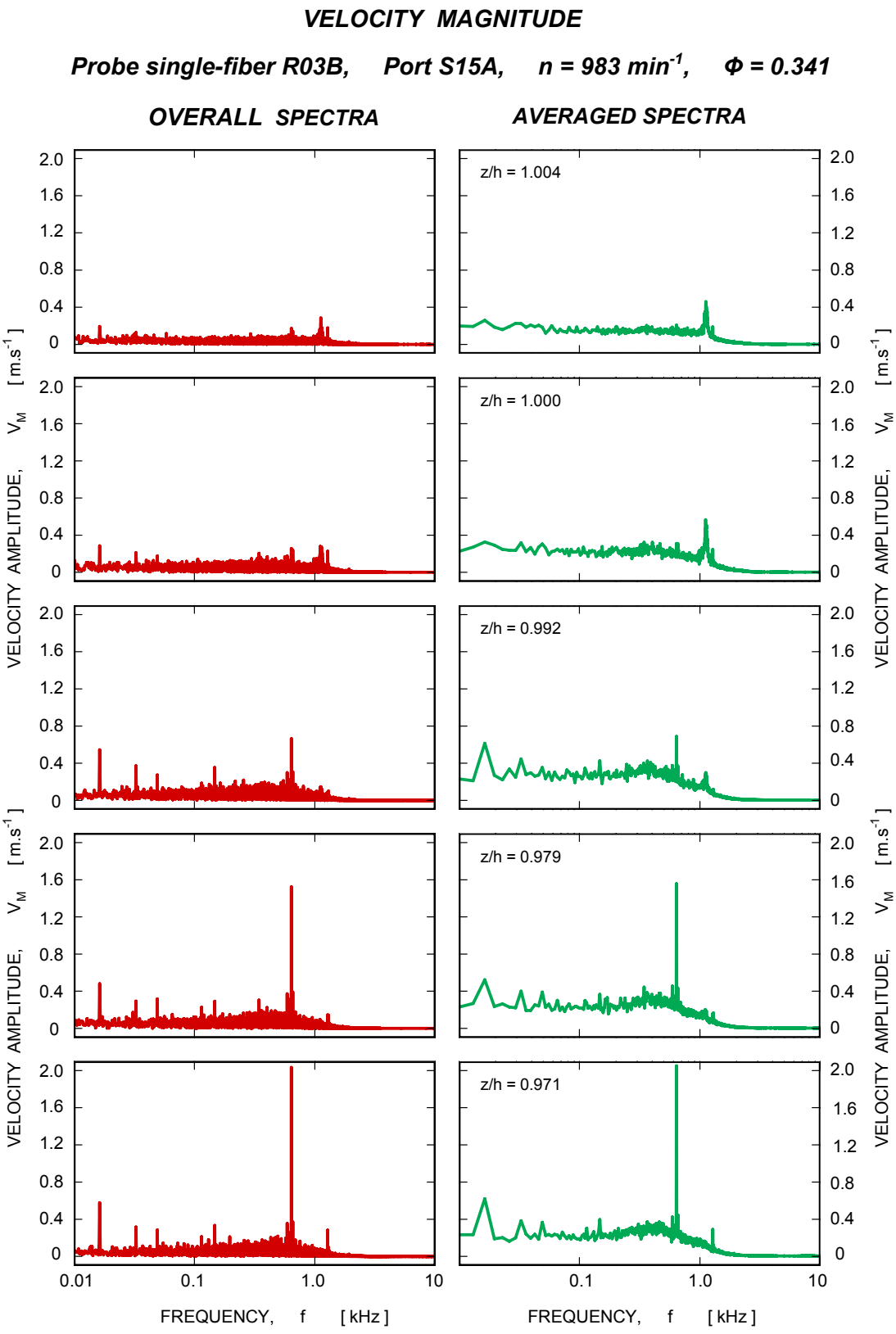


**Fig. B-6. Overall and averaged spectra of velocity magnitude at station *S15A* for a flow coefficient of *0.341* recorded by a single-fiber probe.**

# References


1-1 Wasserbauer C.A., Weaver, H.F., and Senyitko, R.G.: "NASA Low-Speed Axial Compressor for Fundamental Research," NASA TM–4635, 1995.

1-2 Wellborne S.R. and Okiishi, T.H.: "Effects of Shrouded Stator Cavity Flows on Multistage Axial Compressor Aerodynamic Performance," NASA CR–198536, 1996.

2-1 Lepicovsky, J.: "Application of a Split-Fiber Probe to Velocity Measurement in the NASA Research Compressor," NASA/CR—2003-212489, June 2003.

2-2 Bruun, H.H.: "Hot-Wire Anemometry, Principles and Signal Analysis," Oxford University Press Inc., New York, 1995.

2-3 Freymuth, P. and Fingerson, L.M.: "Electronic testing of frequency response for thermal anemometers," TSI Quarterly, November 1977.

2-4 Lepicovsky, J.: "Measurements with Split-Fiber Probe in Complex Unsteady Flows," NASA/CR–2004-213065, April 2004.

2-5 Probe Catalog, Dantec Measurement Technology A/S, Denmark, 1992.

2-6 Lepicovsky, J. and Braunscheidel, E.P.: "Measurement of Flow Pattern within a Rotating Stall Cell in an Axial Compressor," ASME paper GT-2006-91209, May 2006.

3-1 Hill, P. and Paterson, C.: "Mechanics and Thermodynamics of Propulsion," Addison-Wesley Publishing Company, 1992.

3-2 Dixon, S.L.: "Mechanics, Thermodynamics of Turbomachinery," Pergamon International Library, Oxford.

4-1 Lepicovsky, J.: "Methodology of Blade Unsteady Pressure Measurement in the NASA Transonic Flutter cascade," NASA/TM—2002-211894, October 2002.

4-2 Lepicovsky, J. and Bell, W.A.: "Aerodynamic Measurements about a Rotating Propeller with a Laser Velocimeter," Journal of Aircraft, Vol. 21, pp. 264-271, 1984.

4-3 Freymuth, P. and Fingerson, L.M.: "Electronic testing of frequency response for thermal anemometers," TSI Quarterly, November 1977.

4-4 Bruun, H.H.: "Hot-Wire Anemometry, Principles and Signal Analysis," Oxford University Press Inc., New York, 1995.

6-1 LabVIEW Function and VI Reference Manual, National Instruments, January 1998.

6-2 Lepicovsky, J.: "Measurements with Split-Fiber Probe in Complex Unsteady Flows," NASA/CR—2004-213065, April 2004.

| REPORT DOCUMENTATION PAGE | Form Approved OMB No. 0704-0188 |
|---|---|



| 1. REPORT DATE (DD-MM-YYYY) | 2. REPORT TYPE | 3. DATES COVERED (From - To) |
|---|---|---|
| 31-05-2007 | Final Contractor Report | |

**4. TITLE AND SUBTITLE**
Unsteady Velocity Measurements in the NASA Research Low Speed Axial Compressor
Smooth Wall Configuration

**5a. CONTRACT NUMBER**
NNC06BA07B

**5b. GRANT NUMBER**

**5c. PROGRAM ELEMENT NUMBER**

**6. AUTHOR(S)**
Lepicovsky, Jan

**5d. PROJECT NUMBER**

**5e. TASK NUMBER**

**5f. WORK UNIT NUMBER**
WBS 561581.02.08.03.21.02

**7. PERFORMING ORGANIZATION NAME(S) AND ADDRESS(ES)**
ASRC Aerospace Corporation
Cleveland, Ohio 44135

**8. PERFORMING ORGANIZATION REPORT NUMBER**
E-15971

**9. SPONSORING/MONITORING AGENCY NAME(S) AND ADDRESS(ES)**
National Aeronautics and Space Administration
Washington, DC 20546-0001

**10. SPONSORING/MONITORS ACRONYM(S)**
NASA

**11. SPONSORING/MONITORING REPORT NUMBER**
NASA/CR-2007-214815

**12. DISTRIBUTION/AVAILABILITY STATEMENT**
Unclassified-Unlimited
Subject Categories: 07 and 09
Available electronically at http://gltrs.grc.nasa.gov
This publication is available from the NASA Center for AeroSpace Information, 301-621-0390

**13. SUPPLEMENTARY NOTES**

**14. ABSTRACT**
The report is a collection of experimental unsteady data acquired in the first stage of the NASA Low Speed Axial Compressor in configuration with smooth (solid) wall treatment over the first rotor. The aim of the report is to present a reliable experimental data base that can be used for analysis of the compressor flow behavior, and hopefully help with further improvements of compressor CFD codes. All data analysis is strictly restricted to verification of reliability of the experimental data reported. The report is divided into six main sections. First two sections cover the low speed axial compressor, the basic instrumentation, and the in-house developed methodology of unsteady velocity measurements using a thermo-anemometric split-fiber probe. The next two sections contain experimental data presented as averaged radial distributions for three compressor operation conditions, including the distribution of the total temperature rise over the first rotor, and ensemble averages of unsteady flow data based on a rotor blade passage period. Ensemble averages based on the rotor revolution period, and spectral analysis of unsteady flow parameters are presented in the last two sections. The report is completed with two appendices where performance and dynamic response of thermo-anemometric probes is discussed.

**15. SUBJECT TERMS**
Unsteady flow; Compressors; Velocity measurements

| 16. SECURITY CLASSIFICATION OF: | | | 17. LIMITATION OF ABSTRACT | 18. NUMBER OF PAGES | 19a. NAME OF RESPONSIBLE PERSON |
|---|---|---|---|---|---|
| a. REPORT | b. ABSTRACT | c. THIS PAGE | | | Jan Lepicovsky |
| U | U | U | | 106 | 19b. TELEPHONE NUMBER (include area code) 216-433-1402 |